POLITECNICO DI TORINO

Doctorate Course in Electronic Devices

XXVIII cycle

MICROCANTILEVER-BASED SENSING ARRAYS FOR EVALUATION OF BIOMOLECULAR INTERACTIONS

Candidate: Gianluca Palmara

Supervisors: Prof. Carlo Ricciardi

Prof. Fabrizio C. Pirri

ABSTRACT

The controlled immobilization on a surface of biomolecules used as recognition elements is of fundamental importance in order to realize highly specific and sensible biosensors. Microcantilevers (MC) are nanomechanical sensors, which can be used as label free micro-sized mechanical transducers. MC resonant frequency is sensitively modified upon molecules adsorption, demonstrating an impressive mass resolution. A widely used approach for the immobilization of biorecognition elements on silicon substrates consists in the deposition of 3-aminopropyl-triethoxysilane (APTES) followed by the incubation with glutaraldehyde (GA) as a crosslinking agent. However, these derivatization processes produce a variable chemical functionalization because of the spontaneous polymerization of GA in aqueous solutions. With the aim of producing a more reliable chemical functionalization for protein immobilization, the deposition of a thin film of APTES by self-assembly followed by the modification of its amino groups into carboxyl groups by incubating in succinic anhydride (SA) is proposed. Moreover, the activation of these terminal carboxyl groups were performed by using the EDC/s-NHS protocol in order to enhance their reactivity toward primary amine groups present on biomolecules surface. This method was characterized from a physico-chemical point of view by means of compositional and morphological surface analysis. Moreover, data acquired after the application of this functionalization to a MC-based system showed a highly reproducible deposition of APTES/SA when compared to APTES/GA deposition process. APTES/SA derivatized MC arrays were then incubated with biomolecules for the study of its protein binding capability: the quantification of the grafted biomolecules was performed from the gravimetric data and compared with a theoretical surface density calculated through a molecular modeling tool, providing information about the orientation of the proteins tethered to the surface. In order to avoid or reduce non-specific protein interactions, Bovine Serum Albumin and ethanolamine were considered for their blocking capability. Finally, the detection of the envelope glycoprotein domain III of the Dengue virus type 1 based on immune-specific recognition through the DV32.6 antibody was performed, providing a stoichiometry ratio for the DIII-DV1/DV32.6 interaction. Currently, no cure or vaccine are available; thus, a better

understanding of the interactions between the viruses and specific antibodies is expected to provide fundamental information for the development of a vaccine.

Contents

Chapter 1: Introduction

The main subject of this thesis is the application of microcantilever-based techniques in the field of biosensing. After the strong impact AFM microscope had in the scientific world, microcantilevers has shown their great capability in transducing the weak surface-tip interaction in a measurable signal [1]. The increasing interest of the scientific community on cantilevers, one of the simpler MEMS structure, provided the stimulus to develop innovative ways of sensing for a wide range of physical phenomena. During the last years, cantilevers have been investigated for a wide range of applications because of their amazing capability of sensing environmental characteristics and for their sensitivity regarding surface interactions, transducing in this way physical, chemical and biological phenomena [2-4].

In this work, resonant frequency variation of microcantilevers has been employed as a platform for the detection of biomolecules interactions. The microcantilever capability of detecting in a sensitive manner the adsorbed mass on its surface makes it a promising platform for the study of the weak forces established in biological interactions and paves the way for the realization of more specific and stable biosensors, thanks to a deeper control and understanding of protein-surface interactions.

In the first paragraph, a general overview of the biosensing field will be given, illustrating different approaches for the detection of biological molecules. In the following paragraph, microcantilever-based sensing is described, focusing on the operating principles of single-clamped beams. A brief description of the main achievement in microcantilever-based biosensing will be presented.

In the third paragraph, the surface chemical modification of silicon-based biosensors is provided, focusing on the most widely used chemical strategies for immobilization of biomolecules. Finally, background information about the biological aspects of dengue virus related disease are described. Moreover, the currently available methods and techniques used for diagnostic purposes will be illustrated.

1.1. Biosensor overview

The IUPAC definition of a biosensor affirms that a biosensor is an integrated device that is able to provide specific quantitative or semi-quantitative analytical information using a biological recognition element that is put in direct spatial contact with a transducer element [5]. A plain schematic representation of the working principle of a biosensor is reported in Fig. 1.1.

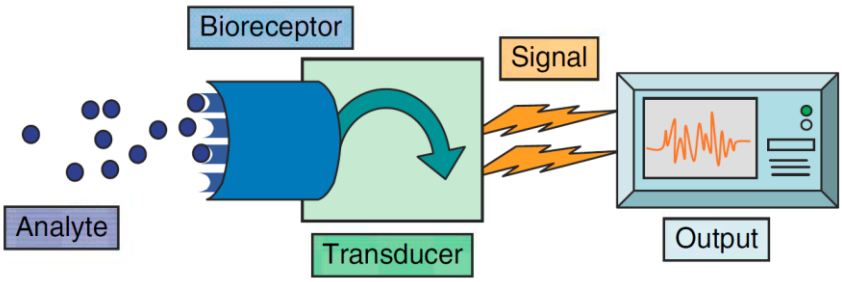

Fig. 1.1. Schematic representation of a biosensor (Adapted from Griffin and Stratis-Cullum, 2014).

A common definition is that biosensors are analytical devices that use biological macromolecules to establish specific interactions with an analyte and, subsequently, these interactions are detected with a transducer. Usually, biosensors are subdivided into categories, such as affinity biosensors and catalytic biosensors, based on the activity of the biorecognition element [6]. Thus, affinity biosensors have as their fundamental property the recognition of the analyte by the biorecognition element (i.e. antibody-antigen). While, catalytic biosensors have as their biorecognition element proteins or microorganisms that not only interact with the analyte of interest but also catalyze a reaction resulting in the formation of a product [7, 8].

In Table 1.1 the ideal characteristics of a biosensor are summarized. In many cases, they are single-use devices, even if the requirements for reusable ones is desirable for many applications. An ideal biosensor is frequently described as being robust, selective, capable of reproducible responses and sensitive with a large dynamic range [9]. However, all these characteristics are rarely achieved.

Table 1.1. Ideal biosensor characteristics (Griffin and Stratis-Cullum, 2014).

Characteristic	Description
Analysis time	A fast analysis time is desired, with "real-time" responses to target analytes
Sensitivity	A sensitive analysis allows for detection of low concentrations of target analytes
Specificity	A specific analysis allows the discrimination between target analytes and other closely related species and minimizes false-positive analyses
Reproducibility	The analysis should be highly reproducible, to provide for a reliable analysis
Accuracy	The biosensor device should be highly accurate, meaning false-positives and false-negatives are minimized
Robustness	The biosensor should be insensitive to environmental conditions (temperature, pH, etc.)
Unit and operational costs	A lower unit cost and operational costs for reagents, and so on, will allow for a more wide spread implementation of the biosensor systems
Size and weight	The ability to miniaturize a biosensor is desired, particularly for integration into process monitoring applications as well as for portable applications
Regeneration	The ability to regenerate the binding surface, allowing multiple measurements by the same sensor element is preferable, although single-use platforms are sometimes sufficient
Multi-analyte detection	A biosensor that can detect multiple analytes simultaneously is highly desired for the efficient cost, time, size and weight utilization
User interface	Ideally, fully automated systems are desired or, at the minimum, require little-to-know operator skills for routine analysis

Bioanalytical systems, such as immunoassays like Enzyme Linked Immuno-Sorbent Assay (ELISA), which may use the same elements, should be distinguished from biosensors. Usually, they require additional processing steps and skilled workers, such as reagent addition,

washings and often reading the completed assay on specific instrumentation. Thus, the whole bioanalytical systems described in literature (i.e. immunoassays, nucleic acid-based assays, etc.) does not necessarily describe biosensors, although those techniques and methods usually represent a good starting point for the development of actual biosensors [10].

1.1.1. Assay Formats

From a general point of view, a variety of biorecognition elements can be used to establish specific interactions with a target of interest (see section 1.1.2) and different transduction elements can be employed for the detection of such interactions (see section 1.1.3). The association of different biorecognition-transducer elements allows to design several assay formats for biosensing purposes. Here is reported a brief overview of them.

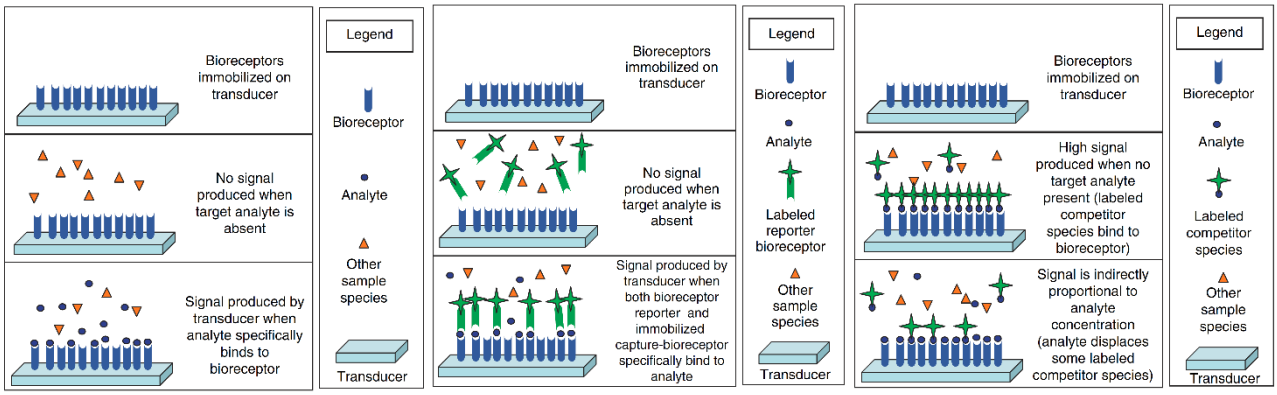

Fig. 1.2. Schematic representation of different assay formats (Adapted by Griffin and Stratis-Cullum, 2014).

The assay formats can be classified as direct or indirect. In the direct method, the binding event of the analyte to the biorecognition element is directly detected and related to the change of a measurable signal in the transducer such as a mass or a refractive index change, etc. Instead, the indirect techniques are all those assays that require an additional binding event (other than the biorecognition event) to occur in order to detect the bioreceptor-analyte interaction. This indirect method can be designed with a competitive or a non-competitive approach. In a competitive indirect strategy, the target of interest and a labeled

competitor molecule compete for a limited number of available bioreceptor binding sites [12]. In the non-competitive indirect strategy, a second bioreceptor with a label is put in contact with the analyte sample. Thus, the target of interest binds to the immobilized biorecognition element in the first instance and then the second bioreceptor is able to bind to the same target, establishing a specific double biorecognition on the same analyte molecule [12]. In the case of direct assays and non-competitive indirect assays, the signal is directly proportional to the analyte concentration, while in the case of competitive indirect assays, the signal is inversely proportional to analyte concentration [13]. Moreover, with the aim of increasing the sensitivity of the assay, biosensors usually involve the signal amplification: either the target molecules themselves may be amplified, such as in polymerase-chain reaction (PCR), or the biorecognition event may be amplified, such as in ELISA immunoassays.

Biosensors can be classified depending on the biorecognition element or on the type of transducer employed. From here on (section 1.1.2), the most used biorecognition elements are described. In the following (section 1.1.3), the most widely employed transduction mechanisms are described.

1.1.2. Biorecognition elements

The biorecognition element of biosensors has traditionally been some biological entity, with antibodies (Ab) being the most representative example [14]. However, others biomolecules may be employed for this purpose: bioreceptors such as enzymes, nucleic acids, and transmembrane receptors or larger biological units such as whole cells [10]. Indeed, the biorecognition element plays a crucial role in the overall biosensor performance and detection capability, being responsible for the selectivity against a particular analyte. Moreover, some artificial recognition elements as molecularly imprinted polymers (MIPs) or peptide nucleic acids (PNAs) may be included in this category, even if these are not natural biomolecules [15, 16]. In fact, in literature biosensors using such biorecognition elements, as aptamers, PNAs, liposomes and molecularly imprinted polymers (MIPs) are often reported. A brief description of the various types of biorecognition elements will now be given.

Antibodies

Antibodies are proteins produced by the immune system, which present antigen (Ag) recognition sites that specifically binds antigens by non-covalent interactions and with relatively high affinity. The antigen-binding domains of the molecule are the V_H (heavy chain - variable region) and the V_L (light chain - variable region) regions, which provide the specific antigen interactions with a sort of "lock-and-key" model [17]. Antibodies can be polyclonal and/or monoclonal, where a polyclonal antibody represents a collection of antibodies from different B cells that recognize multiple epitopes on the same antigen [17]. Each of these individual antibodies recognizes a unique epitope that is located on that antigen. A monoclonal antibody, by contrast, represents antibody produced by a single B cell and therefore only binds with one unique epitope [18]. Each individual antibody in a polyclonal mixture is in practice a monoclonal antibody; however, this term usually refers to a technique/method by which a specific antibody producing B cell is isolated and fused to an immortal hybridoma cell line so that large quantities of identical antibody can be generated [19]. Antibodies are probably the most commonly used of all biorecognition elements for sensor applications [14]. The so-called antibody sandwich strategy is frequently used in the design of biosensors, where capture antibodies immobilize the analyte, while other labeled antibodies bind to the analyte and thus provide a sensing signal [20]. It is also common to use some sort of amplification technique (e.g. enzymes-ELISA assays) to provide a more robust signal of the recognition process [21]. Combinations of nucleic acids and immunological techniques (e.g. immune-PCR and immune-rolling circle amplification) can also be used for amplification [22, 23].

Antibody fragments/engineered antibody fragments

For biosensing applications, the molecular recognition sites of the antibody are of fundamental importance, while the function of the Fc region may not be required for sensing applications, as its function is related to the physiological immune responses [24]. Moreover, antibodies are often immobilized on solid substrates and their orientation is as critical as the antigen epitope should be spatially accessible for antigen-antibody interactions. Thus, smaller antibody fragments may have certain advantages, such as more defined points of

immobilization through thiol groups liberated after cleavage of the whole immunoglobulin molecule [25]. In addition, these fragments could be more densely packed upon a sensor surface, increasing the epitope density over that achieved with immunoglobulins (Ig) and so enhancing sensitivity. Enzymatic cleavage of immunoglobulin molecules for the production of fragments such as Fab (antigen-binding fragment) is one way to obtain these smaller recognition elements. Using the techniques of phage display or ribosome display for antibody gene cloning and expression, antigen-binding fragments of antibody molecules called single-chain variable fragments (scFv) can be obtained [26, 27]. These fragments feature the V_H and V_L domains joined by a flexible polypeptide linker, which can be engineered to have desirable properties for immobilization (e.g. a thiol group of cysteine).

Enzymes

Enzymes are catalytic proteins, which have an active site that present a particular specificity for certain molecular structures, analogously to the antigen-binding sites of antibodies. This specificity, combined with the ability of the binding site to perform a precise chemical reaction, make these proteins extremely important in many different field of application. Furthermore, even in this case, genetically engineered enzymes with altered properties can be obtained. For example, an enhancement of the catalytic capability of the enzyme can be achieved [28]. In general, enzymes are not used as biorecognition elements *per se*, but are usually a component of a multiple molecular biorecognition mechanism, underlying the biosensor design. In this context, enzymes represent the element able to provide signal amplification, such as in ELISA immunoassays or coupling to an electrochemical detection transduction system [29, 30]. An example where an enzyme functions as a direct biorecognition element would be the use of cholinesterase enzymes to detect certain organic phosphate pesticides that are cholinesterase inhibitors [31].

Phage display/ribosome display

Bacteriophage are viruses able to infect and replicate into bacteria. They are made of an outer protein coating (capsid) that encloses the genetic material, which is injected into the bacterium. The phage genome is then used to direct the synthesis of phage nucleic acids and

proteins using the host's transcriptional and translational machinery [32]. For example, a biorecognition peptide can be expressed as the N-terminal add on to the phage coat protein. In this way, thousands of copies of the recognition element are exhibited on the capsid surface, increasing the density of the epitopes displayed. Therefore, the phage themselves serve as both biorecognition and amplification elements [33]. By using techniques developed in recent years, it is possible to produce and evolve peptides with strong binding affinity for specific proteins. These techniques include phage display and ribosome display. Briefly, in each techniques iterative rounds of affinity purification allow the *evolution* of peptides with desired binding properties for a specific ligand [34, 35]. The unique feature of phage display is that the production of 10^7-10^8 short peptides on the surface of filamentous bacteriophage can be achieved through the fusion of an epitope library of DNA sequences with the gene(s) coding for one of several coat proteins [36, 37]. In some cases, the bacteriophage may be labeled with fluorescent dyes in order to detect the binding events [38].

Nucleic acids

There are two types of nucleic acids: deoxyribonucleic acid (DNA) and ribonucleic acid (RNA). DNA is more frequently used in comparison to RNA due to its inherent greater stability under a variety of conditions [39]. In this case, the biorecognition process relies on the hydridization mechanism, in which two single strands establish non-covalent interactions between nitrogenous bases of complementary nucleic acids by Watson-Crick base pairing rules. Specificity is obtained due to the cumulative specific interaction of many bases to the complementary ones present on the other polynucleotide chain. Nucleic acid sensors are often coupled to amplification techniques of nucleic acid sequences with the potential for extreme sensitivity, since a large number of copies of an initially low copy number sequence can be obtained [40, 41].

Aptamers

Aptamers can also be included as nucleic acids biorecognition elements, since they are made up of single strands of nucleic acid (DNA or RNA), but here the biorecognition is not via base pairing but by folding to form a unique structure. In fact, aptamers are single-stranded DNA

or RNA (ssDNA or ssRNA) molecules than can bind to pre-selected targets including proteins and peptides with high affinity and specificity [42]. These molecules can assume a variety of shapes due to their propensity to form helices and single-stranded loops, explaining their versatility in binding to diverse targets. They are used as sensors and therapeutic tools (e.g. to guide drugs to their specific cellular targets), and to regulate cellular processes [43]. Contrary to the genetic material, their specificity and characteristics are not directly determined by their primary sequence. Instead, their features depends on their tertiary structure [44]. An advantage of aptamers over other kind of biorecognition elements, such as antibodies, is that the aptamer structure is inherently more robust than the antibody quaternary structure [45]. Thus, aptamers can be subjected to numerous rounds of denaturation and renaturation, providing an overall more robust biosensor as well as an option of easy regeneration of the sensor [46]. Moreover, aptamers are produced by chemical synthesis after selection rather than via immune system cells, and so can be readily modified to enhance stability and affinity [47]. Because of all these advantages, aptamers are being used increasingly as biosensor elements.

Peptide nucleic acids

PNAs are hybrid DNA-peptide molecules consisting of a series of N-(2-aminoethyl)-glycine units making up the backbone structure, instead of the sugar-phosphate backbone of natural nucleic acids, with the nitrogenous bases bound to this peptide backbone [48]. All intramolecular distances and configurations of the bases are similar to those of canonical DNA molecules, thus hybridization of PNAs to DNA or RNA molecules can be readily achieved. Since PNAs backbone is uncharged, double helixes formed by PNA and DNA molecules are more thermally stable than DNA-DNA duplexes [49]. This feature results in a more destabilizing effect of PNA-DNA hybrids in presence of single-base mismatches [50]. The application of PNAs in bionsensing field has been implemented because of the advantages that these molecules can provide. In fact, their structure remains stable over a wide range of temperature and pH range and resistant to nuclease and protease activity. Moreover, the use of PNAs for the direct detection of double-stranded DNA was possible due to the PNAs capability to form higher order complexes with DNA, such as three- and four-stranded complexes, eliminating the requirement for thermal denaturation [51]. Finally, contrary to

DNA molecules, PNAs can be incubated and immobilized on surfaces using saline buffers at low salt concentration in order to stabilize their structures in solution [52].

Molecular beacons

These molecules can be considered as a subset of nucleic acids used as biorecognition element: they are synthetic oligonucleotides designed to have a hairpin (stem-loop) structure [53]. The loop region presents a nucleotide sequence complementary to the analyte sequence to be detected. The stem region, instead, only contains a small number of complementary bases, forming a short double-stranded portion [54]. The detection of the analyte of interest relies upon a fluorophore and quencher mechanism: when the molecular beacon is in the closed position, the two molecules are held in close proximity on the two ends of the double-stranded structure of the stem region. Upon binding of the analyte sequence to the complementary sequence presents on the loop region, the stem structure opens and the quenching effect on the fluorophore is removed. Thus, the fluorescence signal reveals the presence of the analyte sequence [55]. Aptamers can be used also to design molecular beacon biosensors: these molecules are used to detect non-nucleic acid analytes, such as proteins or small organic molecules [56]. Even PNAs can serve as molecular beacon-type structures. In this case, PNAs assume a stem-less structure, which provide some advantages when compared to the initially designed DNA beacons: they are less sensitive to ionic strength and the quenching effect is not affected by DNA-binding proteins [57].

Cell Surface Receptors

Many of the molecular recognition events involved in cell-cell interaction, pathogen infection upon host cells, and so on, take place in the glycocalyx layer of the cell membrane [58]. This layer represents the coating on the apical surface of many cells that primarily consists of oligosaccharide headgroups of glycoproteins and glycolipids [59]. The hydrophobic portions of these biomolecules are embedded in the membrane bilayer, while the hydrophilic oligosaccharide chains protrude toward the outer environment. In some cases, pathogens and/or toxins target specific cell surface receptor sites [60]. Thus, these same receptors can be used as biorecognition elements. However, one of the major difficulties with the

application of these receptors for biosensing purposes is represented by the complexity of the cell membrane. Therefore, simpler models of cell membranes with a defined chemical composition include liposomes and Langmuir-Blodgett monolayers [61, 62].

Whole Cells

Among the different biorecognition elements, it is possible to employ entire cells in order to establish specific interactions with the analyte of interest. Cells are usually genetically modified in order to synthesize a certain marker that produces some sort of detectable signal, such as luminescence and/or fluorescence, when they are put in contact with specific compounds or environmental condition. This type of whole cell sensors have been applied for environmental analysis and monitoring purposes [63]. Examples of whole cell sensors use genetically engineered bacteria into which a lux gene, coding for a luciferase, is introduced under the control of an inducible promoter [64]. For example, Sayler and co-workers employed a whole cell sensor for the realization of a naphthalene biosensor: a genetically engineered *Pseudomonas fluorescens* was able to detect the biological availability of this molecule and salicylate in contaminated soil through the induction of the lux reporter [65]. Therefore, bioluminescence was the result of the expression of the reporter gene.

Liposomes

Liposomes are synthetic lipid vesicles that can be considered as cell membrane with a low grade of complexity [66]. Usually, liposomes are used as scaffold for the exhibition of standard biorecognition elements such as antibodies and/or oligonucleotides [67]. Moreover, other molecules such as fluorescent dyes, enzymes and electrochemically active species may be encapsulated into liposome structure and be released upon biorecognition event, representing a direct amplification system [68]. For example, the insertion of the ganglioside GM1 into these synthetic membranes has been used for the detection of cholera toxin, given the high specific interaction of the GM1/cholera toxin complex [69].

Molecularly imprinted polymers

Molecular imprinting is a technique, which can provide artificial molecular receptors. The procedure consists in the use of a target molecule as a molecular template in order to direct the assembly of monomeric units, which are subsequently polymerized with a cross-linker [70]. The type of interactions established by these molecular imprinted polymers (MIPs) are typically non-covalent interactions. In the first case, this imprinting scheme is able to interact with the molecule of interest through hydrogen bonding, Van der Waals forces and hydrophobic interactions [71]. During the polymerization of the monomeric units, the cross-linker freezes the binding groups in a specific orientation. After that, the target molecules are removed from the resulting polymeric matrix using suitable solvent or through chemical cleavage. In this way, the molecularly imprinted polymer presents a cavity, which is complementary in size to the analyte of interest [72]. MIPs have been demonstrated binding characteristics similar to those of antibodies and other receptors, but maintaining a much higher stability compared to natural biomolecules. Till now, the use of MIPs for detection purposes have been applied to the analysis of small molecules, while the interaction with larger biomolecules, such as proteins, or with entire micro-organisms represents a challenging task [73].

1.1.3. Transduction Mechanisms

The transducer is the biosensor component responsible for the transformation of the biorecognition event into a measurable signal. Usually, a change in a certain physical or chemical property is exploited. As reported above, biosensors can be classified on their transduction mechanism. Four mainly transduction formats can be identified: piezoelectric, calorimetric, electrochemical and optical transduction [13] (Fig. 1.3).

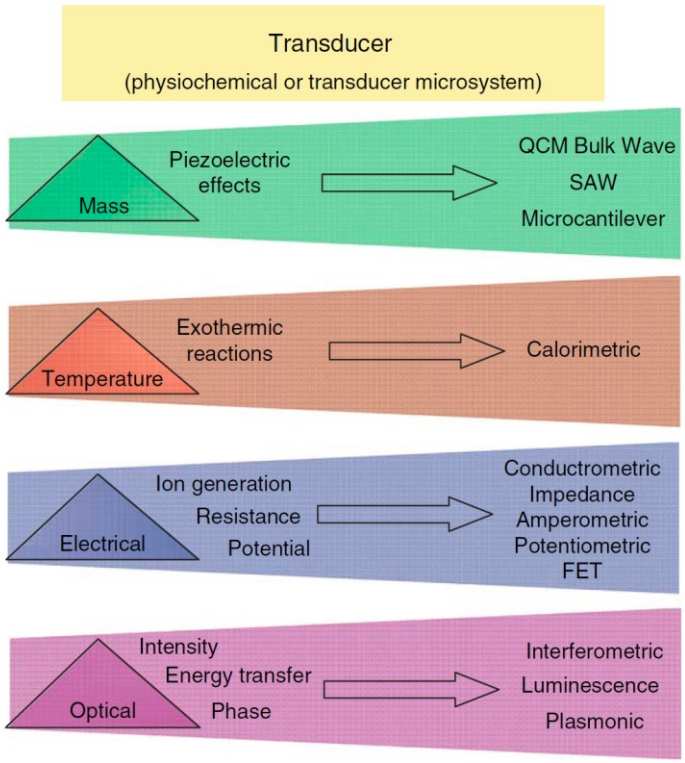

Fig. 1.3. Schematic representation of biosensors transduction types (Griffin and Stratis-Cullum, 2014).

Electrochemical

The electrochemical transduction is one of the most widely used for biosensing [74]. Electrochemical biosensors can be divided into three main categories: potentiometric, amperometric and impedance [75]. Potentiometric sensors use the variation in the potential produced by electroactive species, which is measured by an ion selective electrode. In the case of a biosensor application, an enzyme is usually the responsible for the change in electroactive species concentration [76]. In amperometric biosensors, the production of a current resulting from the oxidation or the reduction of an electroactive biological element when a potential between two electrodes is applied and continuously monitored [77]. Many examples can be found in literature [78-80]. In impedance sensors, the variation in the charge transfer and/or capacitance at the sensor interface layer is measured after the application of controlled AC electrical stimuli with specific frequencies [81].In biosensing application, metabolic changes related to growth and cell metabolism have been shown to correspond to an impedance variation [82].

Piezoelectric

Biosensors able to use the mass variation related to the interaction between the biorecognition element and the target molecules predominantly rely on piezoelectric transduction [83]. The piezoelectric effect consists in the production of electrical charges by applying a mechanical stress and vice versa. This phenomenon may be used to relate the change in mass with the biorecognition binding event. The main advantages of mass sensors is represented by the possibility to perform label-free measurements of the binding events, including binding kinetics analysis [84].

Quartz crystal microbalance

Quartz crystal microbalance (QCM) device consists of a quartz disk that is plated with electrodes and its working mechanism relies on the propagation of an acoustic wave across the device upon introduction of an oscillating electric field [85]. The binding-induced mass change causes the decrease in the oscillation frequency, which is related to the amount of interacting target molecules. The QCM device may be used with several bioreceptors, such as antibodies, nucleic acids and MIPs. However, these devices are not suitable for the detection of small molecules at low concentrations and require the immobilization of an amount of bioreceptors large enough to produce a measurable variation in the recorded signal [86].

Surface acoustic wave

Similarly to QCM devices, surface acoustic wave (SAW) sensors are piezoelectric crystals that detect the mass of interacting target molecules, which causes a change in the resonant frequency of the sensor. SAW devices can directly sense the binding-induced mass changes, exhibiting an increased sensitivity compared to bulk wave devices [87]. However, the acoustic wave dumping effects recorded in biological solutions limit its utility in biosensing applications. Thus, devices able of reliable detection would require improvements in sensitivity [88].

Micro- and nanomechanical cantilevers

Micro- and nanomechanical cantilevers can be used as mass sensors and can be manufactured using silicon micromachining techniques. The modification of the cantilever surface with bioreceptors allows the recognition of target analytes [89]. This binding-induced mass change produces a change in the resonant frequency, giving the possibility of label-free detection of target molecules maintaining low cost and mass production of the devices [1] (Fig. 1.4). As previously reported for SAW-based sensors, cantilever-based biosensors sensitivity is limited by dampening in liquid solutions when compared to cantilever systems operated in air and vacuum conditions. Recent works reported for the incorporation of a hollow channel inside the cantilever structure [90]. In this way, high resonant efficiency can be obtained through the use of static vacuum packaging and the mass changes can be monitored while the samples are flowing inside of the device. Another strategy involves the use of nanoparticles and magnetic beads for signal amplification purposes, causing larger frequency shifts [4].

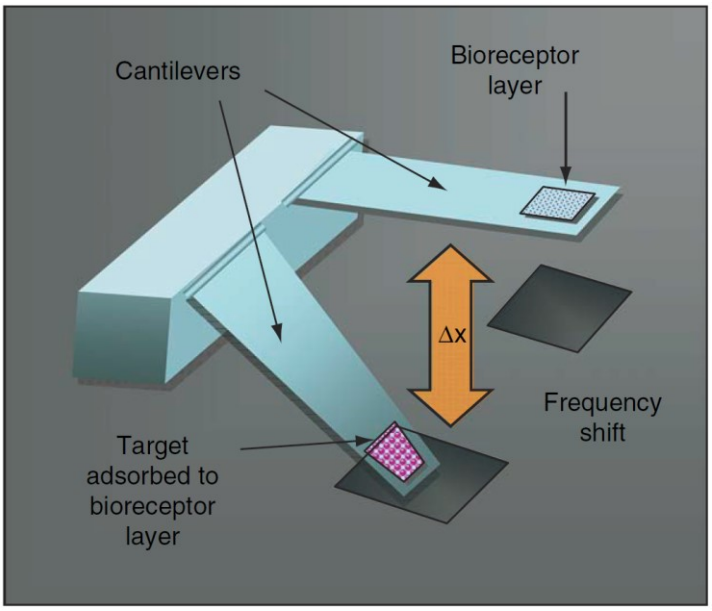

Fig. 1.4. Schematic representation of a microantilver-based biosensor (Boisen et al., 2011).

Calorimetric

Calorimetric sensors consists in the use of thermistor probes for the monitoring of temperature changes caused by exothermic chemical reactions [91]. Biological reactions such

as enzyme reactions are exothermic, thus this type of device provides a universal transduction format for reactions involving these biological catalysts. The main drawback of sensors based on such mechanism is related to the environmental temperature fluctuations. Therefore, the sensor system must be shielded from these fluctuations in order to maintain a constant temperature during the detection event [92].

Optical

The optical transduction is another widely used biosensor type format [93]. In fact, optical-based sensors are very rapid and, usually, the diffusion process related to the biomolecular recognition event represents the only limiting factor in the speed of the detection procedure. The disadvantages of using optical sensors include the detection difficulties reported when analyzing turbid samples and the costs associated with the detection system components. Optical-based sensors use the change of the light interaction with the biomolecular component in order to generate a measurable signal. These changes are related to different properties of light such as refractive index, production of chemiluminescent products, fluorescence emission, fluorescence quenching, radiative and non-radiative energy transfer and scattering techniques [13]. These effects can be monitored using a wide variety of instrumentation such as total internal reflectance and evanescence wave technologies, interferometry and resonant cavities just to cite a few examples [94]. Some examples of the most used optical-based mechanisms implemented in the realization of sensing devices will be described in the following sections.

Fluorescence

Fluorescence is one the most popular optical transduction because of its high sensitivity. Typically, a fluorogenic molecule is used to label a biorecognition component in order to create a bioreporter. The monitoring of the bioreporter signal gives information about the presence and concentration of the analyte of interest. The binding interaction between the reporter and the target can produce shift in the wavelength of the fluororeporter or energy transfer phenomena, which may be recorded for time dependence analysis of biological phenomena or for the study of structural conformational changes of target molecules [95-97].

Moreover, fluorescence detection can be coupled to other techniques and methods. For example, fluorescence has been coupled to cytometry and microfluidic platforms or biochips systems that use imaging arrays methods, in which fluorescence signals related to biological recognition elements are matched to target species [98]. Fluorescence-based techniques do not have the interference issue that Surface Plasmon Resonance (SPR) and other refractive index-based methods present (see below). However, the disadvantages are related to the intrinsic sample fluorescence, which may not be sufficient for a sensitive analysis.

Chemiluminescence

Chemiluminescence relies on chemical reactions, which finally produce a characteristic photon [99]. These series of chemical reactions usually involves the oxidation of luminol. The intensity of the produced light is proportional to the presence of the target of interest because the resulting products are conjugated to the biorecognition element, which is used as chemiluminescent reporter. The advantages of this method is the very low background signal, mainly due to non-specific interactions during the bioassay procedure, which may require multiple washing and incubation steps [100].

Surface plasmon resonance

Surface plasmon resonance (SPR) is a physical phenomenon that can be established at a metal/dielectric interface. After passing through a high refractive index prism, the polarized light produces an evanescent wave, which has a maximal intensity at the interface and exponentially decays in relation with the distance from the interface. The intensity of the reflected light is monitored as a function of the angle of incidence. This intensity displays a minimum, in which the energy of the evanescent wave is absorbed by the surface plasmons in the metal. The bioreceptor/analyte binding events established at the interface cause a change in the refractive index at the interface, resulting in a change in the resonance excitation of the surface plasmon [101]. A schematic representation is illustrated in Fig. 1.5.

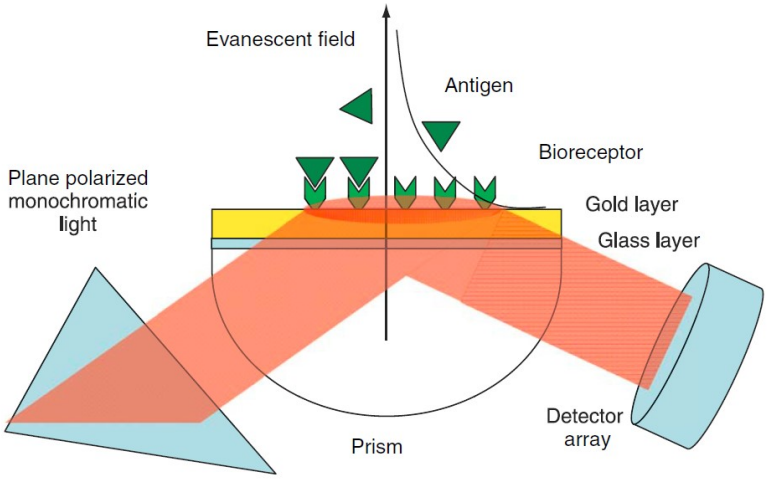

Fig. 1.5. Schematic representation of a SPR set-up (Boisen et al., 2011).

In Fig. 1.5 is illustrated a SPR set-up, consisting of a prism with a gold layer upon which the biorecogniton elements are immobilized. The polarized light is totally internally reflected by the gold coated face of the prism and the reflectivity is monitored during the binding events. Surface plasmons can be excited with a specific angle of incidence, corresponding to a reduction of reflectivity at that specific angle [102]. Therefore, the change in the refractive index at the interface causes a variation of the angle required for an optimal excitation. SPR technique are widely used in biosensing applications because it allows to perform a label-free real-time analysis with good sensitivity [103]. However, all the phenomena that cause the change of the refractive index at the sensing surface may interfere with the analysis of the target of interest. Such limitations include analytes dissolved in a non-homogeneous matrix and non-specific interactions [104].

Surface enhanced Raman spectroscopy

Surface Enhanced Raman Spectroscopy is a spectroscopy technique that has recently acquired popularity in biosensing applications [105]. SERS is a scattering technique in which a rough metal surface is use to enhance the scattered Raman signal. SERS is a phenomenon associated with the enhancement of the localized electromagnetic field surrounding molecules optically excited near an intense and sharp plasmon resonance. This field enhancement localized at the metallic surface can be used to boost the Raman scattering signal of the immobilized

molecules [106]. The main advantages of SERS is the possibility of obtaining a spectroscopic fingerprint of the immobilized molecules, similarly and complementary to the one obtained by Infrared Spectroscopy. Moreover, it can be used for the detection of very low concentration of biomolecules, as reported in several works in which an immune-based SERS technique is used for the detection of different targets [107]. The disadvantages of the technique are represented by the signal reproducibility difficulties, which are related to the nanostructures SERS substrate fabrication [108]. Indeed, many researchers fabricate their SERS substrates, even if commercially available ones can offer a more consolidated strategy.

1.2. Cantilever as mechanical sensor

Cantilever-based sensing has rapidly increased starting from the half of the 1990 decade. It is the most promising sensing platform for the realization of label-free, sensitive, portable, cheap and fast sensors. In particular, cantilever structures at the micro scale got a lot of interest as point of care (POC) diagnostics and environmental monitoring devices. Moreover, they can be used in fundamental research given the fact that microcantilever can be used as tool for the study or quantification of physical phenomena which cannot be evaluated by other methods. With this goal, microcantilever sensors are versatile devices, which can be used in different modes providing unique information. For example, these sensors are able to detect the change in surface stress, temperature and mass. Microcantilevers were first introduced in 1986, with the discovery of atomic force microscope [109]. AFM is a topographical technique, which allows to scan a surface using a cantilever probe. This probe consists of a cantilever structure and a sharp tip mounted on the free end of the beam. During the topographical analysis, the AFM probe deflects due to the forces between the sample and the tip. The first report of a cantilever structure as a sensor is from Thundat and colleges [110] that used a microcantilever as a very sensitive thermometer. In particular, the change in temperature was detected by an AFM probe coated with a metal layer on one side: the coefficient of thermal expansion of the different materials resulted in the deflection of the cantilever, which can be related to a temperature change. Few years later, the surface stress change resulting from the non-specific binding of proteins was reported [111]. Moreover, the live measurement of the surface stress was demonstrated for a gold-coated cantilever incubated with alkanethiols: it was possible to see the deposition of a self-assembled monolayer (SAM) in real time [112]. An array of polymer-coated cantilevers was used for the detection of various alcohols; the bending and the resonant frequency of each cantilever were monitored [113]. At the beginning of 2000, the detection of a single-nucleotide polymorphism – i.e., two oligonucleotides that differ for a single base mismatch – was reported using a microcantilever-based sensor [114].

1.2.1. Sensing Principle

Cantilever-based sensors can be used in two different operating modes (Fig. 1.6). In the so-called static mode, the static deflection of the cantilever is monitored and related to the differential surface stress of the two faces of the beam. In the dynamic mode, the resonant frequency of cantilevers is monitored: the adsorption of mass on the beam structure is related to the resonant frequency as the resonant frequency of the cantilever decreases as the mass increases. Therefore, it is possible to make a mass estimation using the resonant frequency shift of the cantilevers.

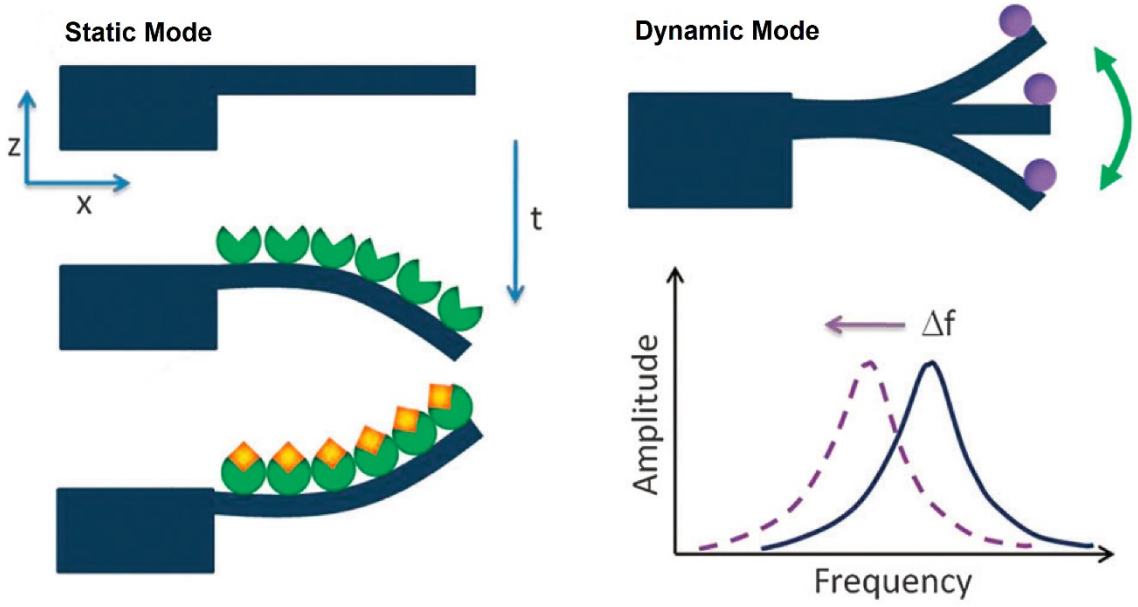

Fig. 1.6. Schematic representation of microcantilevers operating modes (Tamayo et al., 2012).

Static Mode

In the static mode, the interactions established between molecules immobilized on one face of the cantilever structure are able to generate a surface stress. The Stoney equation allows to calculate surface stress of a thin film deposited onto a sheet of metal [115]

$$R = \frac{\hat{E}h^2}{6\sigma(1-v)} \tag{1.1}$$

where R is the radius of the curvature, $\hat{E}$ is the Young's modulus, h is the thickness of the deposited film, σ is the surface stress and υ is the Poisson's ratio. Starting from this equation, Jaccodine and Schlegel [116] were able to elaborate an equation to be applicable to cantilever structures (i.e. single clamped beams). In this case, it is possible to relate the bending of the beam with the surface stress as

$$\Delta z = \frac{3(1-\upsilon)L^2}{\hat{E}h^2}\sigma \tag{1.2}$$

where Δz is the cantilever deflection and L is the length of the cantilever. Surface stress phenomena are reported in Fig. 1.7. In the first case, a compressive stress of the film is illustrated: the cantilever bends downwards and its structure expands until the stress balances the one of the thin film. In the second one, a tensile stress causes the cantilever to bend upwards because of the contracting thin film.

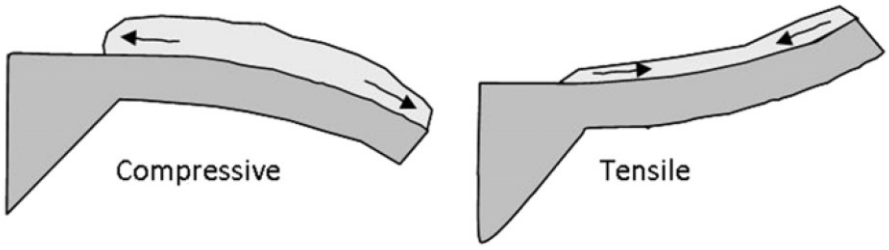

Fig. 1.7. Schematic representation of compressive and tensile surface stress (Boisen et al., 2011).

Dynamic Mode

In the so-called dynamic mode, single clamped beams are used as weighting devices for the detection of small molecules. The sensitivity or minimum detectable mass depends on the ratio between the mass and the resonant frequency of the beam: as the dimensions decrease, the resonant frequency increases. Therefore, a strategy to enhance the sensitivity of the

sensing platform is to decrease the dimensions of the cantilever structure. In literature are reported devices able to detect mass in the atto- (10^{-18}) and zepto- (10^{-21}) gram range [117, 118]. Thus, cantilever-based systems sensitivity demonstrated to be better than the one reported for other methods capable of detecting mass, such as QCM [119].

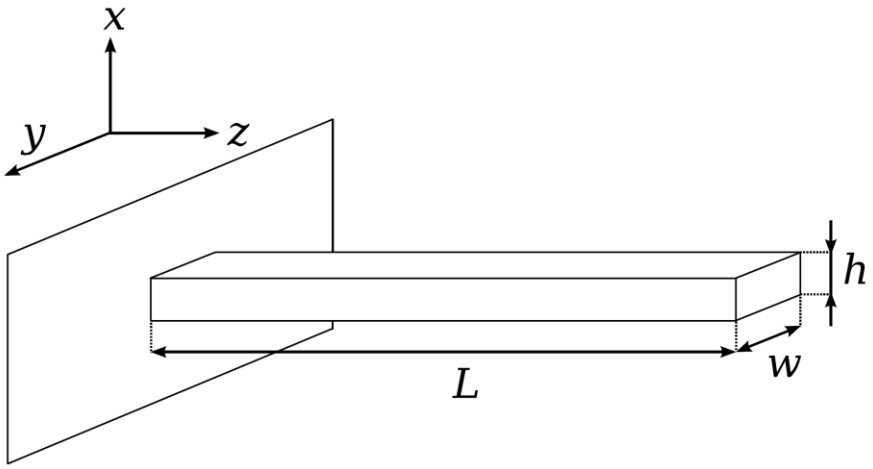

Fig 1.8. Schematic representation of a rectangular cantilever structure.

For a thin beam structure, in which the relationship $L >> w >> h$ is true, it is possible to approximate the behavior of the system using the Simple Harmonic Oscillator (SHO) differential equation [120]

$$m\frac{\partial^2 x}{\partial t^2} + C\frac{\partial x}{\partial t} + kx = f \tag{1.3}$$

where k is the spring constant of the oscillator, f is the force and C is a coefficient related to friction and damping effects. In this case, a unique resonant frequency is given by

$$f = \frac{1}{2\pi}\sqrt{\frac{k}{m}} \tag{1.4}$$

For an infinitesimal change of the mass,

$$f = \frac{1}{2\pi}\sqrt{\frac{k}{m}} = \frac{\sqrt{k}}{2\pi}m^{-\frac{1}{2}}$$
$$\delta f = \frac{\sqrt{k}}{2\pi}\left(-\frac{1}{2}\right)m^{-\frac{3}{2}}\delta m = -\frac{1}{2m}\left(\frac{1}{2\pi}\sqrt{\frac{k}{m}}\right)\delta m = -\frac{f}{2m}\,\delta m \tag{1.5}$$

Therefore, substituting infinitesimal deviations with experimental finite but small variations, it is possible to obtain the following relationship:

$$\frac{\Delta f}{\Delta m} = -\frac{f}{2m} \tag{1.6}$$

However, this model presents some obvious limitations due to the fact that a vibrating cantilever is not described by a spring with a punctiform mass and dissipation. The equation of motion that describes the behavior of a cantilever in vacuum is the Euler-Bernoulli equation [121]:

$$\rho A\frac{\partial^2 v(x,t)}{\partial t^2} + C\frac{\partial v(x,t)}{\partial t} + \hat{E}I\frac{\partial^4 v(x,t)}{\partial x^4} = F_{ext} \tag{1.7}$$

where $v(x,t)$ is the displacement in the x-direction, ρ is the mass density, $A = wh$ is the cross-sectional area, $\hat{E}$ is the Young's modulus and I is the moment of inertia.

The equation (1.7) do not have closed-form solutions, thus it is possible to define the solutions of the transcendental equation

$$cos(\lambda_n)\,cosh(\lambda_n) + 1 = 0 \tag{1.8}$$

from which it is possible to obtain the resonant frequency for the different vibrational modes

$$f_n = \frac{1}{2\pi}\left(\frac{\lambda_n}{L}\right)^2 \sqrt{\frac{\hat{E}IL}{m}} \tag{1.9}$$

Therefore, the infinite modes of vibration of cantilever present themselves in an aperiodic manner and with decreasing amplitude. The resonant frequencies of the first vibrational modes are illustrated in Fig. 1.9.

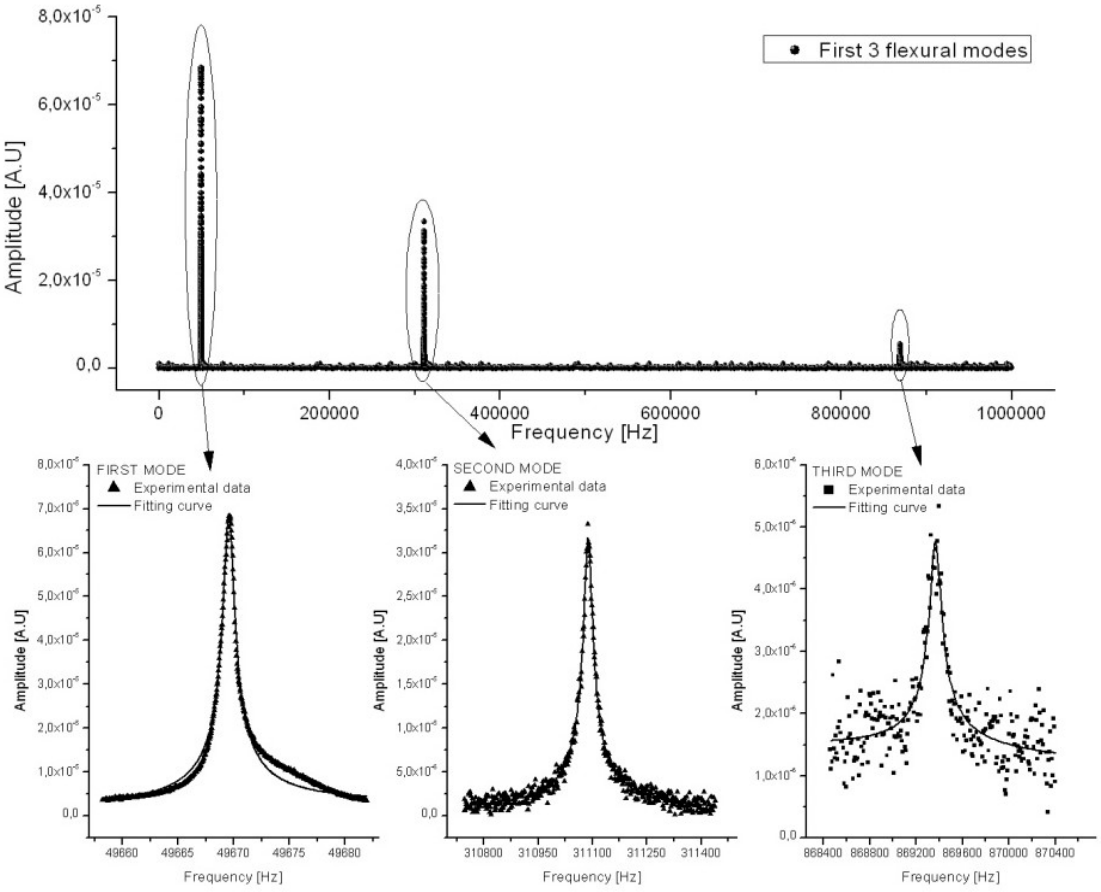

Fig. 1.9. Experimental acquisition of the first three vibrational modes of a cantilever resonator.

The decrease in amplitude of the vibrational modes occurs because, as the mode increase, nodes are added to the vibrating structure of the beam, that is non-vibrating points which limit the oscillating behavior of the cantilever. Thus, the oscillating mass decreases and the

beam stiffness increases as the resonant frequency increases. Generally, a cantilever vibrating at the *n*-mode presents *n*-1 nodes.

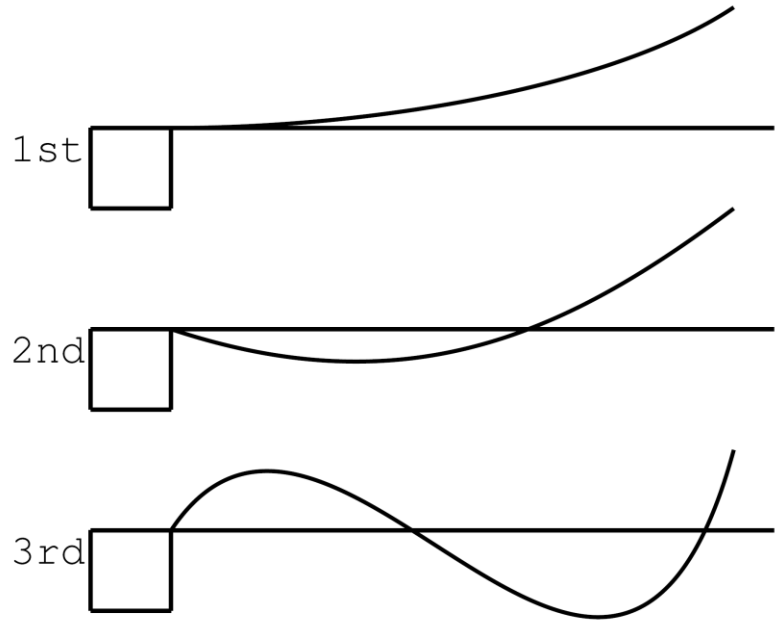

Fig. 1.10. Schematic representation of the vibrational profile of the first three vibrational modes of a cantilever resonator.

It is possible to use the SHO model, introducing the effective mass parameter $\boldsymbol{m_{eff}}$ which for the first mode is equal to

$$m_{eff} \approx 0.25m$$

In this way, the frequency of the first mode of vibration is

$$f_1 = \frac{1}{2\pi}\sqrt{\frac{k}{m_{eff}}} \tag{1.10}$$

The mass change after the deposition of a molecule with mass *m** on the cantilever surface, causes the resonant frequency change

$$f_2 = \frac{1}{2\pi}\sqrt{\frac{k}{(m+m^*)_{eff}}} \tag{1.11}$$

$$\Delta f = f_2 - f_1$$

and the relationship between the mass change and the frequency shift is

$$\Delta m \approx -2\frac{\Delta f}{f}m \tag{1.12}$$

This approximation can be used only if the external vibrating force is negligible, avoiding non-linearity in the oscillating behavior. In fact in a non-linear oscillating regime, cantilever is non able to instantaneously dissipate the energy accumulated during the oscillation of the structure. Thus, the cantilever stiffness increases and the vibrational modes are orthogonal no more.

A parameter which defines the cantilever capability of instantaneously dissipate the accumulated energy is represented by the Quality Factor (*Q*). It is defined as the ratio between the resonant frequency and the frequency interval in which the amplitude of the oscillation is at -3 dB of the maximum amplitude, that is reduced of a factor $\frac{\mathbf{1}}{\sqrt{\mathbf{2}}}$.

$$Q = \frac{f_r}{(\Delta f)_{-3dB}} \tag{1.13}$$

Although not exactly coincident, the Quality Factor for Lorentzian curves is often calculated as the ratio between the resonant frequency and the Full Width at Half Maximum (FWHM), that is the frequency interval in which the amplitude of the oscillation is equal to $\frac{\mathbf{1}}{\mathbf{2}}$ of the maximum amplitude.

$$Q' = \frac{f_r}{FWHM} \tag{1.14}$$

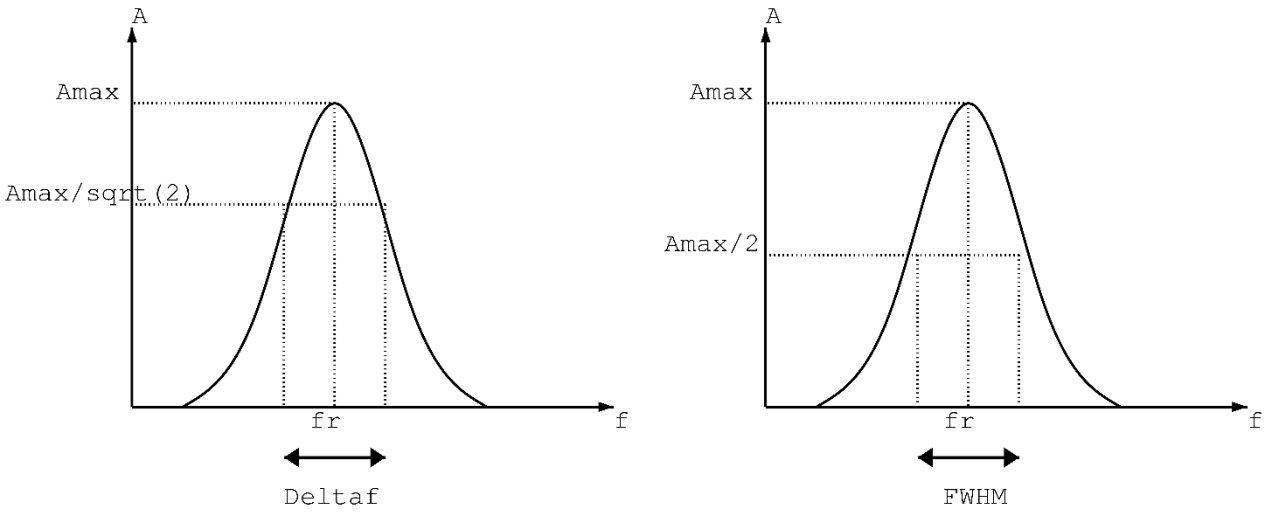

Fig. 1.11. Schematic representation of the Q factor calculation.

The theoretical mass sensitivity is another important parameter, which is defined as

$$S_m = \frac{\Delta f_n}{\Delta m} = -\frac{f_n}{2m_n} \tag{1.15}$$

From an experimental point of view, the Quality Factor should be also taken into account, so that the minimum detectable mass can be defined as

$$\Delta m_{min} \propto \frac{m_n}{Q} \tag{1.16}$$

Thus, it is possible to increase the mass sensitivity decreasing the mass of the resonator, that is reducing the dimensions of the cantilever and/or increasing the Quality Factor.

1.2.2. Cantilever fabrication

Cantilevers can be fabricated in silicon or using polymers and it is important to notice that the fabrication process results to be very different for these two materials. When fabricating free-standing beams, some requirements exists independently of the material used for the realization of the cantilever structure:

The cantilevers mass should be decreased in order to enhance the sensitivity of the sensing platform.

For dynamic mode operated cantilevers, the material should display low internal damping and the geometrical shape of the beam should account for high Quality Factor.

The cantilever dimensions and geometries should be precisely controlled because of the relationship between the mass of the resonator and its sensitivity.

Because of the majority of applications of such sensing platform use an optical read-out for the bending and/or resonant frequency monitoring, cantilevers should be reflective and the surface should be as smooth as possible in order to avoid the scattering of light.

Silicon devices

One of the most widely used material for the fabrication of cantilevers is silicon, because of the microfabrication processes applied in the ICT industry. In fact silicon, silicon nitride and silicon oxide are stable materials that can be used in different temperatures and environmental conditions. Typically, microcantilevers present dimensions that ranges from 1 to 10 µm in thickness and from 450 to 950 µm in length.

Bulk micromachining technique

Clean-room fabrication processes are applied for the realization of micro-sized cantilevers. The approach that consists in the selective etching of silicon substrate from the backside of a wafer to the device is called bulk micromachining [122]. This process can be divided into three main steps: the first one corresponds to the preparation of the silicon substrate, followed by

the definition of cantilever geometry and, finally, the release of the device into a suspended configuration.

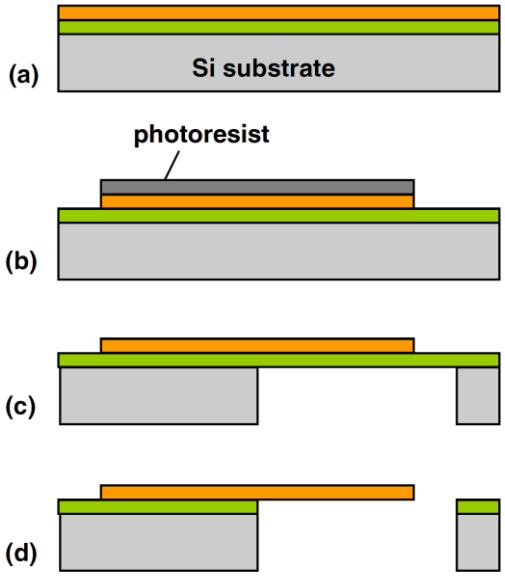

Fig. 1.12. Schematic representation of microcantilver fabrication process using bulk micromachining techniques (Boisen et al., 2011).

As illustrated in Fig. 1.12, during the first step the deposition of thin films is performed on a silicon wafer. The material used could be silicon nitride, silicon oxide or polysilicon. In particular, two layers are deposited. The outer layer is the one corresponding to the cantilever device and it defines the thickness of the beam structure, while the intermediate one represent the so-called stopping layer, which is used to protect the outer layer during the etching of the silicon substrate and to maintain the previously defined thickness of the cantilever structure. A common approach consists in using a Silicon-On-Insulator (SOI) wafer, which present a silicon oxide intermediate layer. The cantilevers geometry is defined by means of an optical lithography, in which the photoresist material is patterned by UV exposure on the front side of the wafer [123]. For cantilevers at the nanoscale, an electron beam lithography is used, in order to have a more controlled definition of the planar geometries [124]. The pattern is transferred to the wafer device layer by wet etching or Reactive Ion Etching (RIE), while the bulk substrate etching is typically achieved using a wet KOH etching or using the Deep Reactive Ion Etching (DRIE) technique. The last step consists in the remove of the sacrificial layer, in order to release the cantilever structure.

Polymer devices

Polymer-based devices have been reported in literature as static sensors because of their Young's modulus, which demonstrated to be two orders of magnitude lower than the one displayed by silicon-fabricated cantilevers. Moreover, the use of polymers allows to reduce costs of the fabrication process. For example, in 1999 the use of SU-8 photoresist for the realization of AFM probes was reported [125]. In this case, SU-8 Young's modulus is as low as 4 GPa, which make it a promising material for the realization of cantilever-based surface stress sensors [126]. Other polymers such as polyimide [127], polystyrene [128], polypropylene [129] and polyethylene therephtalate [130] have been evaluated for the fabrication of cantilever sensors.

Surface micromachining technique

The surface micromachining is a fabrication approach, which relies on the deposition of several layers on a surface in order fabricate free-standing structures [131]Typically, this strategy consists in the presence of a sacrificial layer, on top of which the deposition of the device layer is performed. Common methods of the deposition of the material are represented by spin-coating and chemical vapor deposition (CVD). In Fig. 1.13 are illustrated the main steps of the fabrication process.

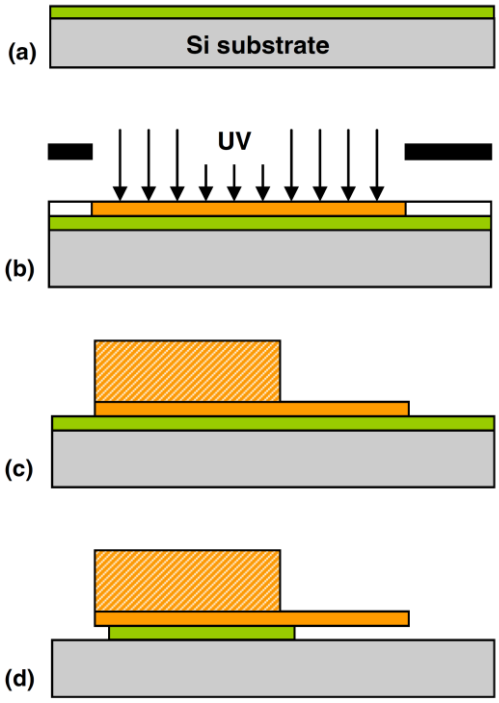

Fig. 1.13. Schematic representation of microcantilver fabrication process using surface micromachining techniques (Boisen et al., 2011).

In order to define the geometry of the polymeric cantilever, several methods can be used such as UV-photolithography. In this case, the polymer must be a photoresist such as SU-8 or polyimide [132, 133]. The polymer deposition is performed through spin-coating, then the polymer is baked and exposed to UV-light. Another strategy consists in the combination of standard lithography and polymer etching techniques. For example, the use of an oxygen-plasma etching to define the planar geometry was successfully applied for the fabrication of a cantilever-based platform made of parylene and polyimide [134, 135]. Moreover, a fabrication process involving a nanoimprint lithography has been reported [136]. After the definition of the chip body, the cantilevers structures are released by removing the sacrificial layer previously deposited. Traditionally, this step consists in a selective etching of the material: wet etching and dry etching demonstrated to be available options [137, 138]. Usually, a major problem of these procedures is represented by the small gap between the cantilever and the substrate, with increasing risk of stiction phenomena [139].

3D fabrication

The fabrication of microcantilevers were reported by McFarland and co-workers using a micro-moulding. Different materials such as polystyrene, polypropylene and nanoclay were investigated [140, 129].

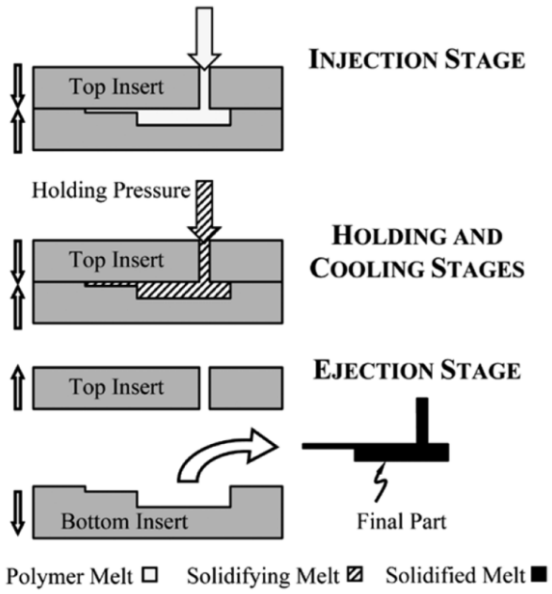

Fig. 1.14. Schematic representation of microcantilver fabrication process using micro-moulding technique (McFarland and Colton, 2005).

Other patterning methods that were investigated are laser ablation, microstereolithography and multi-photon-absorption polymerization [130, 141, 142].

1.2.3. Actuation systems

Different techniques have been implemented to actuate cantilevers, taking in consideration the read-out system employed. Typically, the actuation system is represented by an external piezoelectric platform on which the device is mounted and put into vibration at a certain frequency. In others configurations, the actuator can be miniaturized and integrated within the sensor. The actuation systems include electrostatic actuation, thermal actuation and magnemotive actuation. In the electrostatic actuation the cantilever is put in proximity of an electrode on which an alternating voltage is applied, creating a periodic electrostatic force on the cantilever [143]. In the thermal actuation, an integrated resistive heater or an external laser are used to heat a bimorph cantilever in a pulsed manner [144]. In addition, natural

thermal vibrations of the beam temperature can be used [145]. In the magnetomotive actuation, a static magnetic field is applied perpendicular to a cantilever through which an alternating current is running. The Lorentz forces will thereby cause the cantilever to deflect [146].

1.2.4. Read-out systems

The deflection of the cantilever must be monitored during the measurement sessions; in order to do so, different methods has been implemented: some of them demonstrated to be robust techniques but with the require of large instrumentation, while others resulted in less reliable measurements but promising for their implementation into portable devices.

Optical read-out

The optical lever technique is the most used read-out system for cantilever-based sensors. A laser is focused at the cantilever free end and it is reflected off towards a position sensitive detector (PSD). This technique is able to reach a resolution under the nanometer displacement. However, this type of set-up cannot provide the simultaneously detection of an array of cantilever. In order to do so, an array of eight vertical cavity surface emitting lasers (VCSELs) was used for the monitoring of an array of equally spaced cantilevers [147]. The laser spots reflected by the cantilever structures are collected by a photodetector that can track the displacement of each corresponding cantilever. Another read-out system consists in the use of an expanded and collimated laser beam to illuminate an array of cantilevers. The reflected light is collected by a HR CCD camera [148]. Even though this method allows to acquire the displacement information from several cantilever simultaneously, the equipment required for the measurements is bulky and the resolution obtained is limited by the resolution of the camera employed. Another way to track the beam deflection is represented by the use of an interferometric system, which exploit the Doppler effect for the measurement of the velocity of dynamic mode operated microcantilevers; moreover, the same system can be used for the reconstruction of the profile of a bent cantilever [149]. Another application of the VCSELs technology as a read-out system consists in the formation of a so-called external

cavity between the laser and the cantilever. In fact, the light from the laser is reflected back into the VCSEL generating an interference signal [150].

Capacitive read-out

The change in the capacitance between two electrodes is exploited to monitor the deflection of cantilevers. In particular, a cantilever placed in close proximity to parallel electrodes causes a capacitance change, which can be related to the deflection of the beam [151]. The application of this read-out system for sensing purposes can be achieved starting from a SOI wafer, in which the buried oxide layer acts as sacrificial layer and defines the space between the cantilever and the electrode [152]. The capacitance changes are in the pF range, thus this type of read-out system require a precise control in the fabrication process in order to correctly define the spacing between the beam structure and the counter electrode. The main advantage of this read-out system is that it provides a method that does not require the modification of the cantilever structure, thus without affecting the mechanical properties of the sensor.

Piezoelectric read-out

Piezoelectricity consists in the generation of an electrical potential caused by a mechanical stress across a piezoelectric material and vice versa. This physical phenomena has been widely used as actuation and read-out system in dynamic mode operated cantilever-based sensors. The differential deposition of piezoelectric material on cantilever surface has been implemented for both AFM and sensing purposes. In particular, the first report of a zinc oxide film deposited on one side of an AFM probe was from Itoh and Suga in 1993 [153]. Another AFM piezoelectric read-out was demonstrated using a lead zirconate titanate (PZT) thin film [154]. The same PZT material was coated on a silicon nitride cantilever sensor designed for the detection of PSA and the DNA of the Hepatitis B virus [155, 156]. The piezoelectric read-out has the advantage of being scalable and presents a low power consumption. However, the disadvantage is represented by the difficulty to work with these materials. Moreover, most of them are not clean-room compatible.

Piezoresistive read-out

In piezoresistive read-out, the beam structures are fabricated with an integrated resistor, which displays piezoresistive properties: as the cantilever bends, it causes a change in resistance. Therefore, the resistance change is related to the deflection of the beam. This method can be used both in liquid and air and can be applied for static and dynamic operated cantilever sensors as well. Initially, this read-out system was integrated into an AFM set-up [157, 158]. Cantilever-based sensors with piezoresistive read-out for the detection of glucose and saccharide were reported [159, 160]. Typically, a Wheatstone bridge is used to connect a reference and a measuring cantilever in which the resistors were integrated [161]. In this way, the signal is generated only if there is a differential response arising from the two cantilevers, significantly reducing the noise. Moreover, this read-out system is easily integrated with CMOS for signal processing and amplification [162].

1.2.5. Biosensing applications

Microcantilevers represents a promising sensing platform because of their high sensitivity and rapid response. This sensing platform has been successfully used for the detection of proteins, pathogens, DNA and other small molecules [163-165]. In the following sections, a brief overview of the major achievements involving microcantilever-based biosensing will be given.

Proteins

Different microcantilever-based biosensors have been applied for the detection of proteins in various environments. In 2003, Arntz et al. reported the label-free detection of creatine kinase and myoglobin using a static-mode operated cantilever sensor [166]. The achieved sensitivity was below 20 mg/mL. Few years later, Wee and co-workers reported the use of a piezoresistive cantilever sensor for the detection of prostate specific antigen (PSA) and C-reactive protein at different concentrations (10 ng/mL, 100 ng/mL, and 1 μg/mL), obtaining a proportional resistance signal as output of the sensor [167].

Waggoner et al. used arrays of dynamic mode operated nanomechanical resonators for the detection of PSA. The protein was revealed in a complex matrix such as fetal bovine serum, using a nanoparticle-based sandwich assay [168].

Pathogens

Ilic and co-workers described the application of a cantilever array for the detection of *Escherichia coli* cells in vacuum, using a selective anti-*Escherichia coli* antibody [145]. The same authors reported the use of a resonating cantilever for the detection of *Baculovirus* by means of a specific antibody. The sensor was dipped into a virus containing solution at different concentrations and the sensing platform was able to detect frequency shifts related to exposure to 10^5 pfu/mL of *Baculovirus* [169]. In 2007, Maraldo et al. successfully developed a cantilever sensor able to detect the pathogen *Escherichia coli* O157:H7. They reported sensitivities of 10 cfu/mL in phosphate buffered saline and 100 cfu/mL in ground beef [170]. The same year, Zhu et al described the use of a microcantilever sensor for the detection of *Salmonella typhimurium*, with a concentration of 5×10^3 cfu/mL [171].

DNA molecules

Fritz and colleagues reported the use of cantilevers for the detection of nucleic acid. The cantilevers were coated with gold, and thiolated oligonucleotides were immobilized on this side of cantilevers. After the hybridization of the complementary oligonucleotide, the bending of the cantilevers was related to the change in surface stress [114]. In 2003, Su et al. used oligonucleotide conjugated with gold nanoparticle. The microcantilever resonators were able to detect DNA concentrations as low as 0.05 nM [172]. In 2008, Mertens and colleagues reported the study of a self-assembled monolayer of single stranded DNA on a sensing platform consisting in a static operated silicon microcantilever. The surface stress established on one side of the beam structure was investigated upon hydration of the oligonucleotides layer, demonstrating a sensitivity in the fM range [52].

1.3. Chemical surface functionalization for silicon-based biosensing

The successful realization of biosensing devices relies on the immobilization of biomolecules capable of specific interactions with the analyte of interest. Therefore, the proper surface functionalization of silicon-based sensing devices has a critical role, in order to provide high sensitivity and specificity. The immobilization of bioreceptors can be performed through different procedures: direct adsorption, covalent attachment, binding through electrostatic and affinity interactions. A chemical modification of the device surface is often required for the proper attachment of biorecognition elements. Physisorption of bioreceptors on silicon substrates has been widely investigated [173, 174], with drawbacks such as disordered orientation, lack of reproducibility, time-consuming procedures and receptor desorption phenomena. Thus, the stable immobilization represented by covalent attachment is desirable. Ideally, surface chemical functionalization should provide a biocompatible substrate for biorecognition elements tethering, high surface density, stability, reproducibility and minimal samples consumption.

1.3.1. Silane Self-assembled monolayer

Chemical surface modification with organosilanes represents one of the most used functionalization applied to silicon-based devices. The alkoxysilanes molecules are covalently attached to the silicon substrate through the condensation between the siloxanes of the organosilane and the hydroxyl groups exposed on the surface (Fig. 1.15). Silane self-assembled monolayer are more stable from a physical and chemical point of view than thiol-based assembled monolayers, although the formation of an ordered layer of organosilane molecules on silicon surface is a difficult task to achieve [175]. In fact, several important paramenters must be considered: water content, solvent employed, temperature and time of the deposition process are critical aspects for the achievement of high stability and reproducibility [176]. The most used organosilane molecules are thrichlorosilanes, trimethoxysilanes and triethoxysilanes [177]. Before the deposition process, silicon surfaces are dipped into oxidant solution in order to remove organic contaminants and increase the number of hydroxyl groups, which are fundamental in the silanization procedure [178]. Oxygen plasma [179, 180] and piranha solution [181, 182] are the most representative oxidant solutions. The deposition

of organosilane on silicon surface can be performed using different techniques such as wet techniques [183, 184], but organosilane condensation performed through CVD technique was reported to provide well-ordered monolayers [185, 186].

1.3.2. -NH_2 terminating organosilane

3-aminopropylthriethoxysilane (APTES) and 3-aminopropyltrimethoxysilane (APTMS) are the most widely used organosilanes in biosensing applications because of their terminal amine group, which can react with aldehyde and carboxylic groups [187, 193]. APTES and APTMS molecules have the possibility to establish hydrogen bond interactions with the SiO_x surface through the terminal amine group, resulting in a disordered layer deposition [194]. Moreover, alkoxysilane molecules can intermolecularly polymerize into a tridimensional structure, which provide an unstable layer with variable thickness [175]. In literature, different works has investigated the optimal conditions for APTES silanization process on silicon [176]: the best results were obtained using 1% APTES with short reaction time. After the silanization precess, the silicon surface exposes amine groups, which can be used for the direct immobilizations of bioreceptors. Thus, the APTES aminated surface demonstrated to be able to attach antibodies by adsorption [195]. Another strategy consists in the used of N-hydroxysuccinimide (NHS) for protein immobilization. For example, NHS-activated antibodies were incubated on an aminated silicon surface, resulting in the covalent attachment of the biomolecules through the formation of an amide bond [196]. However, the successful immobilization of NHS proteins is heavily dependent on the experimental conditions because of the hydrolysis phenomena in aqueous solutions [197]. A different approach involves the use of homobifunctional linkers such as 1,4-phenylenediisothiocyanate (1,4-PDI) and glutaraldehyde (Fig. 1.15). In the first case, the resulting isocyanate groups represent the binding site for the immobilization of amine-modified oligonucleotides with the formation of a thiourea bond [198]. Instead, by using the glutaraldehyde cross-linker it is possible to expose terminal aldehyde groups on the surface, which can provide the interaction site for amine-containing biomolecules with the formation of imines [199, 200]. Some work report the use of sodium cyanoborhydride for the reduction of the imine double bond [201, 202].

1.3.3. –SH terminating organosilane

The use of organosilane with a terminal thiol group represents an alternative strategy for the immobilization of thiolated receptors. For example, an interferometer system was chemically functionalized through the deposition of mercaptopropyltriethoxysilane (MPTS) and a thiolated oligonucleotide was covalently tethered to the surface by means of a disulfide bond [203]. The same chemistry can be employed for the attachment of aminated bioreceptors through the use of the m-maleimidobenzyoyl-N-hydroxysuccinimide (MBS) cross-linker [204]. Moreover, the treatment of the surface with dithiothreitol (DTT) would allow the regeneration of the silicon device, even though this procedure is rarely implemented.

1.3.4. Epoxy organosilane

Epoxide chemical structure is an alternative chemistry for biomolecule tethering. The main advantage of this chemistry is represented by its stability in aqueous environment and by the possibility of coupling biomolecules containing thiol- or amine- moieties [205]. For example, 3-glycidoxypropyltrimethoxysilane (GOPTS) was used as for the covalent immobilization of antibodies and oligoneucleotides [206]. In another work, the GOPTS molecules were further derivatized incubating with heterobifunctional poly-ethylene-glycol molecules presenting carboxyl groups, which were then activated by means of EDC/NHS for biotin immobilization [207]. Using a second approach, a heterobifunctional poly-ethylene-glycol with amine groups were derivatized on the silicon surface and the following NHS activated biotin molecules immobilization was performed [208].

1.3.5. –COOH terminating organosilane

The deposition of carboxylic functional groups on silicon surface has been investigated for the bio-conjugation opportunity they provide. In fact, these chemical groups can be used for the conjugation of biomolecules that present amine groups. Few works reported the use of this approach: Duval and colleague functionalized silicon nitride devices with carboxyethylsilanetriol sodium salt and applied an EDC/NHS protocol for proteins bio-conjugation [209]. In another work, the same protein bio-conjugation procedure was

performed after derivatization with N-(trimethoxysilylpropyl)-ethylene-diamine triacetic acid [210]. The EDC/NHS protocol must be applied taking into consideration the experimental conditions in which the carboxyl activation is performed. Such chemistry can be employed using two strategy [211]. The first one consists in the activation of carboxyl groups directly on the silicon surface in acidic conditions, followed by the protein bio-conjugation in neutral conditions. The second strategy consists in the activation of proteins in solutions at neutral pH and then the activated proteins are incubated on the carboxylated silicon surface. The main difficulty with this second approach is represented by the cross polymerization of biomolecules in solution, resulting in the formation of protein aggregates [211].

1.3.6. Isocyanate terminating organosilane

The isocyanate chemistry can be used for biomolecules immobilization due to its reactivity towards amine, with the formation of isourea bond and towards hydroxyl groups, with the formation of urethanes [212]. Isocyanatepropyltriethoxysilane (ICPTS) was reported for protein immobilization on the surface of a silicon photonic crystal [186]. The same silane was used for the attachment of streptavidin molecules onto an ICPTS derivatized surface and then biotin-conjugated oligonucleotides were immobilized exploiting the biotin-streptavidin high affinity [213]. This chemistry consists in a one-step protocol, but a precise control of the experimental conditions must be achieved in order to obtain high reproducibility of the immobilization procedure.

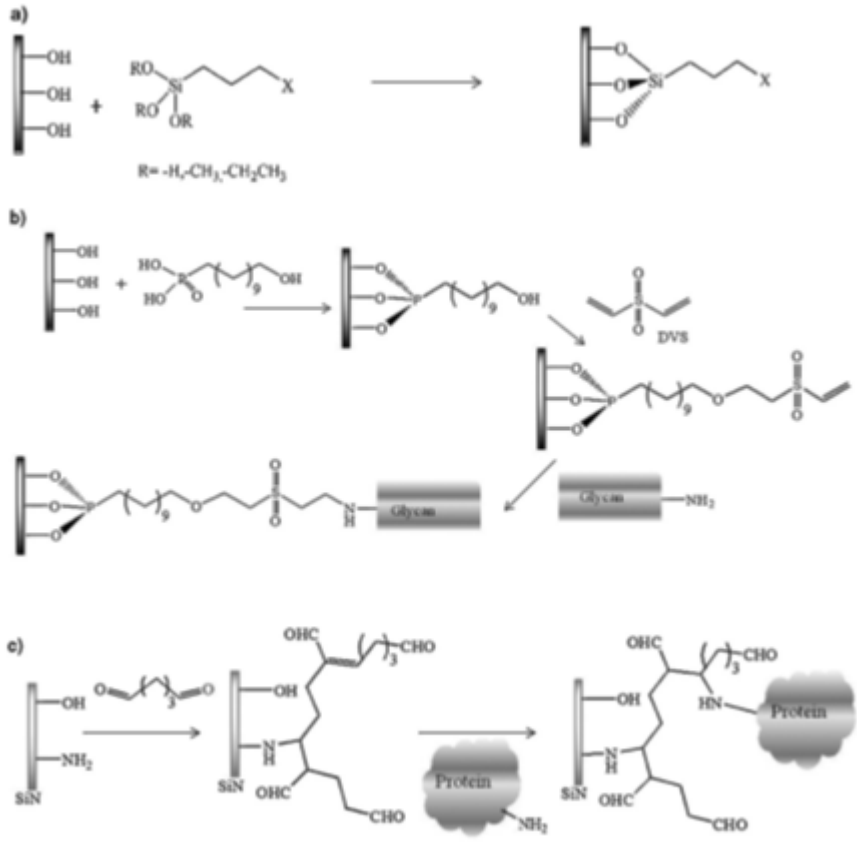

Fig. 1.15. Schematic representation of the most used silicon-based surface chemical modification: organosilane modification (a), phosphonate modification (b), glutaraldehyde modification (c) (from Bañuls et al., 2013)

1.3.7. Alternative strategies for biomolecules immobilization

Even though organosilane-based chemical functionalization represents the most applied surface modification for silicon sensing devices, other approaches can be employed in order to immobilize biorecognition elements on the sensor surface. A few works reported a chemical functionalization based on the formation of a SAM of organophosphonate molecules with terminal hydroxyl groups [214, 215] (Fig. 1.15). Chen et al. reported the immobilization of amine-groups containing glycans on a divinyl sulfone modified surface [216]. Silicon nitride surfaces can be chemically modified following a catalytic hydrosilylation procedure. After removal of the native silicon oxide from the surface, a thermal or photochemical activation was performed in order to promote the reaction between the Si-H moieties on the surface and the alkene molecules [217-219]. The reaction resulted in the formation of carboxylic

groups, which were further activated through the EDC/NHS protocol. This is an interesting strategy that can provide a controlled immobilization of biomolecules with short time procedure. Another strategy consists in the immobilization of antibody by using Protein A or Protein G biomolecules. Protein A and Protein G present domains able to bind the Fc portion on mammalian IgG and their affinity varies with the species. In general, IgGs have a higher affinity for Protein G than for Protein A, and Protein G can bind IgG from a wider variety of species [220]. Several works reported the use of these proteins for the immobilization of antibodies in an oriented manner [221, 222]. Typically, after the biorecognition element tethering, a blocking step is performed on the functionalized surface in order to avoid or reduce non-specific interactions of non-target biomolecules on the remaining active sites. Widely used blocking agents are Bovine Serum albumin (BSA), poly-ethylene-glycol (PEG) and ovoalbumin (OVA) just to cite a few [223-226, 184].

1.4. Dengue Virus

The Dengue virus is a *Flavivirus*, belonging to the family of *Flaviviridiae*. It is a single-stranded RNA virus enclosed in a lipopolysaccharide envelope [227] and itis responsible for an endemic disease spreading in the tropical and subtropical regions of the world called dengue fever [228]. Around 100 countries reported Dengue virus infections with an increasing incidence at global scale [229]. Since now, almost the 40% of the population lives in areas affected by the virus, corresponding to 2.5 billion people [230]. The World Health Organization (WHO) estimated more than 50 million infections annually, with 500,000 hospitalizations and a mortality rate of 5% [231, 232]. Thus, Dengue virus is considered one of the most important arthropod-borne diseases.

Dengue virus is transferred to human beings by mosquitos such as *Aedes aegypti*, *Aedes albopictus* and *Aedes polynesiensis*; some of them are spreading around the different geographical areas, becoming the vector for the endemic disease expansion [233]. In recent years, Dengue virus transmission have been reported in different areas of the world such as Southeast Asia, Africa, Americas, Australia and Europe [234] (Fig. 1.16).

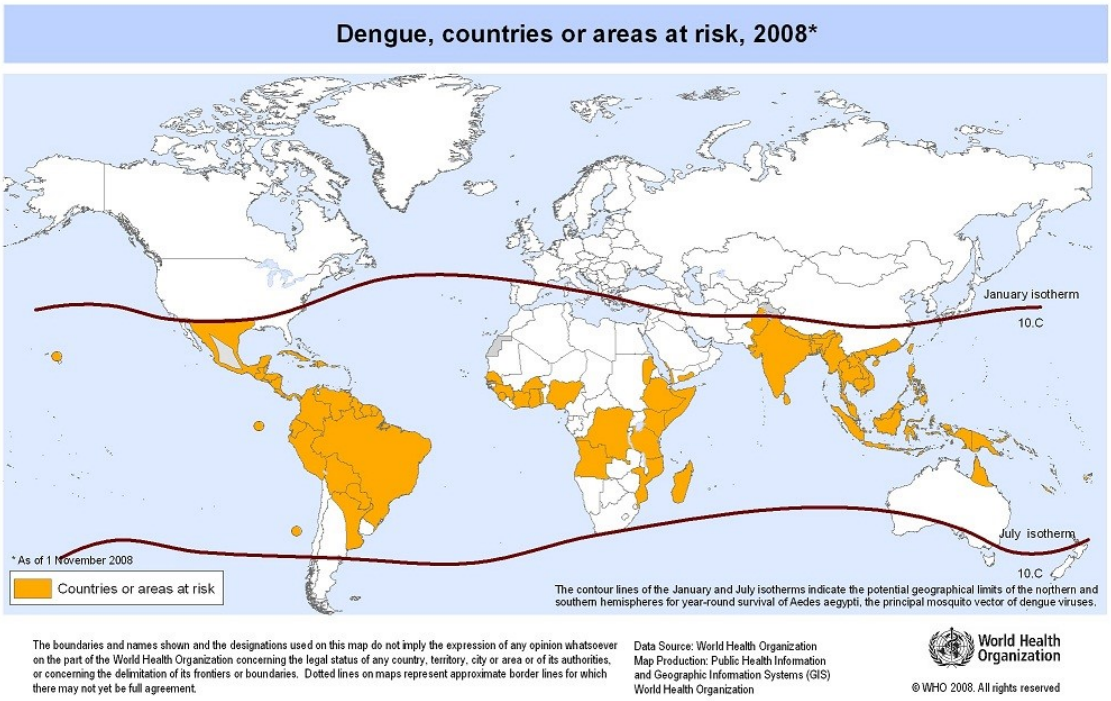

Fig. 1.16. Dengue fever risk map 2008 (from WHO, 2008).

The genomic material of this virus is 10.7 kbp in length and presents a single open reading frame (ORF), encoding for three structural proteins: the nucleocapsid protein C, the membrane protein M, the envelope protein E (Fig. 1.17) and seven more non-structural proteins, including NS1, NS2A, NS2B, NS3, NS4A, NS4B and NS5 [235]. The protein C enclose the genomic material of the virus and the nucleocapsid is enveloped by a lipid bylayer, in which the membrane protein M and the envelope protein E are immersed [236, 237]. The non-structural proteins are involved in the replication mechanism of the virus in the host cell; in particular, they play a role in the virion assembly and in the disruption of host defensive response [238]. Four different serotypes of Dengue virus are known and classified as DENV1, DENV2, DENV3 and DENV4 [239, 240].

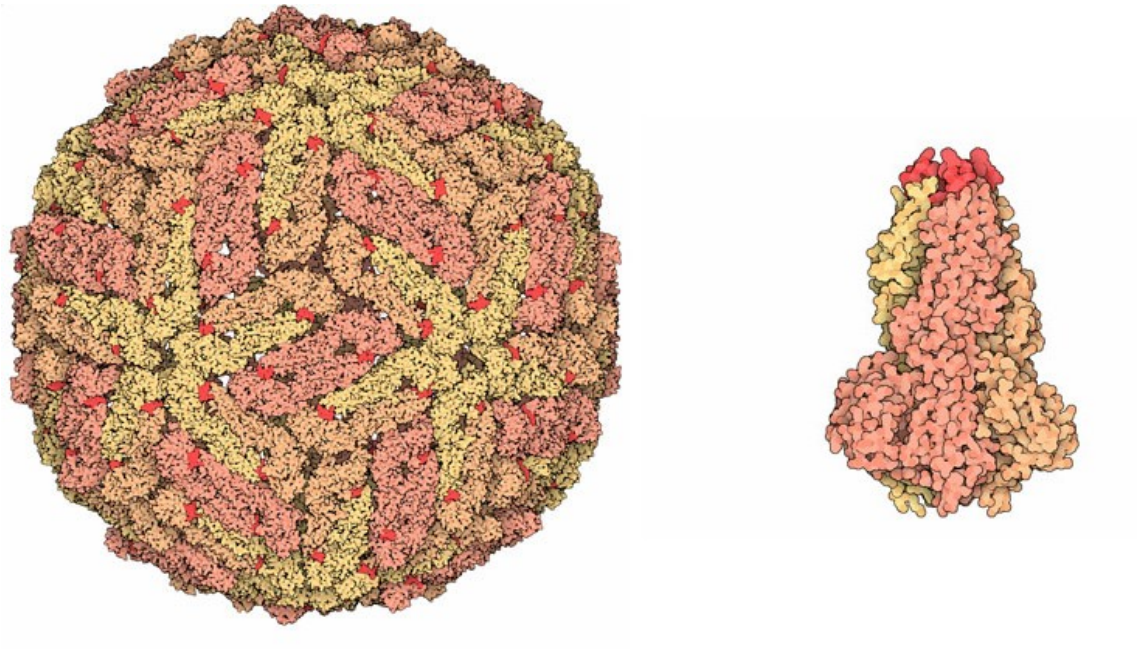

Fig. 1.17. Nucleocapsid of the Dengue virus and the envelope protein E (from Goodsell, 2008).

The infection by one of the serotypes can lead to the different symptoms, from non-apparent infection or mild fever, called Dengue Fever (DF), to severe forms called Dengue Hemorrhagic Fever (DHF) and Dengue Shock Syndrome (DSS), which may lead to death [241, 242]. Immunity against one serotype does not guarantee protection from the infection of other serotypes. Moreover, a secondary infection with a different serotype determines a major risk of onset of DHF and/or DSS [243], due to different immunological mechanisms: the antibody-dependent

enhancement (ADE), the proliferation of the so-called original antigenic sin, which are cross-reacting T cell clones and, finally, the cytokine storm and autoimmune responses [244-249]. Currently, no vaccines of viral treatments are available due to the fact that therapies should be effective against each serotype. The recent spreading of the dengue virus in several geographical areas has led to the increasing demand of reliable point-of-care (POC) devices for on-field detection of the virus, especially in underdeveloped regions of the world. With the advance in bioelectronics technology, new techniques are under development.

1.4.1. Dengue virus clinical diagnostic methods

In a clinical context, the diagnosis of Dengue infection is related to the virion isolation, detection of RNA, capsid antigen detection and serological analysis of specific anti-dengue antibodies [250]. The isolation of the Dengue virus is performed from mosquitoes or patient cells, using cell culture techniques. However, these methods require expensive laboratory instrumentation, educated personnel and time-consuming procedures [251]. Molecular biology techniques have been reported for the diagnostics purposes. For example, reverse transcription-polymerase chain reaction (RT-PCR)-based methods coupled with real-time PCR, such as nested RT-PCR, real-time quantitative PCR and nucleic acid sequence-based amplification have been applied for the detection of dengue virus in patients' samples in acute-phase of infection [252-254]. These techniques can provide sensitive and reproducible analysis with serotype discrimination but are limited by the high technological requirements. Bioassays that use specific antibodies against the NS1 protein have been reported and commercial anti-NS1 protein kits are available for the detection in acute infection samples [235]. However, these methods are not able to discriminate between serotypes. Another strategy consists in the application of serological assays for the detection of the virus. In particular, one of the most used format is represented by an ELISA method for the detection of dengue-specific IgM antibodies in serum, plasma and saliva [255]. Analogously, an IgG antibody-capture ELISA was used for primary or secondary determination of the infection through the evaluation of IgM/IgG ratio, which is related to the mechanism of Dengue virus infection [256]. The determination of serotype by these immune-assays is difficult due to the cross-reactivity among the *Flaviviruses* [239].

1.4.2. Point-of-care diagnostic methods

One of the most successful POC method is a lateral flow immunoassay, in which a specific antibody against the analyte of interest is conjugated with gold nanoparticles [257]. This complex is used to capture the target molecules and reveal the biological specific recognition through a second antibody which is able to interact with a different epitope of the analyte. Such technology was applied for the realization of several commercial kits for the detection of the non-structural NS1 protein and of the specific IgM, IgG and IgA antibodies [255, 258].

1.4.3. Biosensors diagnostic methods

Recently, different biosensing devices with piezoelectric, optical and electrochemical transducing mechanism have been reported for the detection of several targets related to dengue virus. The first one consisted in the use of a QCM on which two specific monoclonal antibodies against the E protein and NS1 protein were immobilized on a piezoelectric transducer for detection in saline buffer. The oriented immobilization of these specific antibodies on the sensing surface was achieved by the previous immobilization of Protein A [259]. This QCM device was able to detect the DENV2 serotype in spiked samples with a sensitivity comparable to the ELISA NS1 immunoassay. Another work reported the use of MIPs as biorecognition elements on a QCM-based sensor[260]. After the immobilization of NS1 protein imprinted polymers on the sensing surface, the device was able to selectively recognize the NS1 protein in clinical samples with a whole detection time of less than one hour. Even though these QCM biosensors have been successfully applied for diagnostic purposes, their detection capability in clinical context may be limited by protein interference in complex matrices such as serum and plasma. Another well established technique for the detection of biological targets is represented by SPR sensing platform. A SPR-based sensor was used for the label-free recognition of IgM antibodies in serum [261]. In particular, the dengue virus antigen was immobilized on the gold-coated sensing surface and the IgM containing serum was put in contact with the device. The detection of the target was monitored in real-time with a single step procedure. A similar diagnostic device was applied for the discrimination of Dengue serotypes: four Dengue virus antigen serotypes were immobilized

and only one µl of serum was required for the revelation of the dengue specific IgM with an overall time detection of ten minutes [262]. Thus, SPR-based sensor allowed the label-free detection of Dengue virus in a sensitive and specific manner. However, the required instrumentation is still rather large, limiting its application to on-field applications. Recently, the application of electrochemical impedance spectroscopy (EIS) was reported for the detection of Dengue virus antigens. EIS is an electrochemical technique, which relies on the change of electron transfer resistance at electrode/solution interface in order to provide information about the adsorption and desorption kinetics of analytes established on the electrode surface. An EIS biosensor was used for the detection of serotype specific IgG antibodies. In particular, particles of DENV2 serotype were immobilized on an alumina membrane presenting nanopores. In this way, it was possible to make quantitative measurements of both the immobilized DENV2 and of the bound IgG antibodies [263]. A similar sensor design was used for the detection of oligonucleotides sequences of the dengue virus on a nanoporous alumina membrane. Synthetic DNA probes were attached to the membrane and complementary dengue target sequences were hybridized to the probes causing an impedance change due to pore blocking. The limit of detection demonstrated to be the 10^{-12} M for a 31 bp sequence [264].

1.5. Aim of the Work

The selective recognition of specific analytes in different matrices is of fundamental importance in several fields and applications. Moreover, these kind of applications strongly need a label-free detection, to reduce costs and complexity of the device. As an example, in the field of diagnostic and/or food monitoring there is a constant demand of biosensors able to detect the presence of biological target molecules (e.g. tumor markers, toxins) which could be found in complex matrices, such as human blood or foodstuffs [168]. Cantilever-based systems are promising label-free sensing platforms for this kind of task because of their high sensitivity [168]. In particular, dynamic mode operated cantilevers are used as a weighting device (microbalance), using the shift in their resonant frequency to detect the mass of the objects tethered to their surface [264], without the need of a signal amplification as it happens in ELISA or in fluorescence methods. In fact, the mass resolution extends from the nano- (10^{-9}) to the zepto- (10^{-21}) gram range, whether vibrational curves are recorded, respectively, in a

complex matrix such as a liquid environment or in vacuum conditions, enhancing mass sensitivity due to the minimization of dumping effects in the latter case [165].

MC-based-biosensors had been successfully applied for the detection of different targets (proteins and small molecules) in physiological buffers, paving their potential application in complex matrixes. In particular, this kind of biosensor was used for the detection of Angiopoietin-1 in Phosphate Buffer Solution (PBS) [222], of mycotoxins in PBS and in a mixture of acetonitrile/PBS [265] and of β-estradiol in serum samples [266].

However, this MC arrays method shows some critical aspects when working with biological samples, which may result in a less accurate performance of the sensing platform. The critical steps were identified in the washing procedure, in the chemical functionalization used for biomolecules immobilization and in the non-specific binding due to the lack of passivation steps. Moreover, the conditions carried out for incubation of biomolecules represent another critical aspect of the whole procedure.

For these reasons, the methodology used to face all these critical aspects of the detection technique is described in the Results and Discussion section. Then, the application of the MC-based arrays to the quantification of immobilized proteins is presented. Thanks to this approach, it was possible to acquire useful information about the preferential orientation assumed by these proteins with respect to the sensing surface. Finally, this method was applied for the study of the interactions of the dengue virus 1 with a specific antibody. Dengue virus is responsible for the Dengue Fever (DF) and Dengue Hemorrhagic Fever (DHF), which are a leading cause of hospitalizations in tropics and subtropics area. Four serotypes of dengue virus are currently known and the infection by one serotype does not confer protection from other serotypes. Moreover, a secondary infection by a different serotype is correlated to a major risk of insurgence of DHF, which may lead to death. Currently, no cure or vaccine are available; thus, a better understanding of the interactions between the viruses and specific antibodies is expected to provide fundamental information for the development of a vaccine.

Chapter 2: Materials and Methods

In this section, the fabrication process of MCs starting from a Silicon-On-Insulator (SOI) wafer is described. In order to define MCs geometry and establishing their characteristic suspended configuration, a combination of bulk micromachining techniques on the back side and Reactive Ion Etching (RIE) on the front side of the silicon wafer have been applied. Next, the different components constituting the experimental measuring set-ups used for the resonant frequency characterization of MC arrays is illustrated. All the components of the system are described: the actuation (through a piezoelectric crystal), the read-out systems (using the optical lever technique), the vacuum chamber in which the MC arrays are mounted and the pumping system which allows to operate MCs arrays in a relatively high vacuum condition (2×10^{-7}).

During the early phase of this work, an optimization of the bioassay procedure was performed by means of an ELISA-like assay. In particular, squared silicon samples (5×5 mm^2) were used as a model surface for the study of a novel chemical functionalization protocol used to immobilize proteins to the silicon surface. Moreover, this model was used for the optimization of the washing steps, for the investigation of the proper incubation conditions during proteins immobilization and for the blocking step necessary to avoid non-specific interactions. The preparation of the samples and the experimental conditions will be described in details.

2.1. MCs fabrication process

MC arrays have been produced starting from a 4 inches Silicon-On-Insulator (SOI) wafer (Ultrasil Corporation). This is a (100)-oriented single crystal, p-type boron doped wafer.

Fig. 2.1. Cross-sectional view of the SOI wafer used for the cantilever fabrication.

In Fig. 2.1, a cross-sectional view of the SOI wafer used for MCs fabrication is reported. This wafer comprises four layers: i) the device layer with dimensions of 7 ± 1 µm, ii) the buried oxide layer of 1.5 ± 0.1 µm, iii) the handle layer (bulk silicon) of 300 ± 5 µm, iv) the silicon oxide layer on the back of the SOI wafer of 1.5 ± 0.1 µm.

For the MCs fabrication a Reactive Ion Etching (RIE) process on the front of the wafer and a bulk micromachining technique on the backside have been implemented. The former allow to define the geometry of the cantilevers, while the latter permits the release of the structure into a suspended configuration. The steps of this two-mask process is reported in Fig. 2.2.

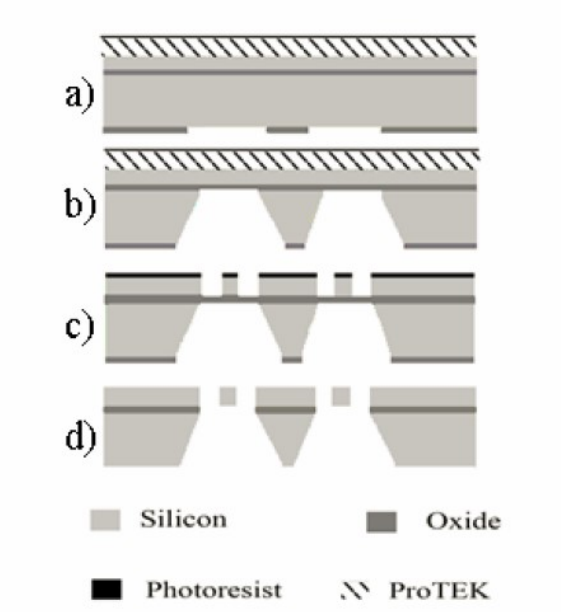

Fig. 2.2. Scheme of the main steps of the cantilever fabrication process: a) optical lithography on the back side, HF etching of the SiO_2, polymeric (ProTEK™) KOH protection on the front side; b) KOH wet etching of the bulk silicon; c) optical lithography on the front side to define the planar geometry and RIE on the silicon device layer; d) HF etching of the buried oxide layer.

2.1.1. Optical lithography and device layer polymeric coating

On the backside of the wafer an optical lithography is performed. This step allows to draw the geometrical area for the following wet etching.

A HPR 504 positive photoresist (Fujifilm) is spinned on the backside (v= 3500 rpm, t= 20 s, d= 1.4 um). Subsequently, the surface is covered with the lithographic mask to define the region in which the bulk silicon attack will be performed and following exposed to UV light using a mercury vapor lamp (wavelength λ=365 nm, power density P=3 mW/cm^2). After exposure, the photoresist is developed using the AZ developer and removed in an acetone bath. Finally, a hydrofluoric acid solution (Buffered Oxide Etch, BOE) is used for the wet etching of the silicon oxide layer present on the back of the exposed regions of the wafer. After the optical lithography procedure, a protective polymeric film is deposited. In particular, the ProTEK™ B2 (Brewer Science) is used as a protective coating of the device layer during the wet etching of the bulk silicon (see section 2.1.2). Before the polymer deposition, a primer (ProTEK Primer™, Brewer Science) is applied to improve the adhesion of the polymer itself to the silicon surface.

This primer is spin coated (v = 1500 rpm, spinning time t=60 s) and a soft bake at a temperature of 130 ÷ 150 °C on a hot plate for 1 minute is performed. The polymeric coating is then deposited by a spinning procedure (v=1000 rpm, t=90 s). Finally, a three step hard bake at T_1=150 °C for t_1=2 min, T_2=170 °C for t_2=2 min and T_3=225 °C for t_3=1 min is performed in order to obtain a compact polymeric film.

2.1.2. KOH wet etching

The KOH wet etching of the bulk silicon is performed using a 20% w/v KOH solution. The geometric dimensions of the regions are calculated in order to obtain a 1080×1080 μm^2 squared silicon oxide/silicon membrane, given that the etching angle of the KOH attack on single crystal (100) silicon is θ=54°74'. During this procedure, the sample is mechanically locked in vertical position using a Teflon® cell (see Fig. 2.3). This positioning guarantees a better evacuation of the hydrogen bubbles produced during the etching process. The operating temperature of the bath is T=85 °C and the use of a magnetic stirrer for mixing improves the uniformity of the removal from the bulk silicon, which is obtained in almost three hours of KOH etching.

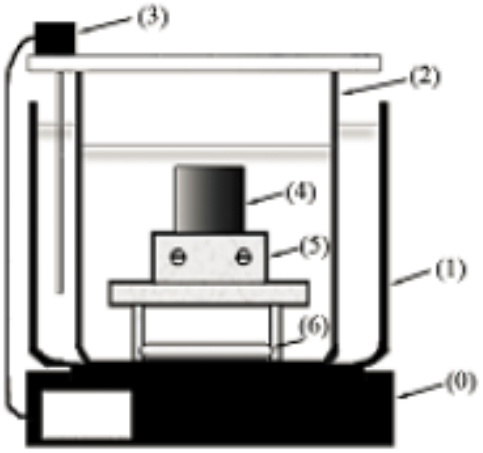

Fig. 2.3. KOH etching set up: (0) hot plate with temperature control; (1) external glass vessel filled up with hot water; (2) internal glass vessel filled with KOH solution; (3) temperature sensor feedback; (4) sample; (5) Teflon sample stage with clamping system for sample immobilization; (6) magnetic stirrer.

2.1.3. Optical lithography and RIE process

When the KOH wet etching of the silicon bulk is complete, the removal of the polymeric film using the ProTEK™ Remover 100 solution (Brewer Science) is performed. In order to obtain a perfectly clean silicon surface, a cleaning procedure in piranha solution (H_2SO_4:H_2O_2, 3:1) is required. Through an optical lithography on the front side using the second mask of the process, the planar cantilever geometries are defined. As previously described, a positive photoresist film is spin coated on the cleaned silicon surface (v=4000 rpm, t=20 s), then exposed to UV light and developed in the proper solution. The cantilever shape is transferred to the device layer through a RIE dry etching, removing the silicon down to the silicon oxide membrane. For this plasma etching, sulphur hexafluoride (SF_6) is used as process gas. Its etching rate is much greater on silicon than on the photoresist pattern imprinted on the front side and it is negligible on the buried silicon oxide layer. A plane parallel plate RIE (STS 320PC) was used; the gas flux into the vacuum chamber is 30 sccm and the operating pressure is 100 mtorr. Finally, the samples are immersed in a BOE solution in order to remove the silicon oxide membrane and the cantilever array is released.

2.1.4. MC array

MC arrays used in this work comprises eleven MCs. They are 460 µm in length, 50 µm in width and 7 µm in thickness. In Fig 2.4 is reported an image of a MC array. The dimension of the handle layer of a whole MC array is about 5×5 mm^2.

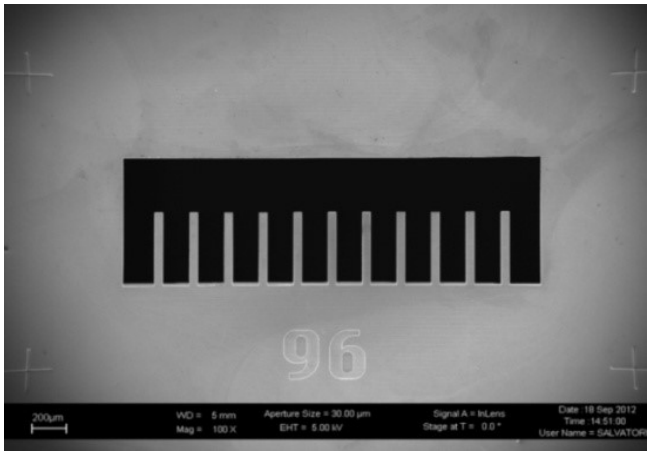

Fig. 2.4. FESEM image of the MCs array.

2.2. Experimental set-up

MCs resonant frequency characterization has been performed in vacuum conditions using the optical lever technique. After each step of molecules deposition, it was possible to relate the resonant frequency shifts with the variation in mass due to the attachment of small molecules (chemical functionalization) and/or biomolecules to MCs surface.

The experimental set-up used to characterize MCs vibration properties has been developed by Microla Optpelectronics S.r.l. This set-up allows to measure different MCs vibrational modes in an automated manner, superimposing a Lorentzian data fitting on the recorded signal.

In this section, the main parts that constitutes our sensing apparatus will be described:

- The actuation system, that is a piezoelectric disk;
- The read-out system, which comprises a light source focused on the cantilever surface, whose reflection is revealed with a Position Sensitive Photodetector (PSD);
- The electronic chain, which collects the signal from the PSD and filters the external noise before sending it to a PC for data storage;
- The vacuum chamber system that is placed over a two-axis motor controller and allows performing the resonant frequency measurements in vacuum conditions.

In Fig. 2.5 is reported a scheme of the different components comprising our resonant frequency characterization system, while in Fig. 2.6 is illustrated the measurement set-up.

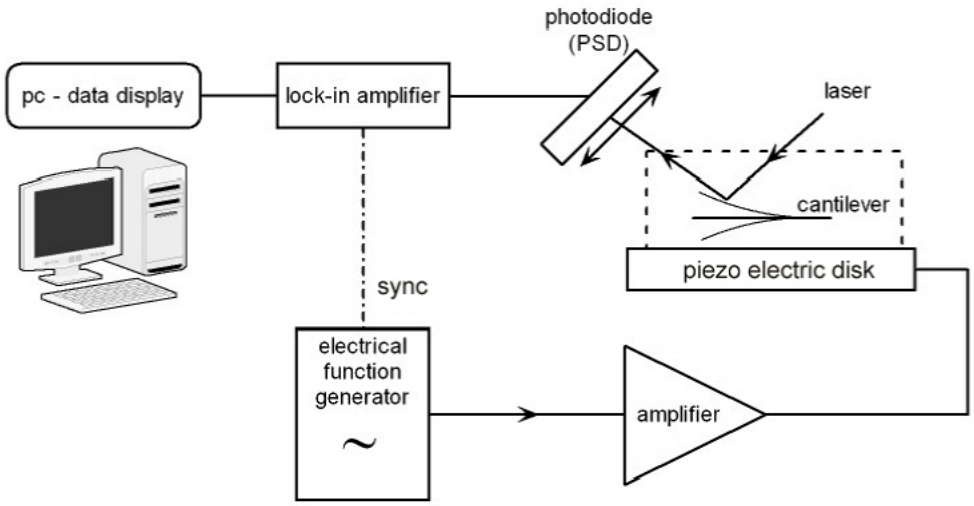

Fig. 2.5. Drawing for the connections of the components which constitutes the set-up for the cantilever characterization

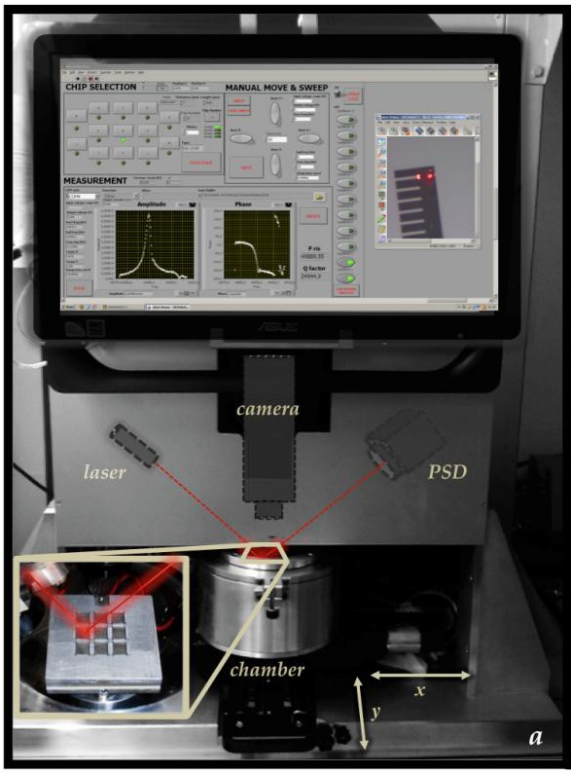

Fig. 2.6. A photograph of the measurement set-up and a close view of the holding cell.

2.2.1. Actuation system

MCs arrays are actuated using a piezoelectric crystal controlled by the function generator of a high frequency lock-in amplifier, which send a sinusoidal signal to the piezoelectric disk. In particular, the piezoelectric disk employed in our experimental set-up is a lead zirconium titanate (PZT) material (PI Ceramics), with dimensions of 300 µm in thickness and 56 mm in diameter, and a nickel/copper metallization on both sides. The bottom side of the disc is attached to a Peltier element by means of a thermal conductive glue. MC arrays are mounted on the piezoelectric crystal using a bi-adhesive conductive tape that allows the proper propagation of the mechanical vibration to the devices. The actuation system is able to put in vibration the MC arrays when excited by a voltage at a certain frequency. Therefore, the MCs vibrate at the same frequency of the excitation input. Moreover, performing a frequency scan to the piezo disk, the MCs can oscillate around their resonance frequency while monitoring their oscillation amplitude.

2.2.2. Read-out system

The sensing of the MCs vibration is performed using the optical lever technique. A laser diode beam (AMS Technologies) is focused on the front side of the cantilever. The procedure is performed using an optical microscope (50x magnification), in order to control the laser positioning on the MCs free end. Once the laser beam is reflected from the surface, an optical lens system collimates the light and focuses it on the small area of the PSD (PSD, Edmund Optics). The incident light is converted in a photocurrent and the amount of charge collected is inversely proportional to the distance between two lateral electrodes and the hitting point of the detector light spot.

The differential response is independent from the intensity of the incident light and from the geometrical properties of the light spot. The photodiode can only detect a dynamic signal, because the differential variation of the charge collected at the electrodes is given by the position variation of the light spot.

2.2.3. Data collection, filtering and storage

The PSD is able to collect the signal related to the movement of the cantilever, but generic low frequency mechanical vibrations of the system and its thermal noise have an influence on the final signal. All these components give origin to a very noisy signal detectable by the photodiode. Therefore, a signal filtering is performed by means of a lock-in amplifier allowing to record only the frequency of the signal which is related to the vibration of the cantilever. A lock-in amplifier works as a narrow band-pass filter centered on an input main frequency, which in our case corresponds to the driving frequency of the piezoelectric disk actuator. The output of the lock-in amplifier (HF2LI Lock-in Amplifier, Zurich Instruments) is proportional to the amplitude of the cantilever amplitude displacement on the z-axis, taking into account only the component related to the driving force of the piezo vibration. The electronics, constituted by the lock-in amplifier and the function generator, is controlled by a Labview® program. This program allows to set up automatic measurements up to nine MC arrays, controlling the range of the frequency scan, the main acquisition parameters and to store data on the PC.

2.2.4. Vacuum chamber system

The vacuum system is constituted by a vacuum chamber evacuated by a series of membrane and turbomolecular pumps (MINI-Task System, Varian Inc. Vacuum Technologies). The chamber is an aluminum hollow cylinder with an internal diameter of 100 mm. At the center of the chamber, there is a cylindrical pivot with a diameter of 30 mm on which a Peltier cell is mounted; the piezoelectric disk is locked over this element. Finally, the chamber is closed on the upper side by a transparent plexiglass stopper, allowing the laser light to pass across it to hit the cantilever surface. A Viton® circular O-ring is used to prevent leakage.

The membrane pump of the vacuum system supplies the primary vacuum, down to a minimum pressure of about 1 mbar, while the turbomolecular pump allows to reach the maximum vacuum value of at least 10^{-7} mbar. Temperature is set by using a Peltier element (SuperCool) and a temperature control feedback (Electron Dynamics Ltd). The feedback signal necessary to maintain a fixed temperature is obtained interfacing the Proportional Integral

Derivative (PID) controller to a thermistor placed in contact with the upper surface of the piezoelectric disk.

2.3. Vibrometer Micro System Analyzer (MSA) 500

The MSA 500 laser vibrometer (Polytec, Waldbronn) uses the principle of the heterodyne interferometer to acquire the characteristics of mechanical vibration or transient motion processes. With this type of interferometer, a high frequency carrier signal is generated on the photo detector with the aid of a Bragg cell. To perform the vibration measurements, the beam of a helium-neon laser is pointed at the vibrating object and scattered back from it. Velocity and displacement amplitude of a vibrating object generate a frequency or phase modulation of the laser light due to the Doppler effect. This modulation is recovered in the signal processing unit by means of suitable decoders (demodulators). The velocity information is recovered from the frequency modulation of the Doppler signal, while the displacement signal can be reconstructed form the phase modulation available at the same time. A schematic layout of both signals is shown as a diagram in Fig. 2.7.

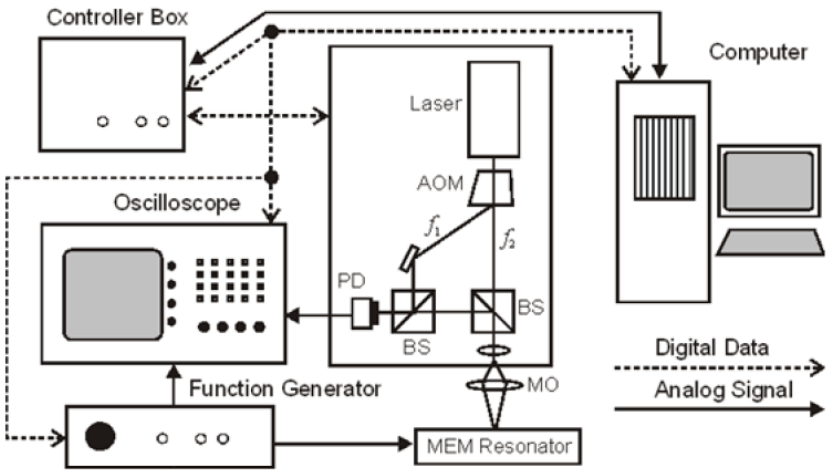

Fig. 2.7. Schematic of the interferometer system: BS is a beam splitter, PD is a photo detector, MO is a microscope objective and AOM is the acousto-optical modulator (Bragg cell).

The Doppler signal is decoded in the controller (OFV-5000) with up to four different signal decoders. The high-frequency Doppler signal coming from the scanning head initially enters into a high-frequency stage, in which velocity or displacement information are recovered from the signal. The decoder stage is followed by a low-frequency stage, consisting of an analog filter module and a digital interphase (S/P-DIF transmitter) as well as a digital filter module.

2.4. Chemical functionalization

The chemical functionalization derivatized on silicon substrate provided the active sites for the ordered immobilization of proteins. In particular, two chemical functionalization based on the deposition of a APTES thin film and further derivatized incubating with succinic anhydride (APTES/SA) or glutaraldehyde (APTES/GA) were used in this work. The reproducibility and reliability of these chemical functionalizations were assessed by means of Optical Contact Angle (OCA), XPS and AFM analysis. Then, an ELISA-like assay was developed in order to test their protein grafting capability. In particular, it consists in performing an ELISA on silicon macro samples with dimensions 5×5 mm^2. Moreover, the protocol used to immobilize biomolecules on silicon devices for biosensing through MC arrays was optimized by means of this technique. Once the proper conditions were chosen, they were applied to MCs bioassay.

2.4.1. Silicon silanization through APTES

Before organosilanes derivatization, silicon samples were immersed in a freshly prepared piranha solution for 15 minutes, to clean and hydroxylate the surface. Then, the samples were rinsed with Milli-Q™ grade water and dried in a stream of N_2. After that, freshly cleaned substrates were incubated with 1% (v/v) solution of APTES in anhydrous toluene at 70 °C for 10 minutes, by using a Schlenk line [267]. Afterwards, APTES derivatized substrates were rinsed three times with toluene and then dried in N_2 stream.

2.4.2. APTES samples modification through GA

In order to obtain a terminal aldehydic group on the silicon surface, APTES samples were incubated at room temperature (RT) in a 0.5% (v/v) GA solution in 100 mM Borate Buffer Saline (pH 8.5) for 1 hour on an orbital shaker. After 15 minutes, sodium cyanoborohydride ($NaBH_3(CN)$) solution (5 M in 1 M NaOH) was added to a final concentration of 50 mM, in order to reduce the imine species formed by the reaction between $-NH_2$ and −CHO groups [267]. After the one-hour incubation, the samples were rinsed several times with Milli-Q™ grade water, dried under N_2 flux and stored in a sealed desiccator until needed.

2.4.3. APTES samples modification through SA

In order to introduce a terminal carboxylic group on the silicon surface, two different methods were tested. The first one consisted in the incubation of APTES samples in a 18 mg/mL SA dissolved in DMF solution for 30 minutes at RT [268]. After the reaction, the substrates were deeply rinsed with DMF, cured for 2 minutes in boiling water, washed with ethanol and finally Milli-Q™ grade water. The functionalized samples were dried under a N_2 stream and stored in a sealed desiccator until needed. These substrates are referred hereafter as APTES/SA1. The second one, by modifying Kim et al. [269], consisted in the incubation of APTES samples at RT in a 5 mg/mL SA and 5 % (v/v) TEA dissolved in THF solution for 2 h, unless differently stated. After the reaction, the substrates were rinsed with THF, ethanol and Milli-Q™ grade water. The APTES/SA1 and APTES/SA2 functionalized samples were dried under N_2 stream, and stored in a sealed desiccator until needed. These substrates are referred hereafter as APTES/SA2.

2.4.4. Surface activation of functionalized silicon substrates

In order to activate the functional groups on the APTES/GA and APTES/SA silicon surface, they were initially immersed in 100 mM MES, 150 mM NaCl, pH 4.7 (MES buffer) for 15 minutes. Afterwards, they were incubated for 15 minutes in a freshly prepared EDC/s-NHS solution (4 mM EDC and 10 mM sulfo-NHS) in MES buffer, unless differently stated. The substrates were

washed three times with phosphate buffer saline supplemented with 0.05% v/v tween 20™ (PBS-t).

2.4.5. Protein G/antibody bioassay

Silicon substrates were functionalized and incubated overnight, at 4 °C, with 50 µL of 50 µg/mL of Protein G (PtG) in PBS-t. Bare silicon or Blank samples (No PtG) were also included as negative controls. The day after, the samples were washed thrice with PBS-t, incubated with 1% BSA in PBS to block the available surface and then incubated with a goat anti-mouse IgG conjugated with horseradish peroxidase (Ab-HRP). The substrates were washed three times with PBS-t, colorimetrically developed with TMB liquid substrate and finally the reaction was stopped with 0.5 M H_2SO_4, at a 1:1 TMB:H_2SO_4 ratio. The optical density (OD) of the solution recovered after the reaction with the samples were recorded by means of a 2100-C microplate reader (Ivymen Optic System) at 450 nm and 630 nm. In order to indirectly quantify the amount of immobilized proteins on the surface, an in-liquid titration curve Ab-HRP in PBS-t was prepared and the related OD was measured. The OD recorded for the different samples were normalized and transformed in surface density (molecules/cm^2) by comparison with the in-liquid titration curve. Finally, the signal-to-noise ratio (S/N) was obtained by dividing the mean signal detected for the different functionalized samples by the signal generated by nonspecific binding of the Ab-HRP to the BSA-blocked surface of bare Si.

2.4.6. Contact angle measurements (OCA)

The surface wettability of functionalized samples was investigated by OCA measurements using an OCAH 200 instrument (DataPhysic Instruments GmbH), equipped with a CCD camera and an automatic dosing system for the liquids. MilliQ™ grade water (H_2O) and diiodomethane (CH_2I_2) were used as liquids for the OCA analysis by means of the sessile droplet method in static mode. Drop profiles were fitted through the Young–Laplace method and contact angles between fitted function and baseline were calculated using the SCA20 software. Standard deviation has been calculated for samples using a data set of three droplets for each liquid. Surface free energy of functionalized silicon substrates was determined by using the Owens–Wendt–Kaelble (OWK) method [270].

2.4.7. X-ray photoelectron spectroscopy (XPS)

XPS studies were carried out by a PHI 5000 Versaprobe scanning X-ray photoelectron spectrometer (monochromatic Al K-alpha X-ray source with 1486.6 eV energy, 15 kV voltage and 1 mA anode current) in order to investigate surface chemical composition. A spot size of 100 µm was used to collect the photoelectron signal for both the high resolution (HR) and the survey spectra. Different pass energy values were employed: 187.85 eV for survey spectra and 23.5 eV for HR peaks. All samples were analyzed using a combined electron and Argon ion gun neutralizer system to reduce the charging effect during the measurements. Spectra were analyzed using Casa XPS software. All core-level peak energies were referenced to C1s peak at 284.5 eV and the background contribution in HR scans has been subtracted by means of a Shirley function [271].

2.4.8. Atomic Force Microscopy (AFM)

The topography of the different samples was investigated by means of the INNOVA® AFM from Bruker Corp. The measurements were performed in the Tapping mode by using Silicon probes with a resonance frequency of ≈ 360 kHz, spring constant ≈ 40 N/m and nominal curvature radius of 8 nm. The recorded images were processed by the Gwyddion software using the standard procedures [272]. The plane inclination and piezo nonlinearities were removed by subtracting a second order polynomial, while the low frequency noise was reduced by a median line averaging. Finally, high frequency noise was reduced through a 2D FFT filtering using an elliptical low-pass filter. The surface roughness parameter was calculated by using the "root mean squared" (RMS) $R_{RMS} = \sqrt{\frac{1}{n}\sum_{i=1}^{n} y_i^2}$, where y_i represents the vertical deviation of point i from the mean value on a topographic map of n points.

2.4.9. MCs protein incubation

Protein G/Ab-HPR assay

Functionalized MC arrays were incubated O/N at 4 °C with 50 µL of 50 µg/mL of Protein G dissolved in PBS. Negative controls (blanks) were incubated with 50 µL of PBS. Subsequently, MCs were rinsed thrice with PBS-t and thrice with Milli-Q™ grade water. After performing resonant frequency characterization, MC arrays were incubated 1 hour at 22 °C with 50 µL of BSA 1% dissolved in PBS. Then, the samples were rinsed three times in PBS-t and three times with Milli-Q™ grade water. After acquiring resonant frequencies, MC arrays were incubated 1 hour at 22 °C with 50 µL of an HRP-conjugated anti-mouse Ab dissolved in PBS. After washing the samples as previously described, the acquisition of resonant frequency was performed.

Domain III-Dengue Virus 1/DV32.6 antibody assay

Functionalized MC arrays were incubated O/N at 4 °C with 50 µL of 250 µg/mL of DIII-DV1 dissolved in PBS. Negative controls (blanks) were incubated with 50 µL of PBS. Subsequently, MCs were rinsed thrice with PBS-t and thrice with Milli-Q™ grade water. After performing resonant frequency characterization, MC arrays were incubated 1 hour at 22 °C with 50 µL of 10 mM ethanolamine dissolved in PBS pH 7.5. Then, the samples were rinsed three times in PBS-t and three times with Milli-Q™ grade water. After acquiring resonant frequencies, MC arrays were incubated 1 hour at 22 °C with 50 µL of 50 µg/mL of DV32.6 antibody dissolved in PBS. After washing the samples as previously described, the acquisition of resonant frequency was performed.

DV32.6 antibody/Domain III-Dengue Virus 1 assay

Functionalized MC arrays were incubated O/N at 4 °C with 50 µL of 50 µg/mL of DV32.6 antibody dissolved in PBS. Negative controls (blanks) were incubated with 50 µL of PBS. Subsequently, MCs were rinsed thrice with PBS-t and thrice with Milli-Q™ grade water. After performing resonant frequency characterization, MC arrays were incubated 1 hour at 22 °C

with 50 µL of 10 mM ethanolamine dissolved in PBS. Then, the samples were rinsed three times in PBS-t and three times with Milli-Q™ grade water. After acquiring resonant frequencies, MC arrays were incubated 1 hour at 22 °C with 50 µL of 50 µg/mL of DIII-DV1 dissolved in PBS. After washing the samples as previously described, the acquisition of resonant frequency was performed.

2.4.10. Statistical analysis of data

Using the following equation, it is possible to relate the shift of the eigen frequency value *Δf* to the corresponding mass increment *Δm*:

$$\frac{\Delta f}{f_0} = -\frac{1}{2}\frac{\Delta m}{m_0}$$

where f_0 is the resonant frequency and m_0 is the initial resonator mass. This relationship is valid if the added mass is uniformly distributed on MCs surface and if the beam spring constant *k* remains constant after the sensing event. These assumptions hold for the detection of soft biomolecules because the spring-constant and the surface stress generated would likely have a negligible influence on the vibrational behavior of the MC resonators [168, 273].

For each MC the first and the second flexural mode of vibration are measured, reported as f_i^n, where i = 1,2 indicates the modal number (the first and the second mode respectively), while n = 1-11 indicates the MC position in each array. The combination of these two measurements allow to increase the number of statistical data. In order to compare measurements from the different vibrational modes, the relative frequency shift are calculated and defined as:

$$\delta_i^n = \frac{\Delta f_i^n}{\Delta f_i^n}$$

These two relative shifts related to the two vibrational modes are combined to obtain the arithmetical mean and the half deviation, which are used as signal of the single cantilever and relative uncertainty, respectively:

$$\delta_{1,2}^{n} = \frac{\delta_1^n + \delta_2^n}{2}$$

$$\sigma_{\delta_{1,2}^n} = \frac{|\delta_1^n - \delta_2^n|}{2}$$

The last step consists in the statistical combination of the eleven MCs comprising an array, in order to obtain a single value with its relative uncertainty. Considering each MC of an array as a single "sensor" able to measure a variable with its uncertainty, it is possible to use the weighted mean to calculate a better estimation of the real value of the array (and its relative uncertainty) as:

$$\bar{\delta}_{1,2} = \frac{\sum \delta_{1,2}^n \, w_{1,2}^n}{\sum w_{1,2}^n}$$

$$\sigma_{\bar{\delta}_{1,2}} = \frac{1}{\sqrt{\sum w_{1,2}^n}}$$

where, $w_{1,2}^n = \frac{1}{\sigma^2_{\delta_{1,2}^n}}$ is the statistical weight, the function which allow to attribute a weight to the single data in the calculation of the mean.

2.4.11. Theoretical estimation of grafted biomolecule densities

Marvin Sketch software (6.1.7, 2014, ChemAxon http://www.chemaxon.com) was used to estimate the theoretical geometrical descriptors of the molecules by means of the geometry tool, as reported elsewhere [274]. The starting structure for the calculation of the BSA parameters was the PDB 4F5S, while for PtG, the protein model structure was elaborated by homology modelling by the I-Tasser server [275, 276]. A manual evaluation of the projection areas was performed for comparison purposes. Two atoms lying on the same plane of the biomolecule PDB were selected using the Viewing Controls-Side View tool of UCSF Chimera (1.10.1, build 40427) [277]. The Distances tool was then used to draw and calculate the distance between these selected atoms. After that, the surface was made visible and an image was exported. With the aim of calculating the theoretical projection area of the biomolecule, this image was analyzed with ImageJ [278] by setting the scale using the previously drawn distance. The projection areas calculate in this way were used for the estimation of the

theoretical minimal and maximal surface densities of immobilized biomolecules. Finally, these theoretical values were compared to the experimental ones obtained with the characterization of MC arrays.

Chapter 3: Results and Discussion

The results of the experimental work performed involving this microcantilever-based system are exposed in this chapter. The dissertation is illustrated in association with a deep discussion about the proposed method and a critic analysis of the obtained data.

In the first section of this chapter, the improvements related to the MC arrays washing step protocol are described. This part of the work allowed to obtain more reliable data from the use of these beams as transducers of biomolecules interactions. The subsequent sections are dedicated to the presentation and characterization of the newly proposed APTES/SA chemical functionalization followed by the comparison of its protein grafting capability with the one established by the widely used APTES/GA surface modification. In particular, the deposition reproducibility and protein binding capability of these chemical functionalizations were investigated by means of an ELISA-like assay, in which silicon samples were used as model surface for the derivatization and the protein immobilization procedures. In the remaining sections, the introduction of the APTES/SA derivatization to MC arrays and the application of this system to the quantification of proteins tethered to the MCs surface are discussed. The MCs biosensing assays presented in this work were performed, as described before, through the characterization of the first and second flexural modes of vibration of different MC arrays before and after target immobilization. All the characterization procedures were performed in vacuum condition. Finally, the same MCs system was applied for the detection of the Domain III of the envelope glycoprotein (Protein E) of the Dengue Virus 1 through the DV32.6 antibody immune-specific recognition, providing some interesting information about the stoichiometry ratio of the interaction between these biomolecules. The evaluation of the binding ability of different antibodies to the virus represents an important achievement because such information may accelerate the development of a vaccine, which is currently not available.

3.1. Washing Procedure

The washing procedure represents a critical aspect for the realization of an efficient biosensor. In the case of MC-based systems used as a microbalance, this aspect is of fundamental importance because the sensor is able to give a signal (frequency shift - mass) even in presence of objects that are not the target of interest. For instance, biomolecules are usually dissolved in saline buffers that provide the optimal pH range and ionic strength in order to maintain the correct spatial conformation of the chemical residues constituting the molecule. This is even more important in the case in which antibodies or receptors represent the biorecognition element, because their specific recognition capability relies on the correct folding of the protein. The necessary presence of salts in the incubation buffer may represents an issue: if the salts are not efficiently removed during the washing procedure, they could crystallize and be weighted during the measurements procedure in vacuum.

In Fig. 3.1 is reported the FESEM analysis performed on two MC arrays that were previously functionalized and subsequently put into two different experimental conditions: the first one (Fig. 3.1a – 3.1b) was incubated with biomolecules dissolved in PBS, while the second one (Fig. 3.1c- 3.1d) was incubated only with the buffer solution (i.e. PBS). In the former ones, the MC array incubated with the biomolecules showed no traces of crystallized salts, while in the latter ones it is easy to notice residues at the clamped region of the MC. In fact, the higher resolution image shows the typical crystallized structure due to salt precipitation.

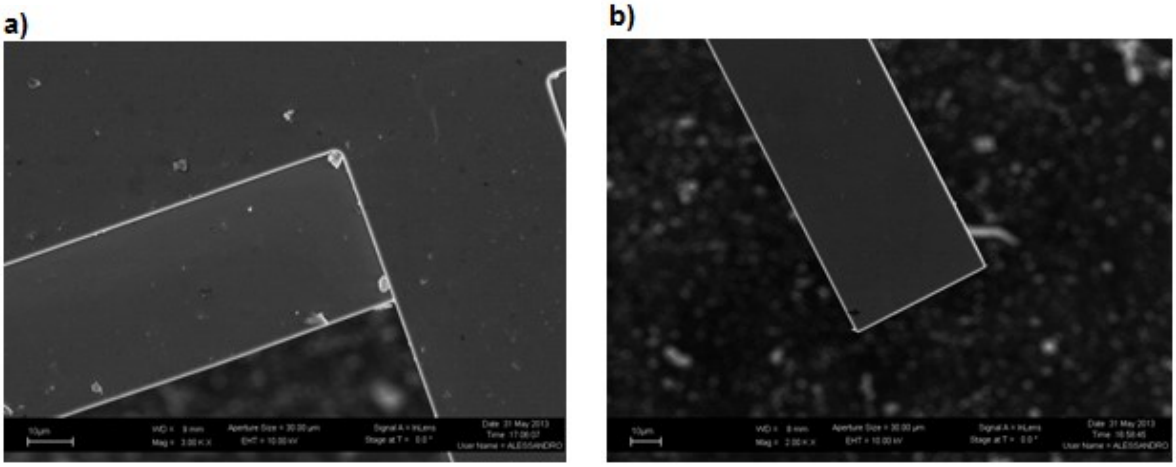

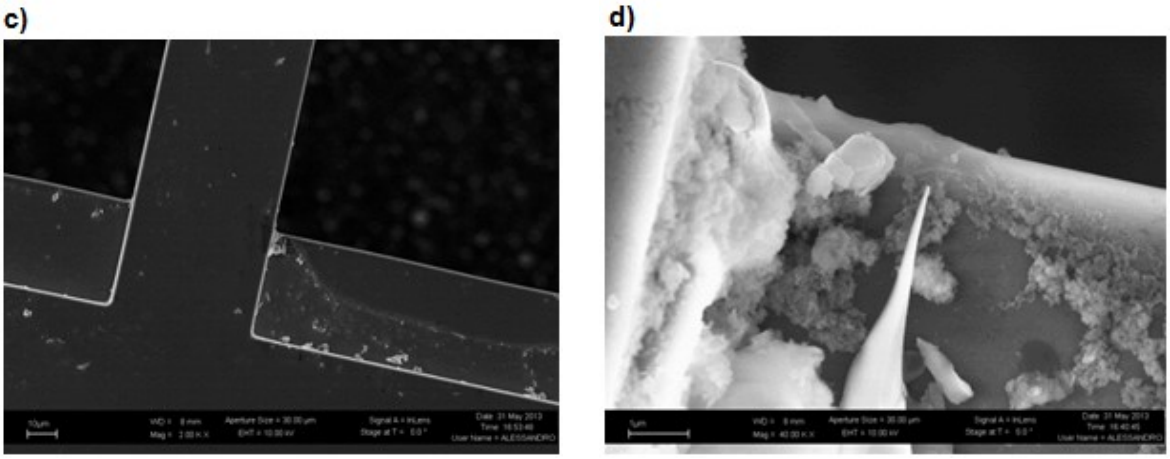

Fig. 3.1. FESEM images of functionalized MC arrays: clamped region of a MC array incubated with biomolecules dissolved in PBS (a-b); MC array incubated in the buffer solution only (c-d).

In order to investigate the most efficient procedure for the washing steps, an experiment in which MC arrays were incubated in PBS only and subsequently washed with different protocols was designed. In particular, two of them were washed pipetting 400 µL of PBS-t thrice followed by pipetting 400 µL of Milli-Q grade water three times. The remaining two MC arrays were washed with the same protocol using a volume of 800 µL of buffer and water.

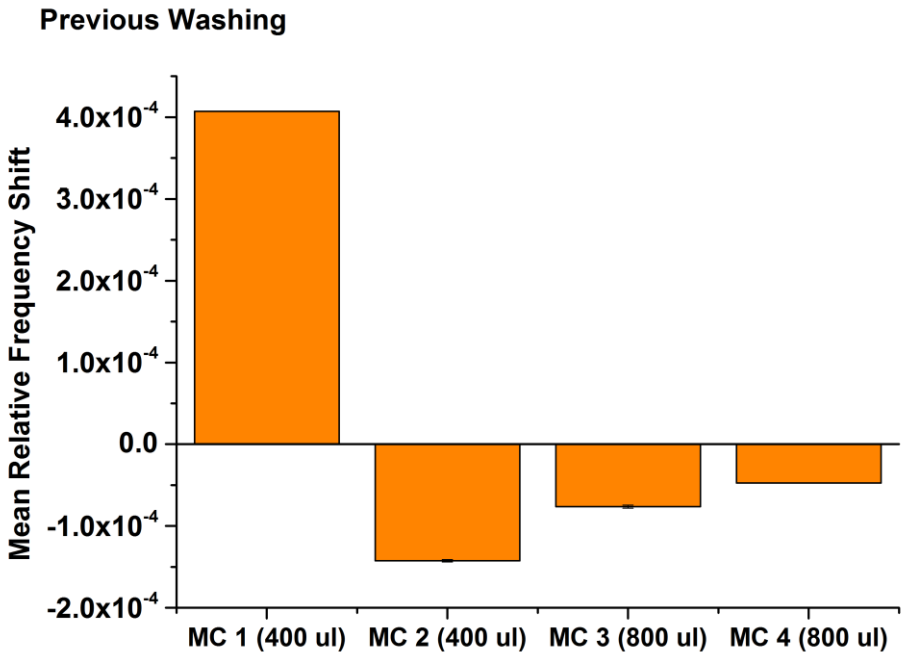

Fig. 3.2. MC arrays evaluation of washing steps procedure: mean relative frequency shifts measured after the incubation in PBS and after performing the two different washing protocols.

In Fig. 3.2, the mean relative frequency shifts recorded after these washing steps are reported. MC arrays washed using the smaller volume of the buffer and Milli-Q water showed the largest frequency shifts. In particular, the MC array 1 experienced a positive shift (i.e. increase of the resonant frequency after the washing procedure); this behavior is probably related to the fact that salts residues, precipitated at the MC clamped region (see Fig. 3.1d), induced an increase of the beam spring constant *k*, which consequently caused an increase of the cantilever resonant frequency. Otherwise, MC arrays washed using a volume of 800 µL showed the smallest frequency shifts in comparison with the MC arrays washed using a volume of 800 µL.

These data suggested that using a bigger volume during the washing steps could improve the removal of salts. Another aspect to be considered is represented by the contact time of buffer and water to the device. The pipetting procedure mainly relies on the mechanical friction to remove the excess of biomolecules that would be loosely attached to the surface. This approach may be not appropriate to dissolve precipitated salts residues.

In order to better understand this aspect, the same experiment was performed using a volume of 1 mL for PBS-t and Milli-Q water, washing the samples three times for 5 minutes on an orbital shaker. Moreover, a gentle pipetting was applied between buffer and water removal.

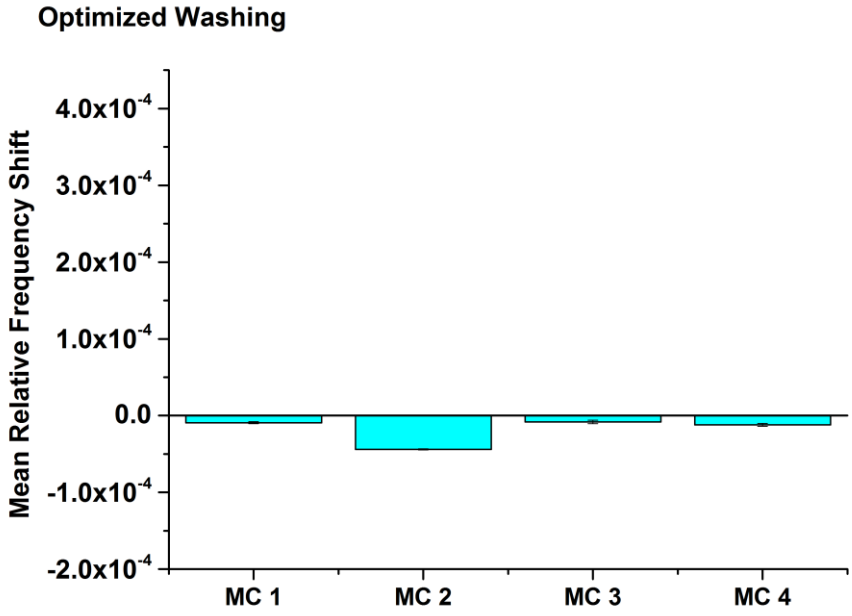

Fig 3.3. MC arrays evaluation of washing steps procedure: mean relative frequency shifts measured after the incubation in PBS and after performing the washing protocol consisting in the use of an orbital shaker and in the increase of buffer and water contact time.

In Fig. 3.3, the mean relative frequency shifts acquired after performing the new washing procedure are reported. As it is possible to notice, the frequency shifts of all the MC arrays are much smaller in comparison with the signals obtained in the previous experiment, particularly when compared to the 400 µL experimental condition. Moreover, the amplitude of the response is very close to the instrumental error of the system used for MCs resonant frequency measurements ($\Delta f/f_0 = 6.0 \times 10^{-6}$). These data showed that an increase in the contact time is required to dissolve completely the precipitated salts residues that would form after the incubation processes.

3.2. Chemical Functionalization

A well-ordered functionalized surface is a critical aspect for the realization of sensitive and specific biosensing devices. One of the most applied strategy to obtain homogeneous and reproducible amino terminated Self Assembled Monolayer (SAM) on silicon based substrates is to work under anhydrous conditions. The procedure followed in this work was previously optimized by Frascella and Ricciardi [279]. The physico-chemical characterization of the samples was performed by means of OCA, XPS and AFM analysis and a set of PtG/Ab-HRP bioassays, in order to obtain an improved surface chemical functionalization with respect to both chemical activity and the procedure duration.

3.2.1. Physico-chemical surface characterization

Two sets of silicon samples were taken in consideration: one was simply cleaned and superficially oxidized with a piranha solution, while the second was also pre-treated by thermal oxidation at 1100 °C. This process allows growing a silica layer of hundreds of nm on the silicon surface [280]. The physico-chemical characterization of these piranha-treated and thermal oxidized silicon samples consisted in Optical Contact Angle (OCA) (Table 3.1) and X-ray Photoelectron Spectroscopy (XPS, Fig. 3.4) analysis.

Table 3.1. OCA measurements of differently functionalized silicon samples.

Surface	OCA_{H2O} [°]	OCA_{CH2I2} [°]	SE [mN/m]	Polar [mN/m]	Disperse [mN/m]
Si-H	78.7 ± 3.0	27.2 ± 1.5	45.52	3.42	42.09
Si-OH	3.7 ± 2.1	33.3 ± 2.3	73.09	45.83	27.26
APTES	58.9 ± 0.6	39.1 ± 3.9	47.87	16.63	31.24
GA	66.1 ± 0.2	36.7 ± 3.9	45.30	11.14	34.16
SA1	52.4 ± 1.3	36.5 ± 1.2	51.94	20.74	31.2
SA2	45.4 ± 0.7	35.6 ± 2.4	56.11	25.76	30.35

The OCA characterization indicated a high contact angle for the non-oxidized silicon surface. Particularly, the Si-H samples (HF treated silicon surface) showed a water contact angle of roughly 79 °, and this value decreased to about 4 ° after the piranha solution treatment (Si-OH samples).

The XPS analysis was performed to check the obtained functional groups following each functionalization step. Fig. 3.4 shows the HR Si2p spectra of a piranha treated silicon sample and a thermally oxidized one. The silicon sample treated with piranha solution presented a characteristic peak split due to the occurrence of both Si (68.6 area %) and SiO_2 (31.2 area %) species (Fig. 3.4, red line).

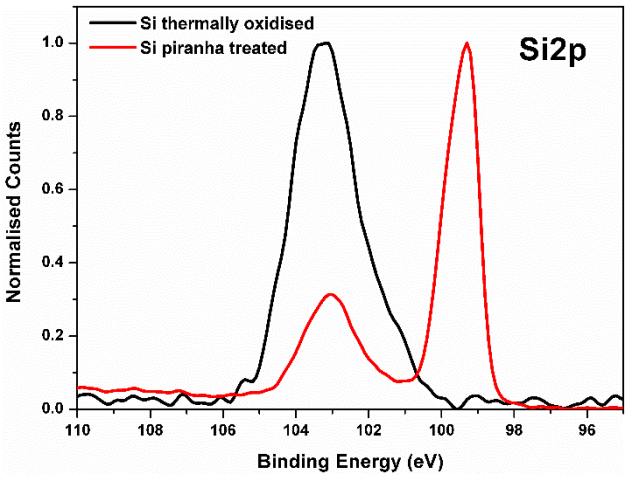

Fig. 3.4. HR XPS Si2p peaks comparison: (red line) Si piranha-treated and (black line) Si thermally oxidized.

The SiO_2 layer thickness, d_x (Å), was calculated using the equation [281]:

$$d_x = \lambda_{Si} \cdot sen\vartheta \cdot \ln\left(\frac{1}{\beta} \cdot \frac{I_{Ox}}{I_{Si}} + 1\right) \quad (1)$$

where λ_{Si} is the attenuation length of the Si2p photoelectrons in SiO_2, θ is the angle between the sample surface plane and the electron analyzer (take off angle, TOA = 45 °), β is the Si2p intensity from infinitely thick SiO_2 and Si, respectively and I_{Ox}/I_{Si} is the ratio of intensities of the oxide film and bulk silicon, respectively. Since there is considerable disagreement in the XPS literature regarding the two sample dependent constants, λ_{Si} and β, it was chosen to assign these two values: λ_{Si} = 2.7 nm and β = 0.83, as used by other authors [282, 283]. With the application of these parameters the oxide thickness was determined as d_x = 8.5 Å as reported in literature [284]. Instead, the Si2p peak of the thermally oxidized sample (Fig. 3.4, black line) is solely due to oxide forms: SiO (12.4 area %) and SiO_2 (87.6 area %). The Si signal coming from the bulk is absent, which means that the entire oxide film (SiO + SiO_2) is thicker than 10 nm at least, which is the typical XPS penetration depth.

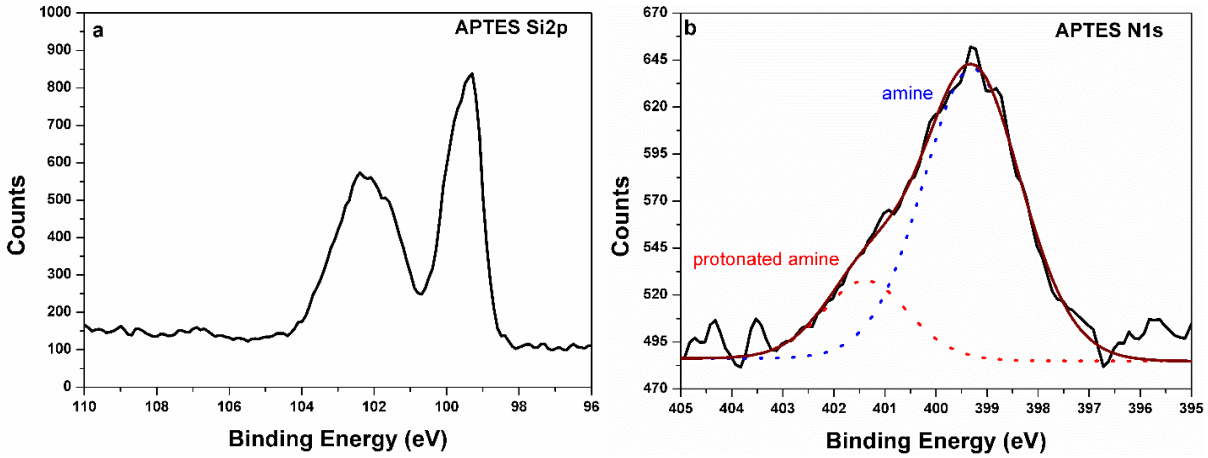

Fig. 3.5. HR XPS Si2p peak (a) and N1s (b) of the APTES functionalized samples: Colored dot lines are fitting curves (Voigt functions), the brown line is the fitting curve envelope while the black line is the experimental curve.

The piranha treated and thermally oxidized silicon samples were then functionalized with APTES, as described in section 2.4. The physico-chemical characterization of these APTES functionalized silicon substrates comprised OCA (Table 3.1), XPS (Fig. 3.5) and Atomic Force Microscopy (Table 3.2) analysis.

The APTES functionalization showed a water contact angle of ≈ 60 °, indicating a moderately polar surface. These properties may be due to the upward oriented amino group and the underlying propyl chain. After the APTES functionalization procedure, an increase of the water contact angle was recorded when compared with the value obtained for the Si-OH samples. Thus, the introduction of the aliphatic component of the molecule prevails on the polar component of the amino group. Moreover, the CH_2I_2 characterization showed a lower value when compared with the one measured from the Si-OH samples.

An XPS analysis was performed on an APTES functionalized Si sample taking into account the Si2p peak and the N1s peak. The former (Fig. 3.5a) still possesses the splitting due to the Si bulk component (51.1 area %) and the oxide one (48.9 area %), which increases, if compared to the previous piranha treated sample. This effect can be explained by the presence of the Si atom in the APTES molecule. The latter one (Fig. 3.5b) is a clear evidence of the primary amine of the APTES molecule. It is composed by the superposition of a higher peak at lower binding energy (399.2 eV, 79.3 area %) and a lower peak at higher chemical shift (401.0 eV, 26.7 area

%). The first component is due to the NH_2 amine signal, while the second one is due to the protonated amine (NH_3^+) signal. The presence of the latter one can be well explained by the interaction through hydrogen bond between the amine of APTES and the unreacted silanol groups of the Si substrates [285].

The AFM topographic maps of APTES functionalized samples were recorded both for piranha treated Si and for thermally oxidized Si. The surface of the sample was quite homogeneous in both cases. The only difference was for the R_{RMS} parameter that was slightly higher for the thermally oxidized samples (0.205 nm) than for the piranha treated one (0.114 nm), as reported in Table 3.2.

Table 3.2. Roughness parameters of the topographical AFM measurements of Si-functionalized samples: $\boldsymbol{R_{RMS}}$ calculated as reported in Section 2.4.8.

Surface	R_{RMS} [nm]
APTES (thermally oxidized)	0.205
APTES (piranha treated)	0.114
APTES/SA	0.202
APTES/SA + PtG	0.305
APTES/GA	1.080
APTES/GA + PtG	1.033

3.2.2. Carboxylic derivatization of APTES samples with SA

In order to improve the reproducibility of immobilized biorecognition elements, the finely tuned APTES protocol was used as a chemical derivatizable layer to introduce at the surface carboxylic groups through the reaction of terminal amine groups with SA. Two procedures (APTES/SA1 and APTES/SA2; see Section 2.4) were chosen: the former corresponds to the

fastest protocol reported in literature [268], while the latter may guarantee a controlled immobilization of proteins [269].

3.2.3. Physico-chemical surface characterization of APTES/SA

The two succinic anhydride tested procedures were characterized through OCA and XPS analysis. In Table 3.1 the OCA values measured for SA1 and SA2 derivatized silicon samples are reported. The water contact angles of APTES/SA1 and APTES/SA2 were 52.4 ± 1.3 ° and 45.4 ± 0.7 °, respectively. In both cases, the hydrophilicity and the polar contribution of the surface energy increased, with a more emphasized result obtained for the SA2 procedure.

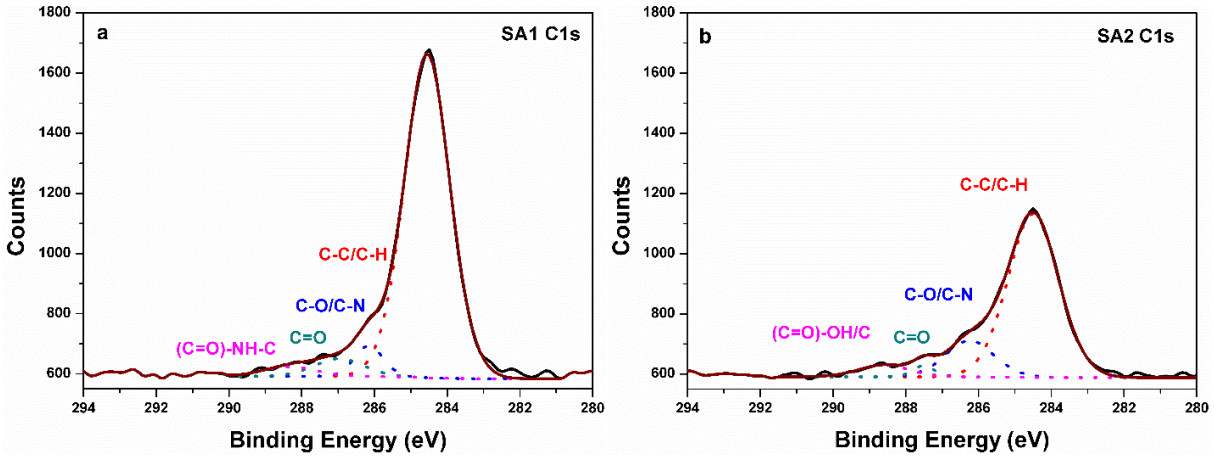

Fig. 3.6. HR XPS C1s peaks for the SA1 (a) and SA2 (b) functionalized samples: Colored dot lines are fitting curves (Voigt functions), the brown line is the fitting curve envelope while the black line is the experimental curve.

In Fig. 3.6, the XPS characterization of the APTES/SA1 and APTES/SA2 samples are reported. The N1s signals from both functionalized samples is less intense, if compared to the one observed for the APTES samples, because of the presence of a longer chain generated by the attachment of the open SA molecule, which lessens the NH_2 signal. It was still possible to distinguish between the amine/amide component at lower binding energy (399.0-400.0 eV) and the protonated amine at higher chemical shifts (405.5-401.2 eV), but the fitting procedure is difficult due to the low S/N ratio (data not reported). For both samples, it was detected the main C-C/C-H peak at 284.5 eV, a second peak due to C-O/C-N at 285.8 eV and the C═O at

287.0 eV. Furthermore, a peak at 288.3 eV was observed in the APTES/SA1 sample and assigned to the amide (C═O)-NH-C resulting from the chemical reaction between $–NH_2$ and the carboxylic moieties of APTES and SA, respectively [286]. For the APTES/SA2 samples a peak corresponding to the terminal carboxylic group ((C═O)-OH/C) was observed at 288.7 eV and it was reasonably superposed to the peak related to the amidic component (not visible). This difference between SA1 and SA2 spectra evidences that only by SA2 method it is possible to limit the reaction between the open SA cycle with the surface amines, to one of the two carboxylic terminations. On the contrary, SA1 method seems to promote "bridge" reactions of both the ends of the molecules with the aminated surface so, feasibly, giving rise to vertical or lateral SA polymerization. This hypothesis is supported by the intensity and amount of SA1 C-C component, at 284.5 eV, higher than the one from SA2 sample (87.78 and 74.80 area %, respectively). It is feasible that this behavior is due to the higher amount of anhydride used during the SA1 method in comparison to the SA2 one.

3.2.4. Protein G/antibody bioassay

Following the physico-chemical characterization, the APTES/SA samples related to the two methods were tested by means of a PtG/antibody bioassay for their capability to effectively tether the biomolecules onto the surface. Furthermore, through the application of an in liquid titration curve, the surface density of grafted molecules was evaluated.

3.2.5. Protein G/antibody bioassay on APTES/SA samples

In Fig. 3.7, the results of this investigation are reported. In this experiment, two different samples were prepared using the two selected procedures and the activation effect of the carboxylic functionalities was also investigated. As it is possible to notice, the higher surface density of grafted molecules is obtained with the APTES/SA2 ($8.38 \pm 1.99 \times 10^{10}$ molecules/cm^2), while the APTES/SA1 protocol allowed to obtain a surface density of $2.15 \pm 0.87 \times 10^{10}$ molecules/cm^2. This difference is accentuated when the samples are activated through EDC/s-NHS dissolved in MES buffer. The mean surface density value measured on activated APTES/SA2 samples is $3.18 \pm 0.06 \times 10^{11}$ molecules/cm^2 of immobilized HRP-conjugated antibody.

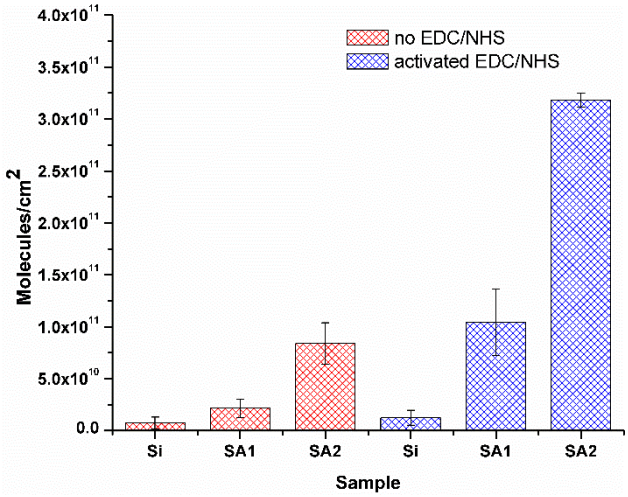

Fig. 3.7. Comparison of the protein binding efficiency of SA1 and SA2 protocols by means of PtG/AbHRP bioassay.

The S/N ratio represent an important parameter for a sensing device and its maximization is desirable in order to have a suitable dynamic range. In Fig. 3.8, the calculated S/N of the differently functionalized samples is illustrated. As highlighted by the graph, the highest S/N ratio is obtained with the activated APTES/SA2 samples.

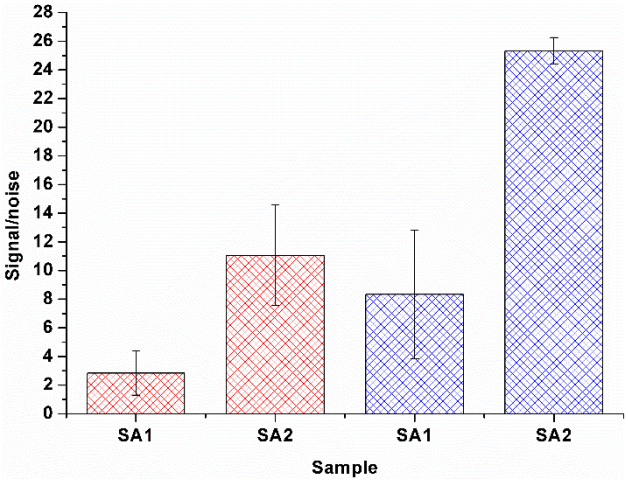

Fig. 3.8. Comparison of the signal to noise ratio obtained during the PtG/AbHRP bioassay performed on APTES/SA1 and APTES/SA2 samples, activated and not activated with EDC/s-NHS.

3.2.5. Optimization of the succinic anhydride functionalization

In order to identify the shortest time required for the chemical derivatization procedure while maintaining a high grade of uniformity and reproducibility of immobilized proteins, the APTES functionalized samples were incubated for different incubation times (0.5, 1, 2, 3 hours) in a SA containing solution. Moreover, the binding capacity efficiency of the APTES/SA2 chemical functionalization was investigated through the proposed PtG/Ab-HRP bioassay. Fig. 3.9a reveals that the mean number of Ab-HRP molecules grafted to the surface is nearly constant starting from 1 hour of contact time, even if the variability of the signal is quite large when compared to longer processes. Thus, an incubation time of at least 2 hours is required with the aim of maintaining a good reproducibility.

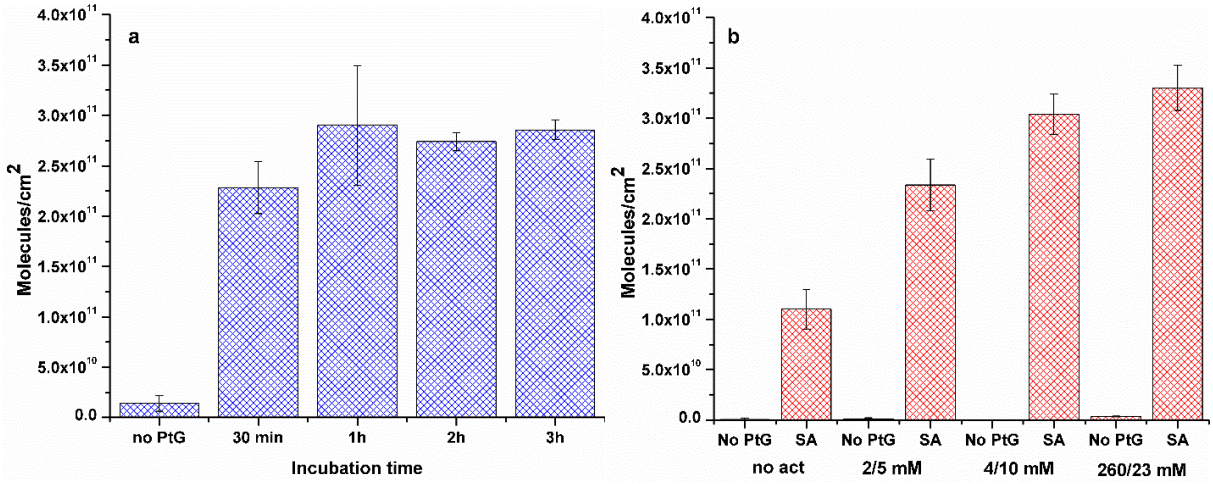

Fig. 3.9. Optimization of the APTES/SA functionalization and activation: a) Influence of different incubation time of the APTES samples in the SA solution on the protein grafting. b) Influence of different carboxyl group activation on the protein grafting (mM concentrations of EDC/s-NHS are reported below the column bars).

The effect of EDC/s-NHS concentrations for the immobilization of PtG/Ab-HRP on APTES/SA2 functionalized samples was studied (see Fig. 3.9b). All the functionalized silicon samples were exposed to the crosslinking agents for 15 minutes: the activation time was chosen as a fixed parameter to avoid the detrimental effects of a longer incubation [196]. The data showed that the mean number of Ab-HRP grafted to a non-activated surface is around 1×10^{11}

molecules/cm^2. The surface density increases to 2.34 ± 0.26 × 10^{11}, 3.04 ± 0.20 × 10^{11} and 3.30 ± 0.23 × 10^{11} molecules/cm^2 if the concentrations of EDC/s-NHS used are 2/5 mM (suggested for bioconjugation applications [196]), 4/10 mM or 260/23 mM, respectively. The highest value of grafted biomolecules was obtained with the highest concentration (260/23 mM), also confirmed by other authors for silicon and silica functionalization [269]. However, the highest calculated S/N ratio corresponds to the 4/10 mM EDC/s-NHS concentration as shown in Fig. 3.10.

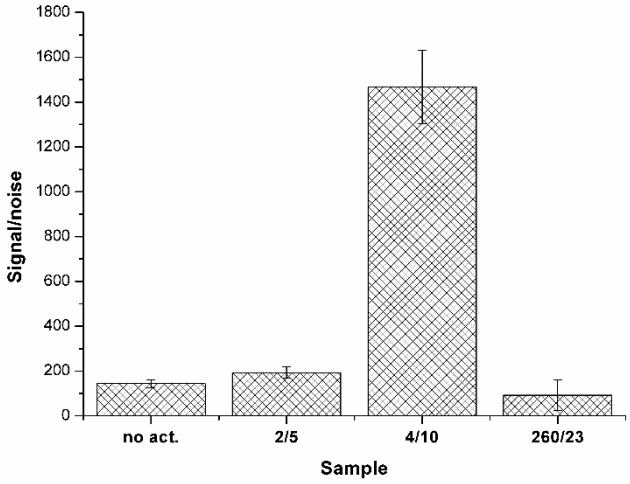

Fig. 3.10. Comparison of the signal to noise ratio obtained during the PtG/AbHRP bioassay performed on APTES/SA2 samples activated with different EDC/s-NHS concentrations.

3.3. Comparison of APTES/SA and APTES/GA functionalization

After selecting the APTES/SA2 chemical functionalization, its protein grafting capability was compared with the one established by another widely used method: the anhydrous APTES-based silanization followed by a glutaraldehyde derivatization for the introduction of an aldehydic functionality (APTES/GA) [279].

3.3.1. Physico-chemical characterization of APTES/GA samples

The physico-chemical characterization of the APTES/GA samples was performed, as before, through OCA, XPS and AFM analysis. In Table 3.1, the values of the OCA measured for the

APTES/GA derivatized surfaces are reported. The GA derivatization showed a water contact angle of 66.1 ± 0.2 °, slightly increasing the hydrophobic component of the surface previously covered by APTES. These results are consistent with the hypothesis presented by other authors [287], suggesting the presence of a high degree of disordered polymerized structures, involving the GA alkyl chains, through the formation of cyclic species containing an aldehydic group.

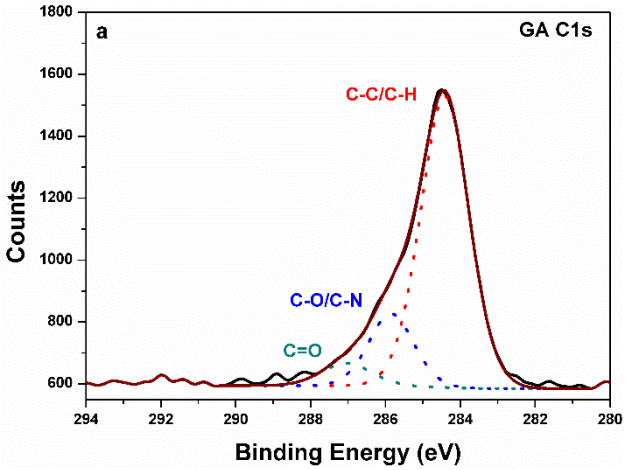

Fig. 3.11. HR XPS C1s peaks for the GA functionalized samples: Colored dot lines are fitting curves (Voigt functions), the brown line is the fitting curve envelope, while the black line is the experimental curve.

In Fig. 3.11, the XPS analysis of APTES/GA samples is reported. It is possible to identify the C-C/C-H peak at 284.5 eV (76.3 area %), the second peak due to C-O/C-N at 285.8 eV (17.6 area %) and the C═O peak at 287.0 eV (6.1 area %). This is due to both the reaction of –CHO in GA molecules with the $–NH_2$ of APTES and the high grade of GA polymerization.

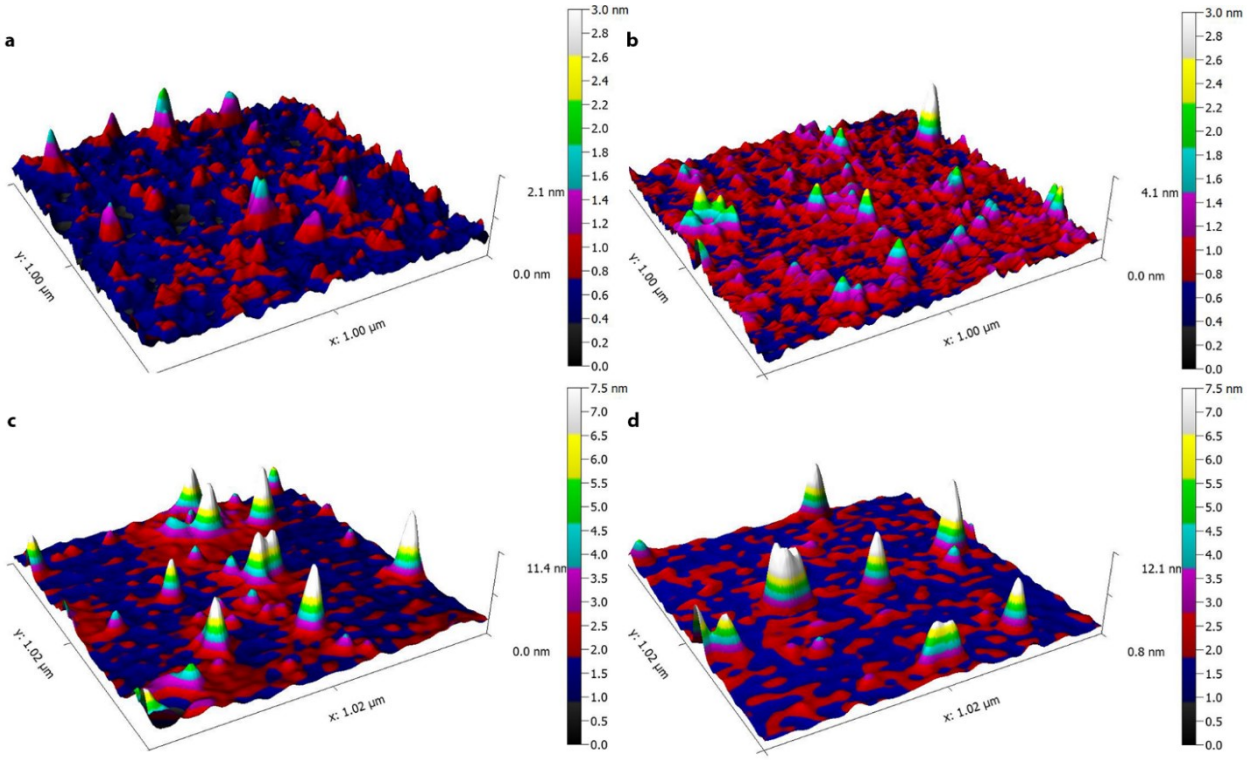

Fig. 3.12. AFM height images of APTES/SA2 (a) and APTES/GA (c) functionalized Si samples: Panels (b) and (d) show the same samples reported on the left but after immobilization of the PtG biomolecule.

Fig. 3.12 shows representative AFM topographic images corresponding to the two different functionalization methods (i.e. APTES/SA2 (a) and APTES/GA (c)). The topographic maps of the same samples after immobilization of the PtG (b and d, respectively) are reported. The surface of the APTES/SA2 sample is quite homogeneous, indicating that the chemical functionalization uniformly covered the sample. This is also confirmed by the rather low value of R_{RMS} = 0.202 nm. After the immobilization of PtG on the surface, the roughness increases to 0.305, but the surface is still homogeneous and only few and very small clusters are formed. Instead, for the APTES/GA sample a considerably irregular morphology was observed with several large clusters and a roughness of R_{RMS} = 1.080 nm, confirming the tendency of GA to polymerize on the surface. The subsequent immobilization of PtG on the surface is hardly noticeable and the roughness remains basically unchanged, slightly decreasing to R_{RMS} = 1.033 nm.

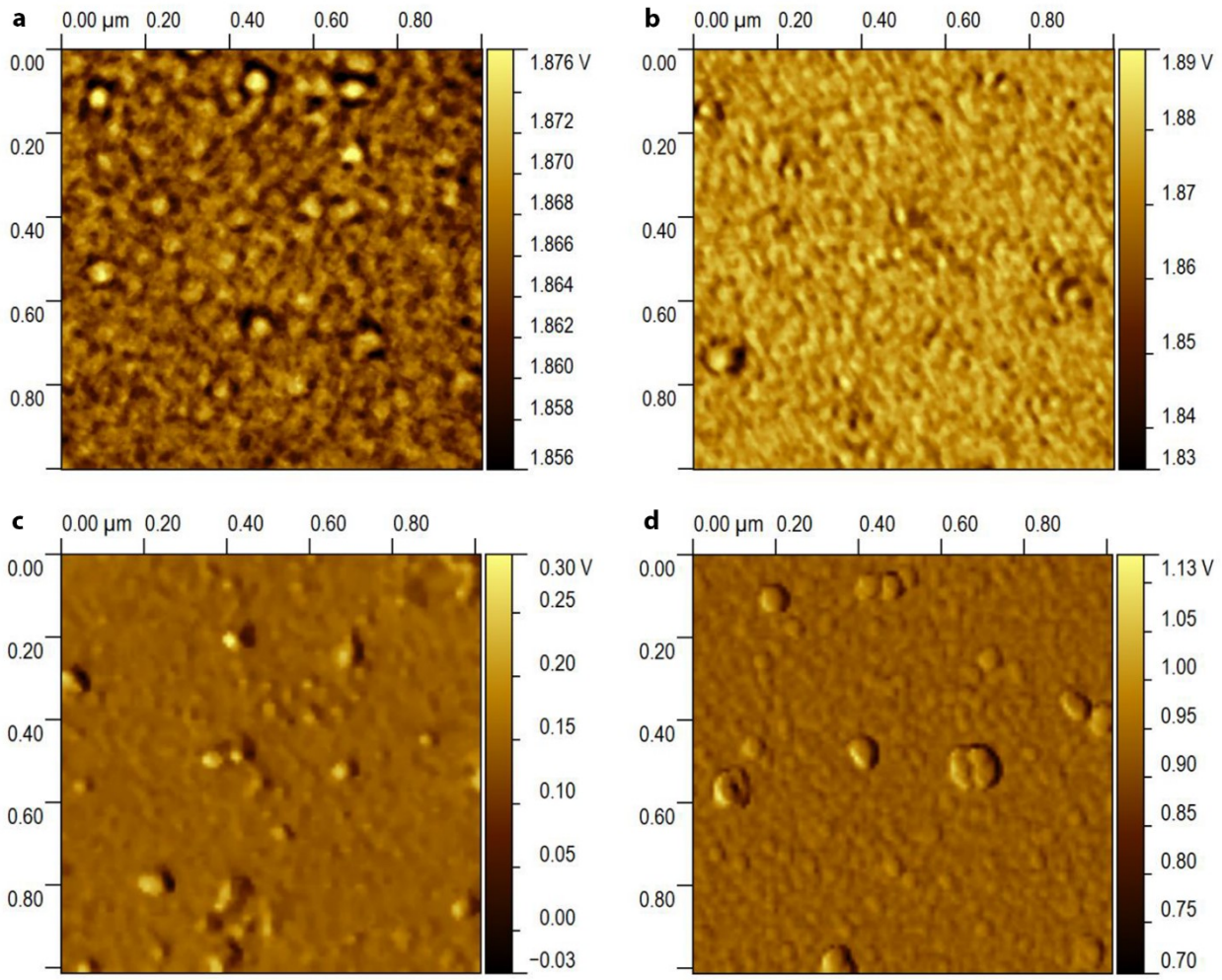

Fig. 3.13. AFM phase maps of APTES/SA2 (a) and APTES/GA (c) functionalized Si samples: Panels (b) and (d) show the same samples reported on the left but after immobilization of the PtG.

The phase maps reported in Fig. 3.13 clearly show that, for the APTES/SA2 samples, new globular structures appear after the incubation with PtG. For the APTES/GA sample, the surface is already inhomogeneous and several globular structures are visible before PtG immobilization. However, the inhomogeneity and the density of globules increase after PtG grafting.

3.3.2. Comparison of the binding capability of APTES/SA2 and APTES/GA through the Protein G/antibody bioassay

The samples were derivatized following the two different methods and compared in terms of surface density of grafted molecules of antibody, after performing the PtG/Ab-HRP bioassay. In Fig. 3.14, the comparison of the APTES/SA2 and APTES/GA functionalizations in terms of active biomolecules immobilization is reported. The highest surface density was obtained for the APTES/SA2 samples activated by EDC/s-NHS with a value of 3.12 ± 0.21 × 10^{11} molecules/cm^2. For the same not activated surface a value as low as 1.14 ± 0.39 × 10^{11} molecules/cm^2 was recorded, highlighting the importance of this activation step. Instead, the APTES/GA functionalization was not influenced by the EDC/s-NHS activation because of the unreactivity of the crosslinking agents with species different from carboxylic groups. The surface densities measured for the activated and non-activated APTES/GA samples were 1.78 ± 0.23 × 10^{11} molecules/cm^2 and 1.54 ± 0.43 × 10^{11} molecules/cm^2, respectively. These data indicate that this surface modification can be used to anchor biomolecules on silicon surface, but with the introduction of a greater variability than APTES/SA2 method.

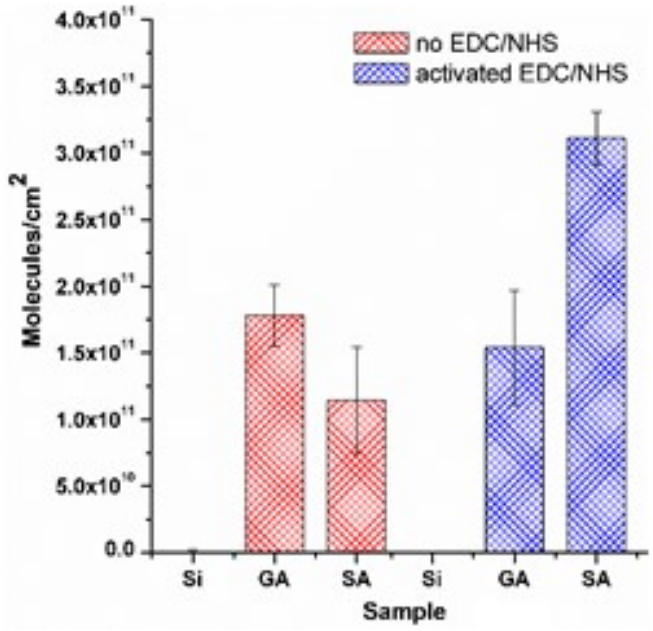

Fig. 3.14. Comparison among the APTES/GA and APTES/SA2 functionalizations in terms of active biomolecules immobilization.

Comparing the surface density of immobilized antibodies, the best performing chemical surface modification is the optimized APTES/SA method combined with the proper EDC/s-NHS activation. Furthermore, the estimated number of molecules of Ab-HRP is related to the effective number of molecules grafted and properly oriented using an orienting protein such as PtG.

Concerning the S/N, this data-set clearly shows that the highest ratio is achieved by the activated APTES/SA2 functionalization, with a mean value of about 1500, which is twice the value obtained by APTES/GA method after the same chemical groups activation protocol (Fig. 3.15).

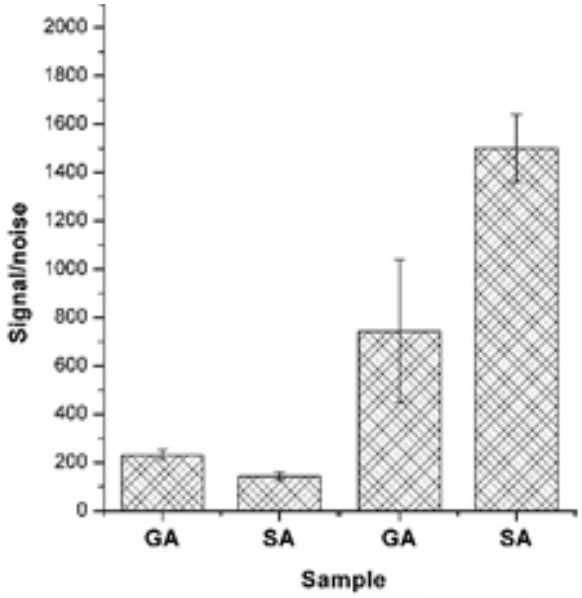

Fig. 3.15. Comparison of the signal to noise ratio obtained during the PtG/AbHRP bioassay performed on APTES/SA2 and APTES/GA samples activated with different EDC/s-NHS concentrations.

The physico-chemical characterizations and the functional PtG/Ab-HRP bioassays demonstrated that the optimized APTES/SA2 protocol generates a surface able to covalently tether biomolecules with high surface density, performing the entire preparation procedure in about 3 hours.

3.4. APTES/SA functionalized MCs for protein immobilization and quantification

The physico-chemical characterizations of APTES/SA functionalization showed that this chemical surface modification is more reliable in terms of homogeneity and reproducibility if compared to the APTES/GA functionalization. Moreover, it demonstrated a better protein grafting capability than APTES/GA when properly activated by EDC/s-NHS protocol. Starting from these results, the APTES/SA functionalization was derivatized onto MC arrays surface, in order to investigate whether it could lead to a more performing biosensing platform when compared to the more consolidated APTES/GA chemical functionalization.

3.4.1. Washing step procedure on APTES/SA functionalized MC arrays

In order to investigate the efficiency of the washing procedure on APTES/SA functionalized MC arrays, the same experiment previously conducted on bare silicon MC arrays was performed (see section 3.1). In particular, three APTES/SA derivatized MC arrays were incubated O/N at 4 °C with PBS.

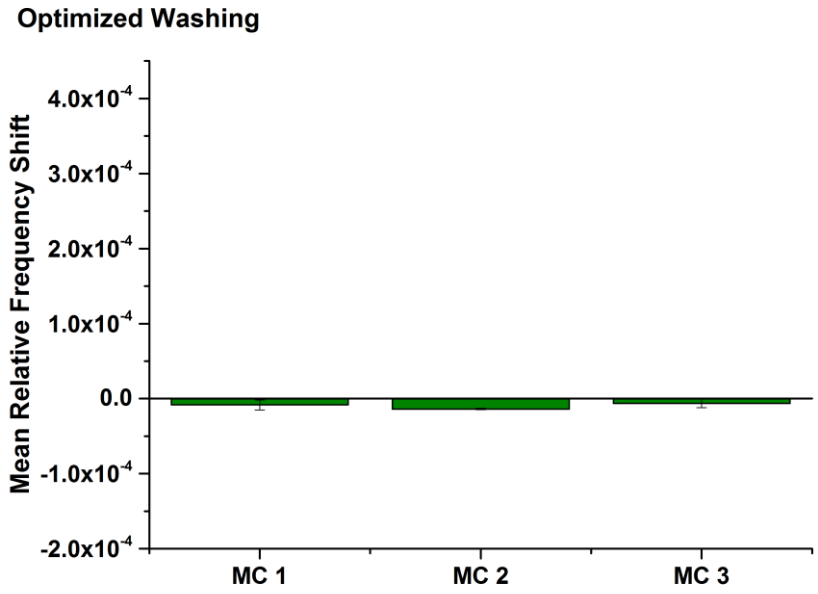

Fig. 3.16. APTES/SA derivatized MC arrays evaluation of washing steps procedure: the box chart show the mean relative frequency shifts measured after the incubation in PBS and after performing the washing protocol.

Fig. 3.16 reports the mean relative frequency shifts measured after the MC arrays were incubated in PBS and washed as previously described in Section 3.1. It is possible to notice that each array underwent very small frequency shifts, comparable to the instrumental error of the measurement set-up. Therefore, these data showed that the optimized washing steps represent an efficient procedure to remove the salts residues that could crystallize during and after the O/N incubation, even on APTES/SA functionalized MC arrays. After the resonant frequency characterization, a FESEM analysis was performed on these MC arrays in order to check the absence of salt residues. The images confirmed the efficiency of the washing steps procedure on APTES/SA derivatized MC arrays (data not shown).

3.4.1. Evaluation of the APTES/GA and APTES/SA molecules deposition on MC arrays

MC arrays were used as a mass sensor for the quantification of APTES/GA and APTES/SA molecules tethered to their surface after the derivatization processes. First, theoretical values were calculated by means of the geometrical descriptors tool of Marvin Sketch (see Section 2.4.8) with the aim of making an estimation of the surface densities in case of a perfect monolayer deposition. These theoretical molecule-covering areas were used (Table 3.3) to make a comparison with the MCs experimental data.

Table 3.3. Comparison of APTES/GA and APTES/SA theoretical molecules/cm^2 and experimental mean molecules/cm^2. *Calculated using Marvin Sketch's Geometrical Descriptors plug-in. **It is assumed that APTES molecules arrange themselves upward.

	Molecular Weight [Da]	Min Molecule Area [Å^2]*	Max Molecules Area [Å^2]*
APTES/GA	234.31	25.34	/**
APTES/SA	234.26	25.34	/**
PtG	21600.00	1359.91	1721.12
BSA	66432.90	2864.03	4088.50

In this experiment, ten MC arrays were silanized with APTES. Afterwards, five of them were subsequently incubated with GA, while the five remaining arrays were incubated with SA. In Fig. 3.17, the mean relative frequency shifts are reported.

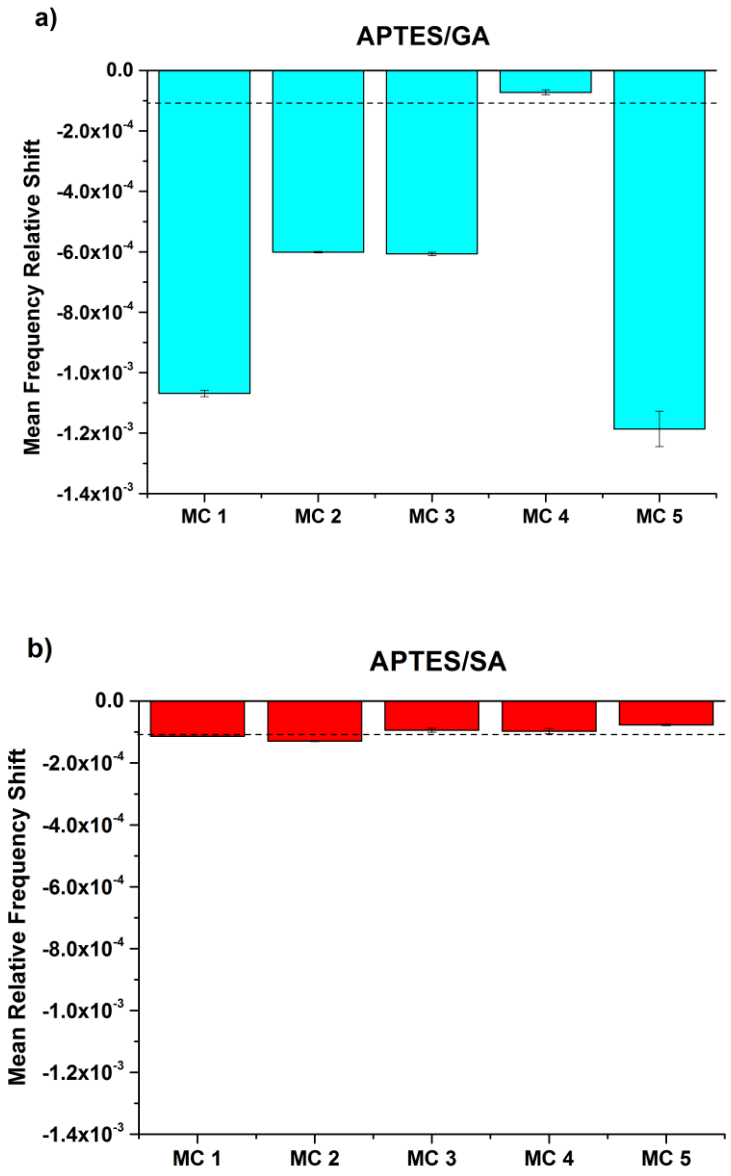

Fig. 3.17. MC arrays evaluation of APTES/GA and APTES/SA molecules deposition: mean relative frequency shifts measured after the functionalization processes of APTES/GA (a) and APTES/SA (b). The dashed line represents the relative frequency shift value expected for a monolayer deposition of molecules. The same y-axis scale was used to facilitate the comparison.

Table 3.4. APTES/GA and APTES/SA theoretical molecules/cm^2 and experimental mean molecules/cm^2.

	Experimental mean Δm [× 10^{-11} g]	Experimental mean molecules/cm^2 [× 10^{14}]	Theoretical molecules/cm^2 [× 10^{14}]
APTES/GA	53.01 ± 33.34	25.81 ± 16.23	3.95
APTES/SA	7.25 ± 1.69	3.53 ± 0.82	3.95

The experimental mean surface density of the five APTES/GA arrays was 25.81 ± 16.23 × 10^{14} molecules/cm^2, while the experimental mean surface density of the five APTES/SA arrays was 3.53 ± 0.82 × 10^{14} molecules/cm^2. The experimental data showed that this measured APTES/SA surface density is very close to the theoretical one, corresponding to a monolayer deposition of molecules 3.95 × 10^{14} molecules/cm^2, while the experimental value for APTES/GA functionalization is about seven times higher than the expected one. In Fig. 3.7, the relative frequency shift expected for a perfect monolayer deposition of molecules is added as a dashed line. Moreover, the measured uncertainty of the APTES/GA functionalization is ≈ 63% of the signal value, while the APTES/SA functionalization present an uncertainty of ≈ 23% of the signal value. These data suggest that the two derivatization processes are quite different in terms of deposition reliability. Thus, APTES/SA can be considered a more reproducible chemical functionalization compared with APTES/GA. Even on MC arrays platform, the lower reproducibility of APTES/GA functionalization is confirmed and can be related to polymerization processes of GA that spontaneously occur in aqueous solutions [287].

3.4.2. Protein G/antibody-HRP bioassay on MC arrays

Thanks to the application of the APTES/SA chemical functionalization, that demonstrated to be a more reliable surface modification for biomolecules immobilization, it was possible to immobilize biomolecules on MC arrays. In particular, MC sensing platform allowed to relate the recorded mass data to the biomolecules surface densities, providing information about the preferential orientation of adsorbed proteins on the resonators surface. In particular, it was possible to formulate interesting considerations about the structure of the protein layers arranged on the solid surface.

The PtG/Ab-HRP, which was conducted on silicon macro samples (section 3.3.2), was then performed on MC arrays. In particular, the resonant frequencies of three MC arrays were acquired after the PtG incubation O/N at 4 °C and after the a-mouse Ab-HRP incubation for 1 hour at RT. These two steps can be considered as the basis for the realization of an immune-sensor because of the Ab orienting ability of PtG.

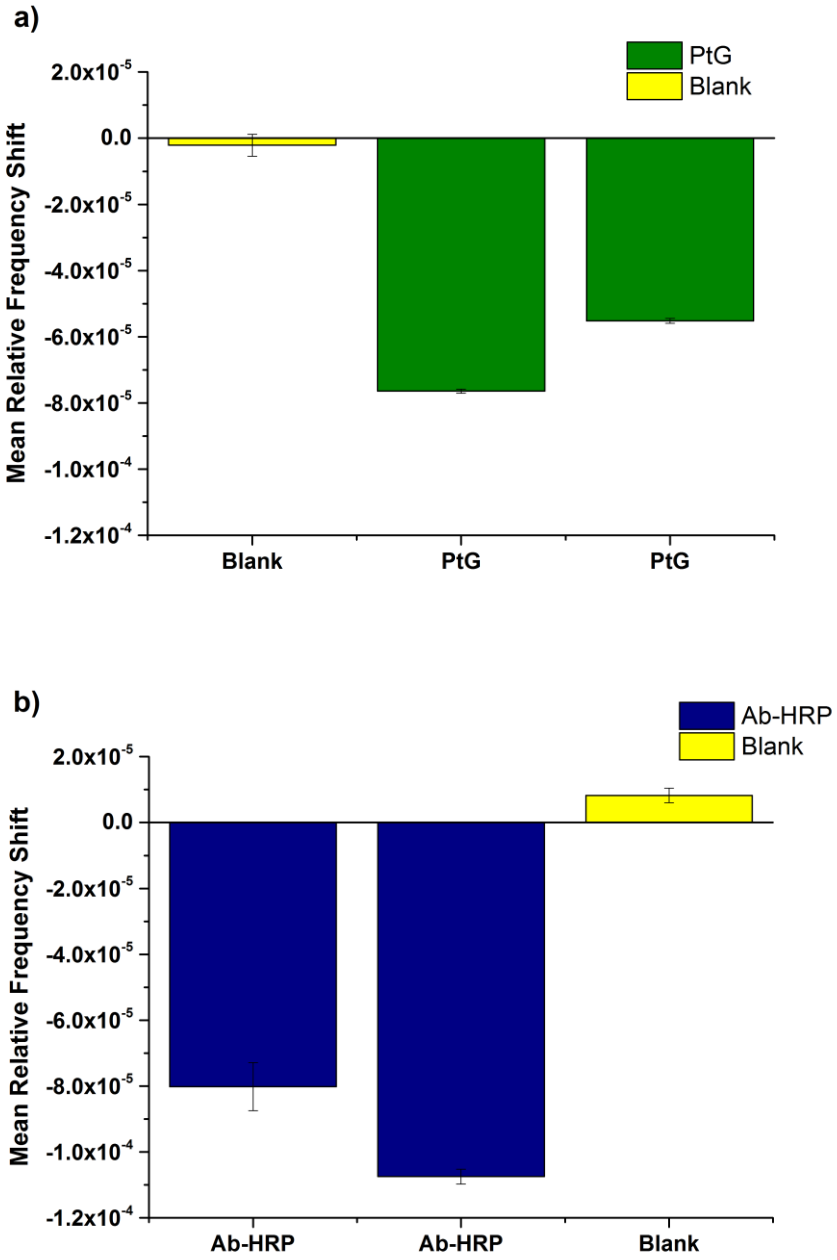

Fig. 3.21. MC arrays evaluation of the PtG and BSA molecules immobilization: mean relative frequency shifts measured after the incubation with PtG (a) and BSA (b).

In Fig. 3.21a, the mean relative frequency shifts after PtG immobilization on MC surface are reported. As it is possible to notice, the two MC arrays incubated with PtG showed a signal that was clearly distinguishable and roughly tenfold higher than the signal recorded for the blank condition. The corresponding frequency shifts are proportional to the added mass of immobilized PtG on MC surface. After the incubation with the Ab-HRP, a clear signal was detectable for the positive conditions (i.e. MC arrays incubated with Ab-HRP), while a very small signal was recorded for the blank condition (i.e. incubated only with the buffer). Analogously, the recorded shifts are related to the mass of Ab-HRP, which established interactions with the orienting PtG previously tethered to MC array. It is important to notice that the first MC array (starting from the left) showed a signal even though it was not previously incubated with PtG and was later incubated with Ab-HRP (Fig. 3.21b, first MC array). The fact that the antibody was able to interact with the MC surface, even when the PtG was not immobilized, suggests that the chemical functionalization still exposes functional groups able to give interactions with biomolecules. This is a common scenario in biosensing applications, in which the non-specific component represents the most important limiting factor for a sensitive device [13].

3.4.3. Quantification of PtG molecules surface density

After showing that APTES/SA could be considered as a more reproducible chemical functionalization in terms of molecules deposition and proteins grafting ability than APTES/GA, a quantification of immobilized PtG was performed using APTES/SA derivatized MC arrays. After the activation step, the MC arrays were incubated with PtG, and their resonant frequencies were acquired. The experimental data were then compared with the theoretical surface densities evaluated with the same bioinformatics approach previously illustrated (see Section 2.4.8). Even though Marvin Sketch geometrical descriptor plug-in was reported to be used for small molecules [274], it is feasible to perform a similar analysis on proteins (i.e. PtG). With the aim of validating the application of this analytical tool to bigger molecules, an evaluation of the proteins projection area was performed by means of a manual method using UCSF Chimera and ImageJ (see Section 2.4.8). The resulting areas from the two methods were

compared: the manual method showed a higher projection area for both protein orientations with a difference that was roughly 5% of the value calculated using Marvin Sketch plug-in. In order to avoid the user-dependent bias of the manual approach, the values obtained by the automatic plug-in were taken into account only (Table 3.3).

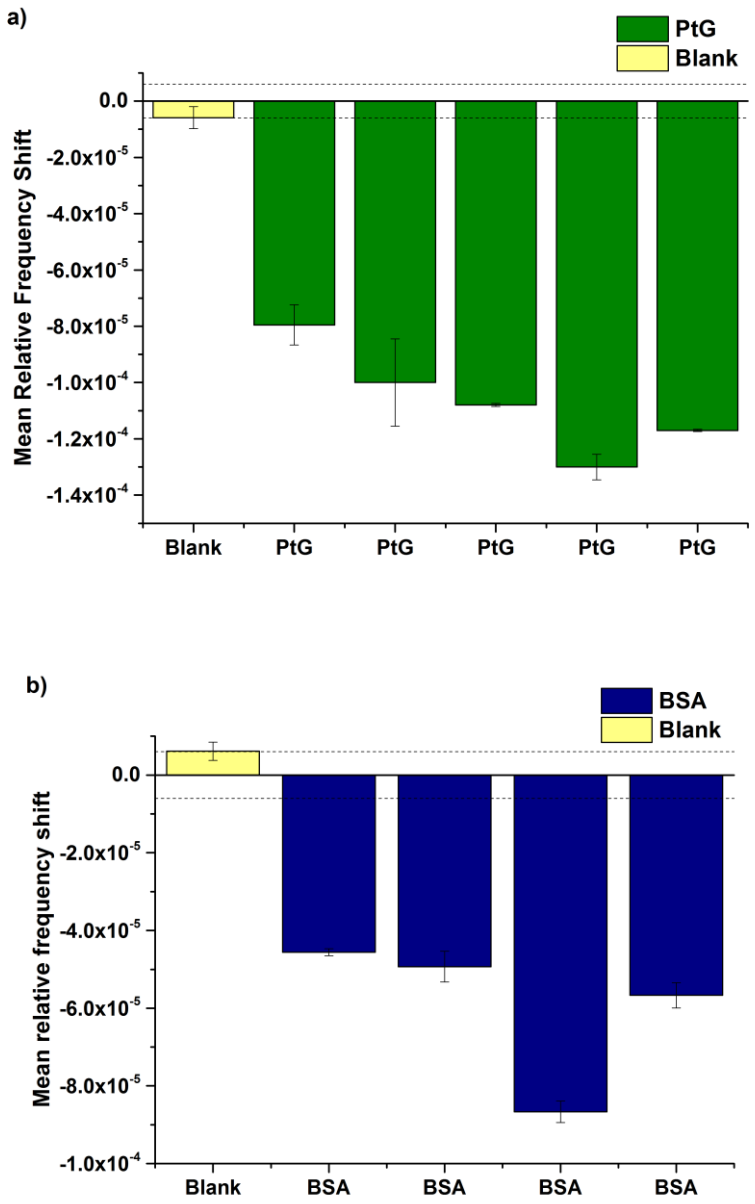

Fig. 3.19. MC arrays quantification of PtG and BSA: mean relative frequency shifts measured after the incubation with PtG (a) and after the subsequent incubation with BSA (b). The yellow columns represent the blank conditions. The dashed line represents the relative frequency shift corresponding to the instrumental error.

Table 3.5. Comparison of the estimated surface densities (minimum and maximum) and the experimentally measured surface density of PtG. PtGeq represents the BSA molecules/cm^2 converted to PtG molecules/cm^2 using BSA/PtG ratio.

	Experimental mean Δm [× 10^{-11} g]		Experimental mean molecules/cm^2 [× 10^{12}]		Theoretical molecules/cm^2 [× 10^{12}]	
	PtG	PtG + PtG_{eq}	PtG	PtG + PtG_{eq}	Min	Max
PtG	8.02 ± 1.42	12.23 ± 2.80	4.23 ± 0.75	5.94 ± 1.36	5.81	7.35

In Fig. 3.19a, the mean relative frequency shifts of the resonators arrays are reported. All five MC arrays incubated with PtG showed a signal that is clearly distinguishable from the blank condition (roughly from ten to twenty times higher) with an experimental mean surface density of 4.23 ± 0.75 × 10^{12} molecules/cm^2. Moreover, the blank signal is comparable with the instrumental error $\Delta f/f \approx 6 \times 10^{-6}$. The precision of the mean value of the analytical replications, such as MC arrays, is limited by the diffusion of the biomolecules in the solution and the possible orientations that proteins can assume with respect to the device surface. As reported by Rabe et al. [288], the orientation of proteins on the surface can be defined by "side-on" or "end-on" orientation. Considering an elliptically shaped particle that is attached with its long or short axis to the surface, a protein is able to expose two different projection areas, leading to different protein surface densities (Table 3.3). The comparison of the theoretical and experimental values for PtG covering densities showed that the experimental mean surface density is slightly lower than the value expected for a monolayer deposition (between 5.81 × 10^{12} and 7.35 × 10^{12} molecules/cm^2), even if it is close to the one corresponding to the theoretical minimum surface density, related to a "side-on" immobilization. However, beyond these considerations, there are other aspects to be taken into account. When a protein containing solution is put in contact with a surface, the protein adlayer structure can be densely or loosely packed depending on the electrostatic features (e.g. pI of the proteins), on the pH and ionic strength of the solution in which proteins are dissolved, and on wettability, roughness and chemical composition of the surface. Therefore, randomized adsorption of proteins on the surface can lead to an inefficiently packed protein

layer leaving undefined gaps between adsorbed proteins, which are not large enough to accommodate other biomolecules [288-290].

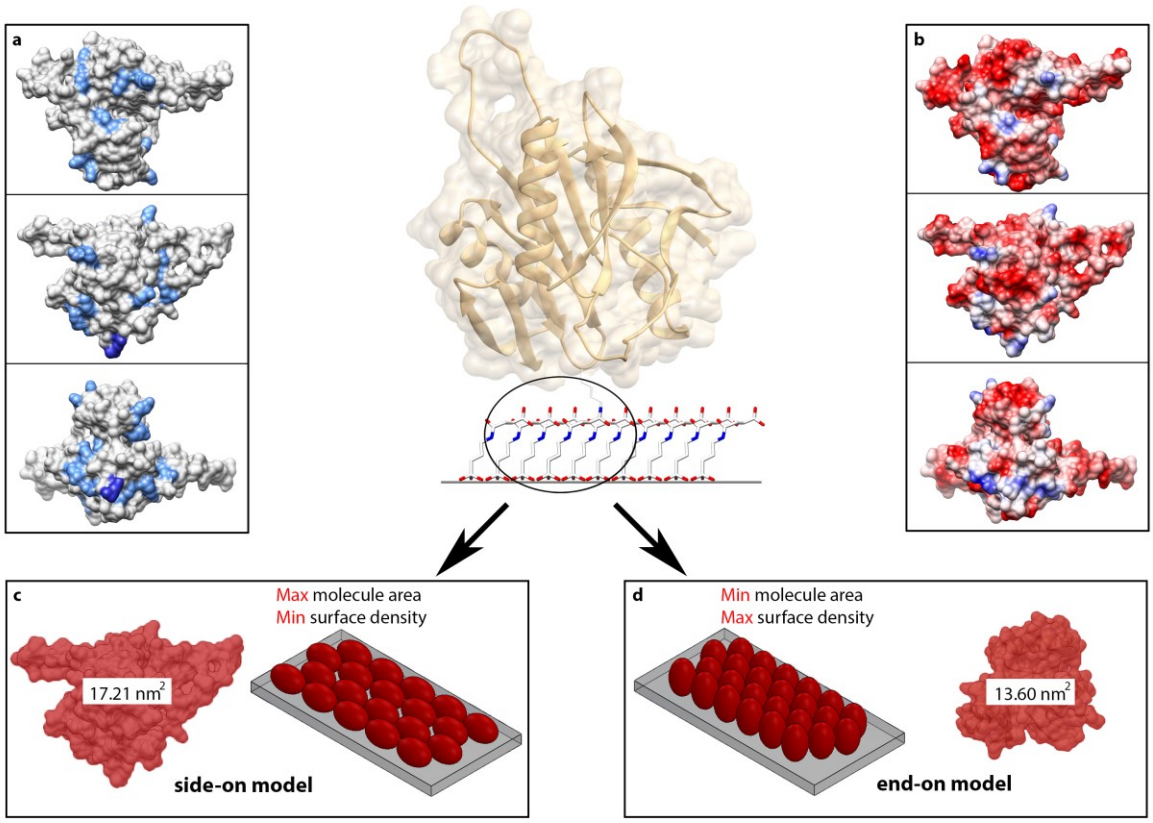

Fig. 3.20. Amine functionalities (a) and the surface amino acids electrostatic potential (b) of Protein G, while in (c) and (d) the Protein G "side-on" and "end-on" orientation models are represented, respectively. On the left, light blue represents Lys residues and blue is the N-terminus. On the right, negatively charged residues are in red and positively charged residues are in blue.

In order to find out the preferential orientation ("side-on" or "end-on") of the PtG on the surface, its surface residues were analyzed according to the primary amine functionalities and to the surface electrostatic potential of the amino acids. Those residues having a primary amine are able to react with activated carboxyl groups present on the APTES/SA functionalized surface; the N-terminus and the Lys residues were taken into account for this analysis. In Fig. 3.20a the Lys residues (light blue) and the N-terminus (blue) are shown, while in Fig. 3.20b the electrostatic potential is represented (negatively charged residues in red and positively

charged residues in blue). As far as the images of the protein model illustrate, the majority of Lys are located in proximity of the N-terminus and a region of highly packed negatively charged residues at the opposite side of the protein. Therefore, it could be more probable that the PtG molecule bind to the chemical functionalization by reacting with one of those residues, through a “side-on” immobilization. Moreover, this hypothesis is corroborated by the asymmetrical distribution of negatively charged residues that would contribute to the formation of a loosely packed “side-on” monolayer, as recorded by our PtG quantification.

Experimental data suggest that, in our case, the achieved PtG immobilization on the MCs surface do not correspond to a monolayer arrangement of proteins and so it is reasonable that small areas of chemical functionalization remain available for the potential interaction of other biomolecules. In fact, the achievement of a perfect monolayer of proteins on a solid surface is a difficult task that quite often remains more an ideal concept, rather than a real experimental condition. In literature, Su et al. reported that a sub-monolayer deposition could be obtained at low concentration of Lysozyme, while the formation of a multi-layered structure was obtained at a higher concentration of enzyme [291]. MC arrays were then incubated with BSA: this incubation step represents a saturation of the available surface for BSA binding, after PtG immobilization on the derivatized silicon surface. Subsequently, the resonant frequencies were characterized again, in order to evaluate the actual immobilization of a protein monolayer. In Fig. 3.19b, the mean relative frequency shifts after BSA incubation are reported. Analogously, each MC array gave a signal proportional to the amount of BSA molecules that were able to interact with the MCs sensing surface and the blank response was again comparable with the instrumental error. A variability in the amplitude of frequency shifts from one MC array to another was recorded. This behavior can be attributed to cross-section and geometry of the available surface for BSA binding, after the PtG deposition. With the aim of better understand this relationship, the PtG and BSA dimensions were related, calculating a BSA/PtG area ratio. Because of the two possible orientation that the BSA and PtG molecules can take on, two ratios were calculated: one considering the maximum projection area of the two proteins (2.38) and one considering the minimum projection area (2.11). The average of these two ratios (2.24) was taken into account due to the impossibility to determine the actual spatial orientation of the two proteins.

In order to estimate the equivalent number of PtG molecules/cm^2 (PtG_{eq}), the experimental values of measured molecules/cm^2 of BSA were multiplied by the average BSA/PtG ratio. This value was added to the PtG molecules/cm^2 obtained in the previous step. The resulting value of total protein coverage was again compared with the theoretical values of PtG surface density reported in Table 3.5.

The experimental mean surface density of PtG + PtG_{eq} ($5.94 \pm 1.36 \times 10^{12}$ molecules/cm^2) resulted to be between the minimum and maximum theoretical surface density. Notably, this value is very close to the expected value for the minimum surface density, indicating that the preferred orientation of the proteins is probably the one exposing the maximum projection area, thus confirming the "side-on" immobilization of the PtG. The same behavior is reported by Su et al. [291] for the interaction of Lysozyme at the water-silica interface.

3.4.4. Bovine Serum Albumin blocking step

The introduction of a blocking step between the PtG immobilization step and the incubation in Ab-HRP was taken into consideration with the aim of reducing and/or avoiding the non-specific biomolecules interactions. In fact, the device is exposed to biomolecules, which are able to establish several chemical interactions, such as hydrophobic, hydrophilic and electrostatic. This aspect represents the non-specific component of the generated signal that is hopefully kept as low as possible in a sensing context. In bioassay applications for biomolecules detection, such as ELISA, the incubation with BSA represents a common approach to this issue [292]. Moreover, this is the same blocking agent that was employed in the ELISA-like bioassay performed for the optimization of the chemical functionalization (section 3.3). Therefore, the application of this protein as a blocking agent for this MC-based system was investigated.

In order to test the actual efficiency of BSA as a blocking agent, the PtG/Ab-HRP bioassay was performed on MC arrays. In particular, after the immobilization of the PtG on the APTES/SA derivatized MC surface, BSA 1% dissolved in PBS was put in contact with the MC surface to saturate all the remaining sites, which could establish biomolecules interactions. Finally, the MC arrays were incubated with Ab-HRP and the resonant frequencies were acquired.

a)

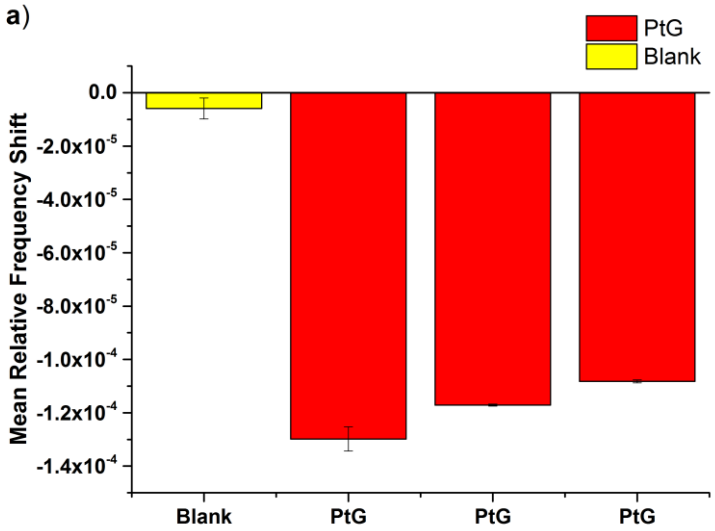
PtG
Blank
Mean Relative Frequency Shift
0.0
-2.0x10-5
-4.0x10-5
-6.0x10-5
-8.0x10-5
-1.0x10-4
-1.2x10-4
-1.4x10-4
Blank
PtG
PtG
PtG

b)

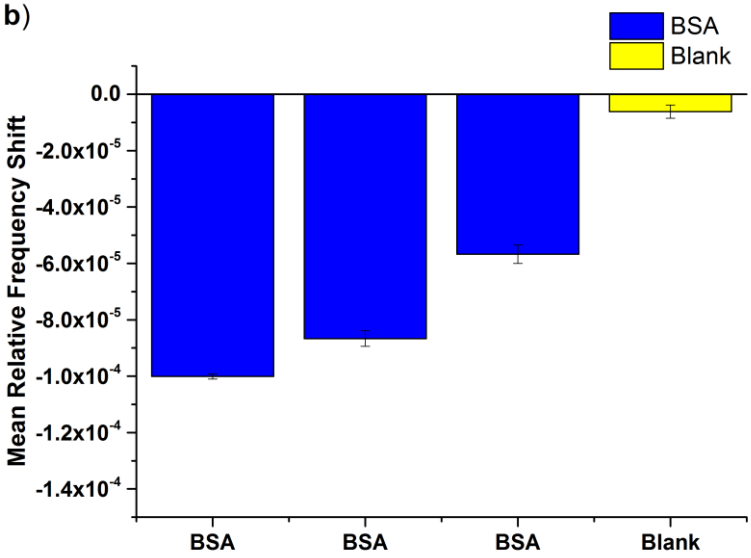
BSA
Blank
Mean Relative Frequency Shift
0.0
-2.0x10-5
-4.0x10-5
-6.0x10-5
-8.0x10-5
-1.0x10-4
-1.2x10-4
-1.4x10-4
BSA
BSA
BSA
Blank

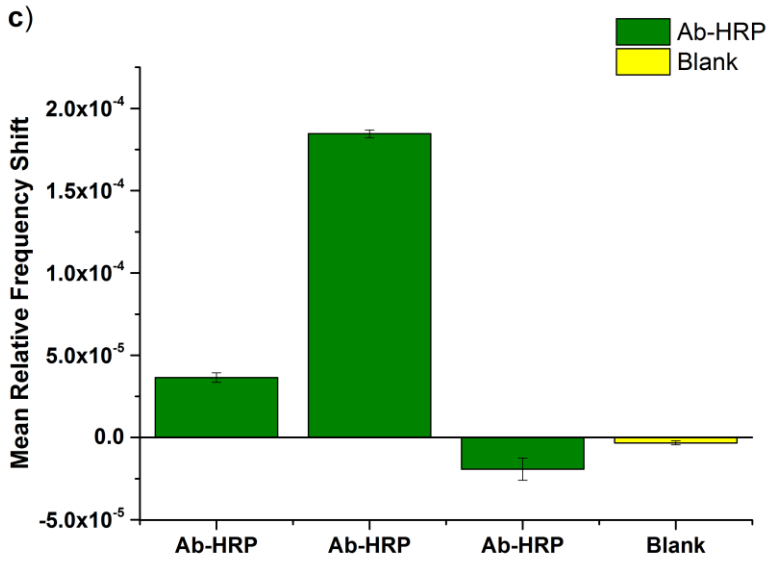

Fig. 3.22. MC arrays evaluation of PtG, BSA and antimouse Ab-HRP molecules deposition: mean relative frequency shifts measured after the incubation with PtG (a), BSA (b) and an antimouse Ab-HRP (c).

In Fig. 3.22, the mean relative frequency shifts respectively acquired after the incubation with PtG, BSA and Ab-HRP (Fig 3.22a-3.22b-3.22c) are reported. After the incubation with the PtG, all the MC arrays showed a decrease in the mean resonant frequencies related to the number of proteins tethered to the MCs surface. As expected, the blank condition experienced a very small relative frequency shift, comparable to the instrumental error. Subsequently, the MC arrays were incubated with BSA with the aim of blocking the remaining available interaction sites of the chemical functionalization. Again, all the MC arrays incubated with the albumin showed a mean relative frequency shift proportional to the number of protein attached to the surface and depending on the geometry of these interacting surfaces defined during the PtG incubation step. Even in this case, the blank condition showed a very small frequency shift (Fig 3.22b). After the blocking step, an anti-mouse Ab-HRP was incubated, expecting an interaction with the PtG previously immobilized on the MCs surface. In Fig. 3.22c, the mean relative frequency shifts experienced by each MC array after the exposition to the Ab-HRP are reported. As it is possible to notice, only one array out of three showed a negative shift (i.e. third MC array); the other two arrays showed positive frequency shifts, which are not comparable in amplitude. This behavior could be the result of the loss in mass on the

suspended beam. Thus, a detachment of BSA proteins during the Ab-HRP incubation, or during the subsequent washing steps, would likely be responsible for the increase of the resonant frequency. In fact, the BSA capability of interacting with the MCs surface depends on the chemical properties of the protein (electrostatic interactions and pI), on the properties of the solution (pH and ionic strength) and on the physico-chemical features of the surface (wettability, roughness, chemical composition), as previously stated for PtG (see section 3.4.2). All of these variables contribute to the definition of a dynamic equilibrium, in which BSA proteins continuously attach and detach from MCs surface. Moreover, it is possible to notice that the blank condition in Fig. 3.22c, which was not incubated with the Ab-HRP, showed a very small shift as expected. This response indicates that the steric hindrance of the Ab-HRP interacting with PtG may result in the detachment of BSA proteins that are close to this interaction site.

3.4.5. Ethanolamine blocking step

Ethanolamine is a small molecule, which presents a primary amine in its structure. This characteristic make this molecule an eligible blocking agent for the reduction of non-specific interactions. In fact, its primary amine group is able to establish a chemical interaction with the terminal carboxyl groups of the APTES/SA chemical functionalization, resulting in the formation of a covalent bond. Moreover, the spatial dimensions of ethanolamine could make it a better choice than BSA because of the lower probability of steric hindrance phenomena in the establishment of the PtG/Ab-HRP interactions.

For these reasons, a PtG/Ab-HRP bioassay was performed on MC arrays. In particular, after the immobilization of PtG on the APTES/SA derivatized MC surface, 10 mM ethanolamine dissolved in PBS (adjusting the pH to 7.5) was put in contact with the MC surface to saturate all the remaining sites, which could establish biomolecules interactions. Finally, MC arrays were incubated with Ab-HRP and the resonant frequencies were characterized.

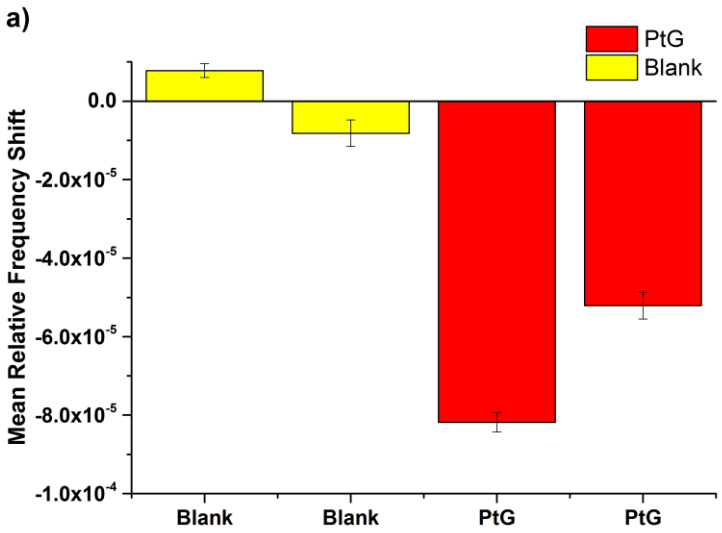
a)
PtG
Blank
Mean Relative Frequency Shift
0.0
-2.0x10-5
-4.0x10-5
-6.0x10-5
-8.0x10-5
-1.0x10-4
Blank
Blank
PtG
PtG

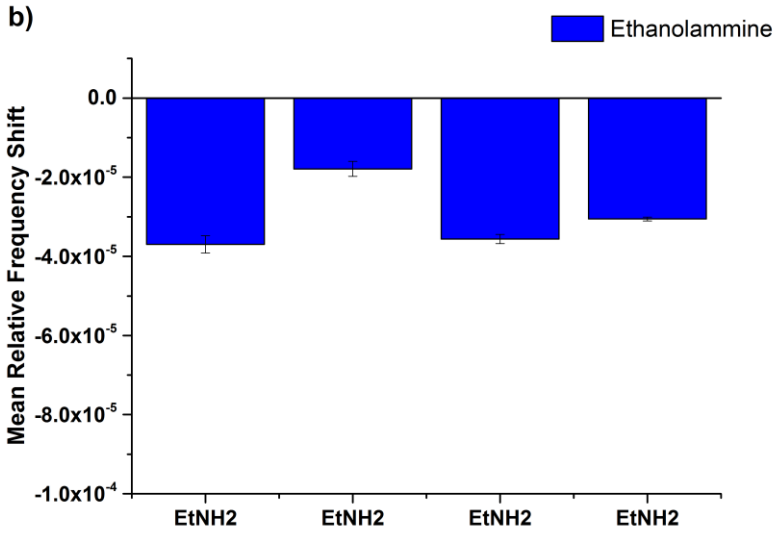
b)
Ethanolammine
Mean Relative Frequency Shift
0.0
-2.0x10-5
-4.0x10-5
-6.0x10-5
-8.0x10-5
-1.0x10-4
EtNH2
EtNH2
EtNH2
EtNH2

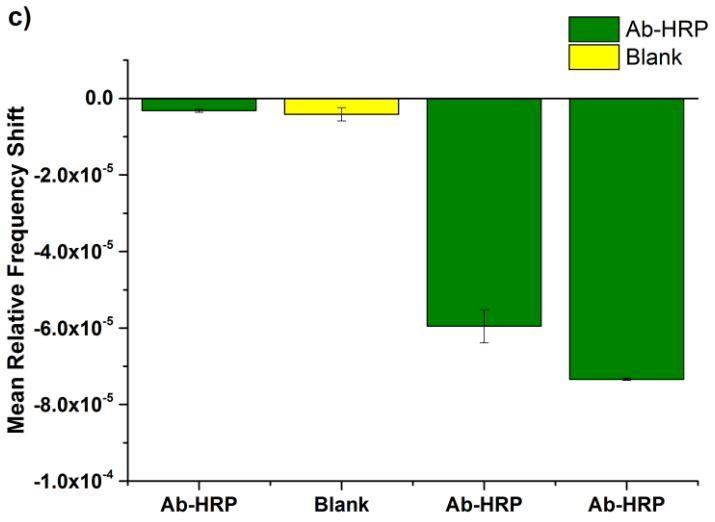

Fig. 3.23. MC arrays evaluation of PtG, ethanolamine and antimouse ab-HRP molecules deposition: mean relative frequency shifts measured after the incubation with PtG (a), ethanolamine (b) and an antimouse Ab-HRP (c).

In Fig. 3.23 the mean relative frequency shifts respectively acquired after the incubation with PtG, ethanolamine and Ab-HRP (Fig 3.23a-3.23b-3.23c) are reported. After the incubation with PtG, two MC arrays out of four were incubated with a PtG containing solution, showing a decrease in the mean resonant frequencies proportional to the number of proteins immobilized on the MCs surface. The two MC arrays that were incubated only with the buffer solution (i.e. blank condition), experienced, as expected, just a very small relative frequency shift. Subsequently, MC arrays were incubated with a 10 mM ethanolamine solution, in order to block the whole remaining available interaction sites of the chemical functionalization. Again, all the MC arrays incubated with ethanolamine showed small mean relative frequency shifts due to the very low mass weight of the blocking molecule (Fig 3.23b). After the blocking step, the anti-mouse Ab-HRP was incubated. In Fig. 3.23c, the mean relative frequency shifts experienced by each MC array after the exposition to the Ab-HRP are reported. As it is possible to notice, two MC arrays out of three, those previously incubated with PtG, showed negative shifts; the other MC array incubated with the Ab-HRP showed a very small mean frequency shift comparable to the instrumental error. This data are very important because show the actual efficiency of ethanolamine as a blocking agent. In fact, PtG was not previously immobilized on this MC array and, after the neutralization of all the interaction sites of the

chemical functionalization by means of ethanolamine, the Ab-HRP was not able to establish any kind of interactions with the MCs surface. Finally, the remaining MC array provide information about the stability of the interaction between the terminal carboxyl groups of the APTES/SA functionalization and the ethanolamine molecule. This MC array was not incubated with PtG, then it was incubated with ethanolamine and finally it was incubated with the buffer solution only (blank condition). It is possible to notice that this MC array experienced a negative mean relative frequency shift only after the incubation with ethanolamine, while after the incubation with the buffer it showed a very small shift.

Thus, this experiment demonstrated that ethanolamine could be considered as a better blocking agent then BSA due to the presence of a primary amine group that can establish covalent interactions with the carboxyl groups of APTES/SA functionalization.

3.5. MC arrays for the detection of Domain III of the Dengue Virus 1

3.5.1. Domain III-Dengue Virus 1/DV32.6 antibody interaction

The introduction of the blocking step involving ethanolamine demonstrated to give better results when compared to the BSA-based one. In particular, ethanolamine resulted to be a stable blocking agent maintaining the capability to avoid or reduce non-specific interactions of proteins to the MCs surface. Thanks to this improvement, this MCs-based system was used as a sensing platform for the study of the interaction between the envelope glycoprotein domain III of the Dengue virus type 1 (DIII-DV1) and the specific antibody DV32.6. This virus is responsible for the Dengue Hemorrhagic Fever (DHF) and is the leading cause of illness and death in the tropical and subtropical area. No cure or vaccine is available for the treatment of patients affected by this pathology, thus a better understanding of the interaction between the pathogens and antibodies is expected to accelerate vaccine development.

In the first instance, an ELISA-like was performed with the aim of evaluating the actual capability of the antibody responsible for the specific recognition of the DIII-DV1. This bioassay was performed on APTES/SA derivatized macro samples, on which DIII-DV1 was immobilized before the incubation with the FullAb-DV32.6. A HRP-conjugated PtG, able to establish

interactions with the Fc of the Ab through its Ab-binding domains, was used to amplify the signal.

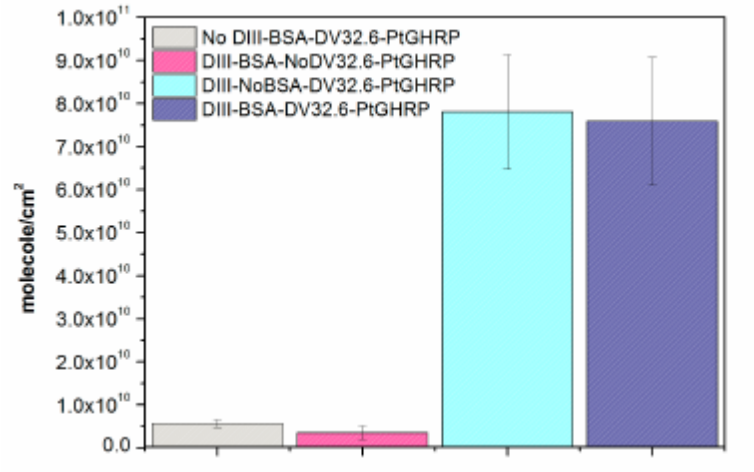

Fig. 3.24. ELISA evaluation of DIII-DV1/DV32.6 interaction: number of molecules/cm^2 of DIII-DV1/DV32.6 evaluated through an ELISA-like bioassay.

In Fig. 3.24, the number of molecules/cm^2 for each experimental condition are reported. The two positive conditions (i.e. DIII/No BSA/DV32.6/PtG-HRP and DIII/BSA/DV32.6/PtG-HRP) showed a signal that is clearly distinguishable from the negative conditions (i.e. No DIII/BSA/DV32.6/PtG-HRP and DIII/BSA/No DV32.6/PtG-HRP). In particular, their values (≈ 8.0 × 10^{10} molecules/cm^2) were about 16-fold times higher than the blank signal values (≈5.0 × 10^9 molecules/cm^2). These data indicates that the DIII-DV1/DV32.6 interaction is fully functional and the DV32.6 is able to recognize the DIII-DV1 in a specific manner.

The same bioassay was then performed on MCs arrays with the aim of evaluating the DIII-DV1/DV32.6 interaction. In doing so, two sets of MC arrays were used to make a comparison between BSA and ethanolamine blocking agents. Thus, a first set of MC arrays was incubated with BSA as blocking agent; while a second set of MC arrays was incubated with ethanolamine. In Tab. 3.6 and Tab. 3.7, the experimental conditions are reported. For the sake of clarification, the immobilization step indicates the biomolecule immobilized on the APTES/SA functionalization, whereas blocking step indicates the (bio)molecule used as blocking agent and the incubation step indicates the biomolecule incubated at the final step of the bioassay.

Table 3.6. Experimental conditions of the first set of MC arrays.

Immobilization Step	Blocking Step	Incubation Step
No DIII-DV1	BSA	DV32.6
DIII-DV1	BSA	DV32.6
DIII-DV1	BSA	DV32.6
DV32.6	BSA	DIII-DV1
DV32.6	BSA	DIII-DV1

Table 3.7. Experimental conditions of the second set of MC arrays.

Immobilization Step	Blocking Step	Incubation Step
No DIII-DV1	Ethanolamine	DV32.6
No DV32.6	Ethanolamine	DIII-DV1
DIII-DV1	Ethanolamine	DV32.6
DIII-DV1	Ethanolamine	DV32.6
DV32.6	Ethanolamine	DIII-DV1
DV32.6	Ethanolamine	DIII-DV1

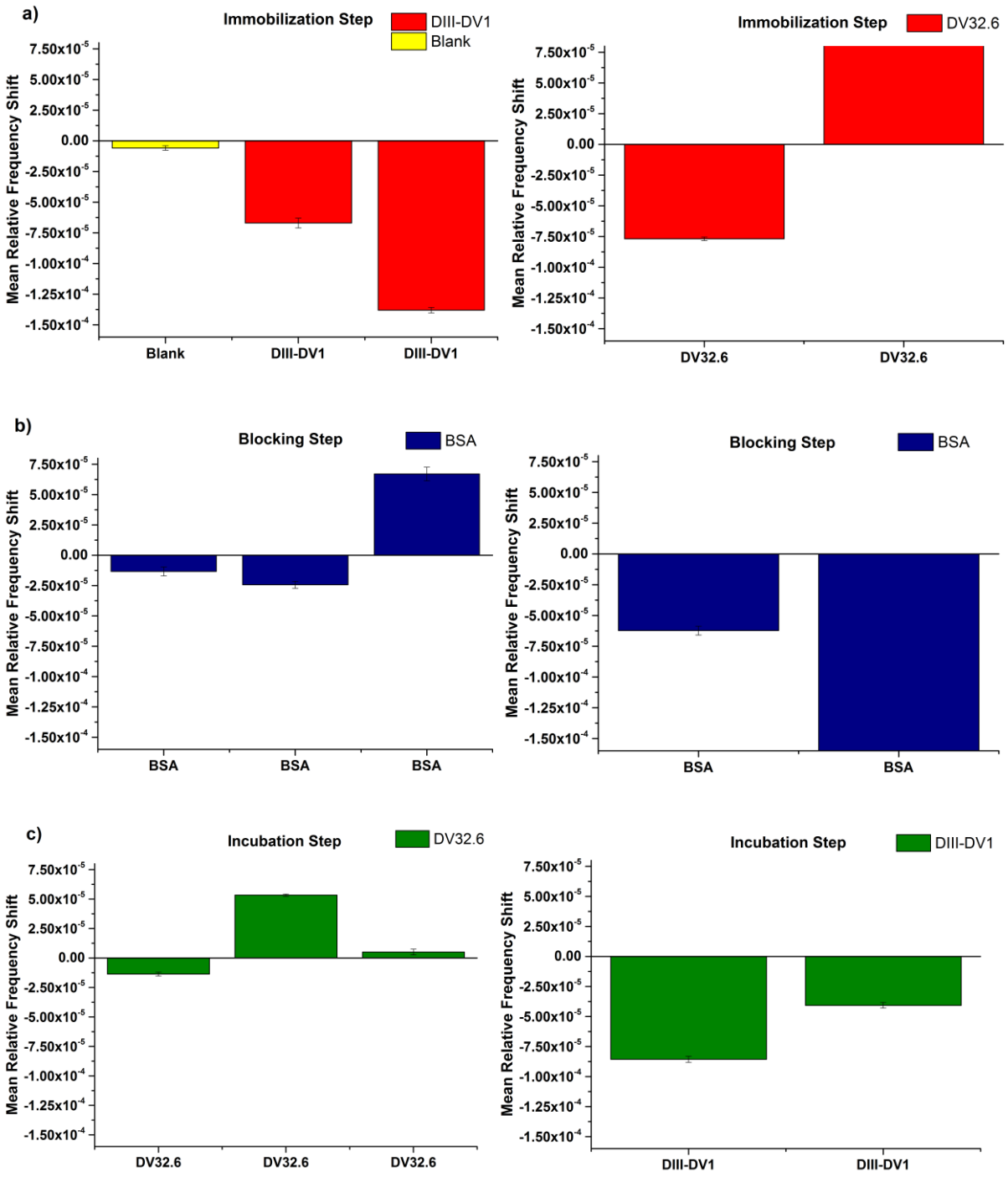

Fig. 3.25. MC arrays evaluation of DIII-DV1, BSA and DV32.6 molecules deposition: mean relative frequency shifts measured after the incubation with DIII-DV1 (a), BSA 1% (b) and DV32.6 antibody (c).

In Fig. 3.25, the mean relative frequency shifts acquired from the MC arrays that were incubated with BSA are reported. Concerning the immobilization step, the two MC arrays that were incubated with the DIII-DV1 showed a frequency shift that was roughly ten to twenty

times higher than the shift recorded from the blank condition ($-5.8 \pm 1.8 \times 10^{-6}$). The two MC arrays that were incubated with the DV32.6 showed a contrasting behavior: the first one showed a not negligible negative frequency shift, indicating that a certain amount of DV32.6 was immobilized on MCs surface. Instead, the second one showed a positive frequency shift with an amplitude that was roughly twenty five times higher than the signal acquired from the first one ($+2.22 \pm 0.05 \times 10^{-3}$, Fig. 3.25a). In Fig. 3.25b, the mean relative frequency shifts acquired after the blocking step with BSA are reported. As it is possible to notice, the MC arrays experienced negative frequency shifts except the third MC array (starting form left), previously incubated with the DIII-DV1, indicating perhaps a non-uniform adsorption of BSA molecules throughout the entire MCs surface. Moreover, the fifth MC array, which was incubated with the DV32.6 and exhibited a huge positive shift at the immobilization step, showed a negative frequency shift similar to the one recorded in the previous step ($-1.62 \pm 0.04 \times 10^{-3}$, Fig. 3.25b). In the final incubation step, the first three MC array were incubated with the DV32.6 antibody, while the remaining two MC arrays were incubated with the DIII-DV1. In Fig. 3.25c, the mean relative frequency shifts measured are reported. The first three MC arrays incubated with the DIII-DV1 showed different frequency shifts: in particular, the first one experienced a shift that was slightly higher than the instrumental error. Note that DIII-DV1 was not previously immobilized on this MC array, thus a small signal value at the final incubation step is consistent with the experimental condition (blank condition). The second and third MC arrays represent, instead, the positive conditions: as it is possible to observe in Fig. 3.25c, both MC arrays showed positive relative frequency shifts with different magnitude. The second MC array experienced the frequency shift with the highest amplitude ($5.3 \pm 0.1 \times 10^{-5}$), while the third one showed a frequency shift very close to the instrumental error. In the former, BSA molecules may have detached from the silicon surface, resulting in the decrease of MC mass and preventing the detection of the possible DIII-DV1/DV32.6 interactions. This would confirm the same phenomenon observed in section 3.4.4, in which the BSA blocking demonstrated to be a source of unreliability for the realization of the bioassay on MC arrays, due to the dynamic interactions that these biomolecules are able to establish with the MCs surface. The remaining MC arrays, which were incubated with the antibody, showed negative relative shifts suggesting that the previously immobilized DV32.6 was able to interact with the DIII-DV1 biomolecules, which were put in contact with the MC arrays at the final incubation step. As it is possible to observe, the first MC array was the only one that experienced a

negative frequency shifts in each experimental step. Taking in consideration the DV32.6 antibodies immobilized on the APTES/SA functionalization and the DIII-DV1 incubated at the final step, it is possible to calculate the experimental surface density and provide information about the interactions of these proteins. In particular, the mean surface density of the DV32.6 immobilized on MCs surface is $4.49 \pm 0.51 \times 10^{11}$ molecules/cm^2, while the number of DIII-DV1 biomolecules recorded from the experimental data corresponds to $3.62 \pm 0.95 \times 10^{12}$ molecules/cm^2. The DV32.6/DIII-DV1 ratio was 1:8, indicating that for each DV32.6 antibody immobilized on the silicon surface eight DIII-DV1 molecules were able to establish some sort of interaction. This ratio is obviously too high considering the Ag/Ab interaction, in which each antibody is able to interact with a maximum of two antigen biomolecules. Such an outcome may be the result of DIII-DV1 clusters formation. In fact, it is reasonable that DIII-DV1 molecules assemble/arrange themselves into clusters through electrostatic interactions when put in solution. In this way, these clusters may interact with the immobilized DV32.6 antibodies with a resulting ratio that is superior to the 2:1 Ag/Ab interaction.

The second set of MC arrays was incubated with ethanolamine 10 mM during the blocking step. Refer to Tab. 3.7 for the detailed experimental conditions. In Fig. 3.26 the mean relative frequency shifts recorded for each step of the bioassay are reported.

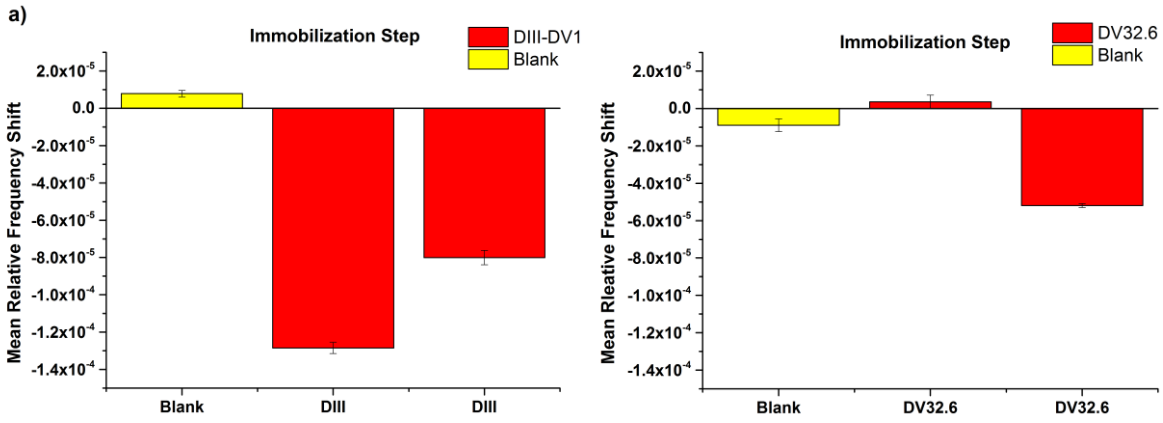

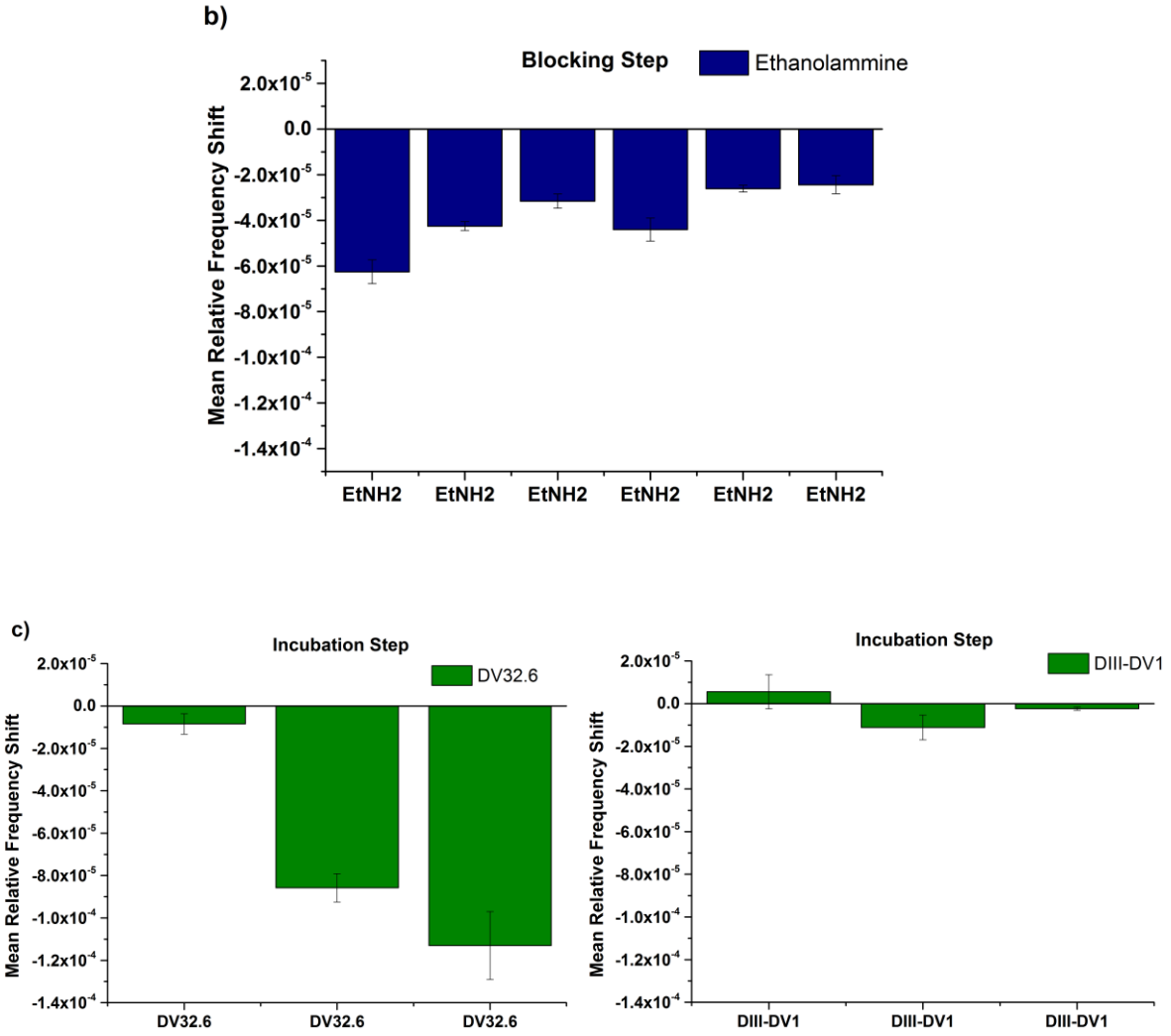

Fig. 3.26. MC arrays evaluation of DIII-DV1, ethanolamine and DV32.6 molecules deposition: the box charts show the mean relative frequency shifts measured after the incubation with DIII-DV1 (a), ethanolamine (b) and DV32.6 antibody (c).

During the immobilization step, two MC arrays were not incubated with biomolecules (blank), while of the remaining four, two were incubated with DIII-DV1 and two with DV32.6. Both the two MC arrays that represent the blank conditions showed a small relative frequency shift, not significantly different from the instrumental error. The two MC arrays on which was immobilized the DIII-DV1 experienced negative frequency shifts, indicating that a certain amount of biomolecules was immobilized on MC surface. The remaining two MC arrays, which during this step were incubated with the DV32.6, showed different behaviors: a very small shift was acquired from the first one, while a not negligible negative frequency shift were recorded from the second. For the former, data suggests that the DV32.6 was not able to

establish covalent interactions with the APTES/SA functionalization, thus indicating that the DV32.6 was not immobilized on the MCs surface. For the latter, the negative frequency shift is to be related with the mass of adsorbed DV32.6 immobilized on the chemical functionalization. Concerning the blocking step, the whole set of MC arrays were incubated with ethanolamine and all of them experienced a negative mean relative frequency shift. In the final step, MC arrays were incubated with the DIII-DV1 and/or the DV32.6 in order to investigate the stoichiometry interactions of these two biomolecules. In particular, the two blank conditions were respectively incubated with DV32.6 and DIII-DV1 with the aim of confirming the good blocking performance of ethanolamine as blocking agent. Data showed that after the blocking step, any incubated biomolecule was not able to interact with the surface of the device if the interacting partner is not directly immobilized on APTES/SA. Thus, this outcome confirms that ethanolamine is an efficient blocking agent. The two MC arrays incubated with the DV32.6 showed a negative frequency shift corresponding to the mass of biomolecules able to establish interactions with those of DIII-DV1 that were previously immobilized on the APTES/SA functionalization at the immobilization step. Finally, both MC arrays incubated with the DIII-DV1 experienced very small shift of the same order of magnitude of the instrumental error. It is important to notice that the first MC array incubated with the DIII-DV1, on which was previously immobilized the DV32.6, at the first step of the bioassay showed a very small shift, indicating that the DV32.6 was not tethered to the functionalized silicon surface. Thus, this phenomenon is consistent with the experimental data acquired. In the first place, the DV32.6 was not immobilized as highlighted by these data and the DIII-DV1 was not able to interact with the MCs surface after an efficient blocking step represented by ethanolamine incubation. However, the second MC array incubated with the DIII-DV1 experienced a small frequency shift even if the experimental data indicated that a certain amount of DV32.6 was tethered to the MCs surface at the immobilization step. This behavior may be the consequence of a non-oriented deposition of the DV32.6 antibody on the surface, resulting in the absence or in a very low availability of binding sites.

From these data, it is possible to notice that the bioassay performed on MC arrays gave better results when the DIII-DV1 was immobilized on the MCs surface. Thus, experimental surface densities of the DIII-DV1 and the DV32.6 were calculated from the gravimetric data acquired during the measurement sessions.

First, the same bioinformatics approach used in Section 3.4.3 was applied to the DIII-DV1 model in order to calculate the maximum and minimum projection areas of the protein. Thus, the maximum and minimum theoretical surface densities were calculated starting from the data (Tab. 3.8).

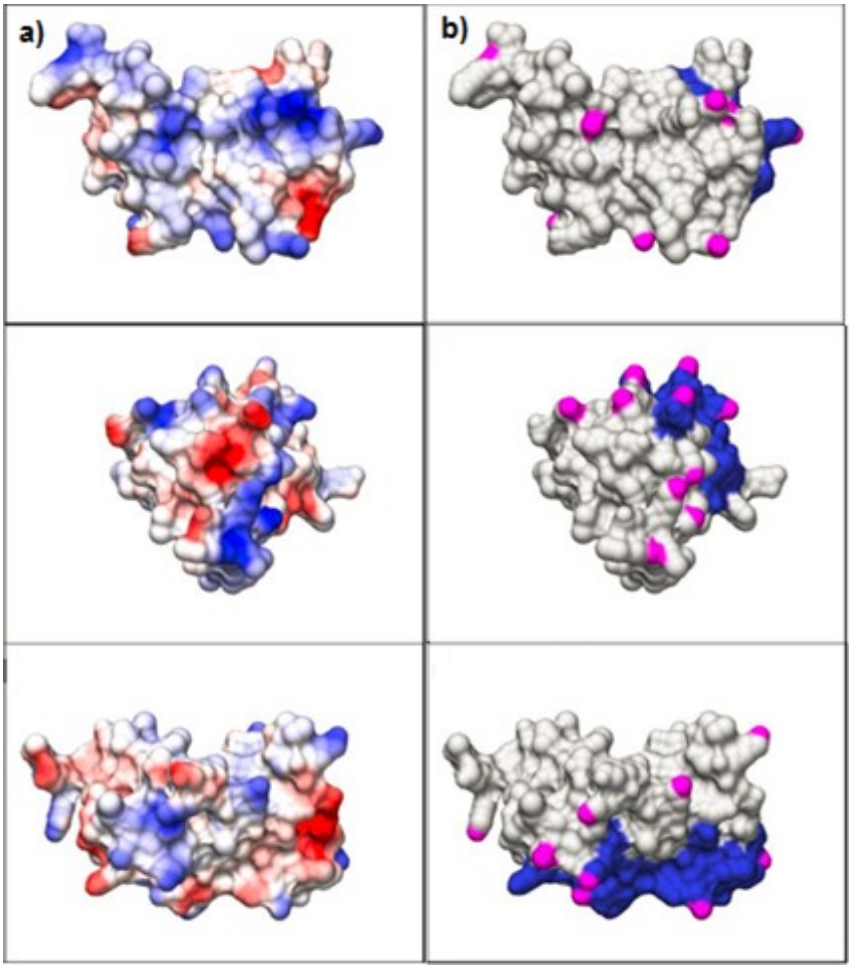

Fig. 3.27. Amine functionalities and surface electrostatic potential of DIII-DV1: the image reports the surface amino acids electrostatic potential (a) and the amine functionalities (b) of the envelope glycoprotein Domain III of the Dengue Virus-1.

Table 3.8. DIII-DV1 projection areas and theoretical molecules/cm^2: the table reports the maximum and minimum projection areas and the estimated theoretical surface densities of DIII-DV1 protein.

	Max projection area [Å^2]	Min projection area [Å^2]	Min theoretical molecules/cm^2 [× 10^{12}]	Max theoretical molecules/cm^2 [× 10^{12}]
DIII-DV1	1,372.58	1,149.40	7.29	8.70

However, it was not possible to apply the same procedure to the DV32.6 antibody provided by the Institute for Research in Biomedicine (IRB) of Bellinzona because the pdb model of this biomolecule was not available.

Table 3.9. DIII-DV1 and DV32.6 molecular weights and experimental mean molecules/cm^2: the table reports the molecular weights of the DIII-DV1/DV32.6 proteins and their experimental mean surface densities.

	Molecular weight [Da]	Experimental mean molecules/cm^2
DIII-DV1	12,000	$7.23 \pm 0.15 \times 10^{12}$
DV32.6	150,000	$5.49 \pm 0.36 \times 10^{11}$

In Tab. 3.9, the experimental surface densities in molecules/cm^2 calculated for the DIII-DV1 and the DV32.6 biomolecules are reported. As it is possible to notice, the mean surface density of the DIII-DV1 is very close to the minimum theoretical surface density, indicating that the immobilization procedure allows to obtain a highly packed layer of proteins. With the aim of better understand the interactions between DIII-DV1 and DV32.6 established on MC surface, the DIII-DV1/DV32.6 ratio of molecules/cm^2 was defined: this ratio is equal to 13:1, meaning that for a surface on which thirteen DIII-DV1 biomolecules are immobilized corresponds a DV32.6 antibody able to interact with its target protein. The interaction ratio represents an evaluation of the capability of the DV32.6 antibody to interact with its specific target DIII-DV1. Moreover, it may be related to the neutralization capability of this specific antibody toward

the dengue virus, giving information about the efficiency of it as a protection against the host cell infection.

Chapter 4: Conclusions

In this work, a MC-based array system was used for the evaluation of biomolecular interactions. In particular, dynamic-mode operated MC arrays have been used as weighting device, with the aim of quantifying proteins that were able to interact with the MCs sensing surface. The work consisted of two parts: in the first one, the critical aspects that emerge when working with biological objects were identified and different improvements of the bioassay procedure were implemented. In particular, the washing steps procedure revealed to be potential source of false positives due to the deposition of salt residues coming from the use of saline buffers. The increase of the volumes and of the contact time of the buffers employed during the washing steps allowed to acquire more reliable data during the measurements sessions. Another source of variability was identified in the previously used surface chemical functionalization, based on the widely applied APTES/GA. After the self-assembly of APTES molecules, the further derivatization with GA in aqueous solution could lead to polymerization processes, generating an unstable multi-layered structure on the MC surface. Therefore, a novel chemical surface modification base on APTES and SA was developed, allowing the exposure of terminal carboxyl groups on the sensing surface. Moreover, the introduction of the EDC/s-NHS protocol allowed activating those carboxyl groups, making them more reactive toward amine groups present on the exposed protein residues. In the first instance, the APTES/SA functionalization was characterized by means of OCA, XPS and AFM analysis and then compared with the previously employed APTES/GA functionalization. The former demonstrated to be a better surface chemical modification than APTES/GA in terms of homogeneity and reproducibility. Moreover, the two chemical functionalizations were investigated for their protein grafting capability through a newly proposed ELISA-like bioassay. Even in this case, the APTES/SA functionalization revealed to be a better performing substrate for proteins immobilization than APTES/GA. Finally, the APTES/SA and APTES/GA functionalizations were derivatized on MC arrays with the aim of testing the deposition process reliability on our sensing platform. First, a molecular modeling tool was used for the evaluation of the theoretical surface density corresponding to a monolayer deposition of molecules. From the comparison of the experimental and theoretical surface densities, the data highlighted that the APTES/SA deposition process produced an

arrangement of molecules that is very close to a monolayer, confirming the high-grade homogeneity observed from the AFM analysis. Instead, the APTES/GA deposition process resulted in a surface density that is far higher than the theoretical value expected for a monolayer deposition of molecules, indicating a multi-layered structure.

In the second part, the improvements reported above were applied to our MC-based sensing platform for the quantification and evaluation of biomolecular interactions established on the MC surface, such as antigen-antibody interactions. The same molecular modeling tool was used for the estimation of two theoretical surface densities corresponding to a monolayer arrangement of Protein G exposing the maximum and the minimum projection areas on the silicon resonator surface. Then, Protein G and BSA were immobilized on APTES/SA derivatized MC arrays and the experimental surface density was evaluated. The experimental surface density was very close to the theoretical minimum surface density, indicating that proteins were able to arrange themselves on the sensing surface exposing the maximum projection area. Thus, this MC-based array system allowed to directly estimate the preferential orientation of proteins attached to the sensing surface. Afterwards, the specific interaction between the envelope glycoprotein domain III of the dengue virus (DIII-DV1) and the DV32.6 antibody was studied. After the attachment of the DIII-DV1 on the MC surface, the antibody DV32.6 was incubated and it was able to interact with its target immobilized on the sensing surface. From the experimental data, it was possible to evaluate the surface density of the two biomolecules and calculate the DIII-DV1/DV32.6 stoichiometry ratio. Therefore, this MC-based array system allowed to provide information about the binding capability of this specific antibody against its target (DIII-DV1) and, consequently, to better understand the host cell infection. Since nowadays there is no cure or vaccine available, the study of the interaction between the pathogen and specific antibodies is expected to accelerate the development of a vaccine. As a future perspective, an interesting application of this MC array system will be the study of the interaction of different antibodies with the entire virus. In such a way, it will be possible to investigate the neutralizing capability of antibodies on a tri-dimensional structure, which presents a plethora of target epitopes.

REFERENCES

[1] A. Boisen, S. Dohn, S. S. Keller, S. Schmid, M. Tenje. Cantilever-like micromechanical sensors. Rep. Prog. Phys. 74 (2011).

[2] C. Steffens, A. Manzoli, J. E. Oliveira, F. L. Leite, D. S. Correa, P. S. P. Herrmann. Bio-inspired sensor for insect pheromone analysis based on polyaniline functionalized AFM cantilever sensor. Sensors and Actuators B: Chemical 191 (2014), 643-649.

[3] B. Liu, X. Wang. Flame radiant heat flux measurement based on bi-material cantilever. International Journal of Thermal Sciences 79 (2014), 60-66.

[4] H. H. Kim, H. J. Jeon, H. K. Cho, J. H. Cheong, H. S. Moon, J. S. Go. Highly sensitive microcantilever biosensors with enhanced sensitivity for detection of human papilloma virus infection. Sensors and Actuators B: Chemical 221 (2015), 1372–1383.

[5] D. R. Thévenot, K. Toth, R. A. Durst, G. S. Wilson. Electrochemical biosensors: recommended definitions and classification. Biosensors and Bioelectronics 16 (2001), 121–131.

[6] P. Mehrotra. Biosensors and their applications – A review. Journal of Oral Biology and Craniofacial Research (2016). DOI: 10.1016/j.jobcr.2015.12.002.

[7] M. Frantlović, I. Jokić, Z. Djurić, K. Radulović. Analysis of the competitive adsorption and mass transfer influence on equilibrium mass fluctuations in affinity-based biosensors. Sensors and Actuators B: Chemical 189 (2013), 71–79.

[8] P. Das, M. Das, S. R. Chinnadayyala, I. M. Singha, P. Goswami. Recent advances on developing 3rd generation enzyme electrode for biosensor applications. Biosensors and Bioelectronics 79 (2016), 386–397.

[9] S. A. Bhakta, E. Evans, T. E. Benavidez, C. D. Garcia. Protein adsorption onto nanomaterials for the development of biosensors and analytical devices: A review. Analytica Chimica Acta 872 (2015), 7–25.

[10] S. Rodriguez-Mozaz, M.J. Lopez de Alda, D. Barceló. Biosensors as useful tools for environmental analysis and monitoring. Analytical and Bioanalytical Chemistry 386 (2006), 1025-1041.

[11] C. Davies. Immunoassay perfomance measures. The Immunoassay Handbook, Fourth Ediotion (2013), 11-26.

[12] C. H. Self, S. Thompson, T. Street, K. J. Lamb, G. Duffin, J. L. Dessi, M. Turnbull. Non-competitive Immunoassays for Small Molecules—the Anti-complex and Selective Antibody Systems. The Immunoassay Handbook, Fourth Edition (2013), 61-65.

[13] G. D. Griffin, D. N. Stratis-Cullum, T. E. McKnight. Biosensors. Reference Module in Biomedical Sciences (2014).

[14] C. I.L. Justino, A. C. Freitas, R. Pereira, A. C. Duarte, T. A. P. Rocha Santos. Recent developments in recognition elements for chemical sensors and biosensors. TrAC Trends in Analytical Chemistry 68 (2015), 2-17.

[15] G. Sener, L. Uzun, R. Say, A. Denizli. Use of molecular imprinted nanoparticles as biorecognition element on surface plasmon resonance sensor. Sensors and Actuators B: Chemical 160 (2011), 791–799.

[16] H. Shi, R. Wang, J. Yang, H. Ren, S. Liu, T. Guo. Novel imprinted nanocapsule with highly enhanced hydrolytic activity for organophosphorus pesticide degradation and elimination. European Polymer Journal 72 (2015), 190–201.

[17] W. E. Paul. Fundamental Immunology, Seventh Edition (2013).

[18] M. J. Day. Introduction to Antigen and Antibody Assays. Topics in Companion Animal Medicine (2015).

[19] H. Orii, T. Yamaguchi, K. Watanabe. Single-step cloning of a hybridoma producing a monoclonal antibody against a target protein. Analytical Biochemistry 434 (2013), 52–53.

[20] Y. Zhou, X. L. Tian, Y. S. Li, F. G. Pan, Y. Y. Zhang, J. H. Zhang, X. R. Wang, H. L. Ren, S. Y. Lu, Z. H. Li, Z. S. Liu, Q. J. Chen, J. Q. Liu. Development of a monoclonal antibody-based sandwich-type enzyme-linked immunosorbent assay (ELISA) for detection of abrin in food samples. Food Chemistry 135 (2012), 2661–2665.

[21] E. Dráberová, L. Stegurová, V. Sulimenkoa, Z. Hájková, P. Dráber, Pavel Dráber. Quantification of α-tubulin isotypes by sandwich ELISA with signal amplification through biotinyl-tyramide or immuno-PCR. Journal of Immunological Methods 395 (2013), 63–70.

[22] J. Lamontagne, C. Mills, R. Mao, C. Goddard, D. Cai, H. Guo, A. Cuconati, T. Block, X. Lu. Screening and identification of compounds with antiviral activity against hepatitis B virus using a safe compound library and novel real-time immune-absorbance PCR-based high throughput system. Antiviral Research 98 (2013), 19–26.

[23] Y. Gusev, J. Sparkowski, A. Raghunathan, H. Ferguson Jr., J. Montano, N. Bogdan, B. Schweitzer, S. Wiltshire, S. F. Kingsmore, W. Maltzman, V. Wheeler. Rolling Circle Amplification: A New Approach to Increase Sensitivity for Immunohistochemistry and Flow Cytometry. The American Journal of Pathology 159 (2001), 63–69.

[24] D. Mancardi, M. Daëron. Fc Receptors in Immune Responses. Reference Module in Biomedical Sciences (2014).

[25] V. Crivianu-Gaita, M. Thompson. Immobilization of Fab' fragments onto substrate surfaces: A survey of methods and applications. Biosensors and Bioelectronics 70 (2015), 167–180.

[26] S. de la Cruz, C. Cubillos-Zapata, I. M. López-Calleja, S. Ghosh, M. Alcocer, I. González, R. Martín, T. García. Isolation of recombinant antibody fragments (scFv) by phage display technology for detection of almond allergens in food products. Food Control 54 (2015), 322–330.

[27] R. M. Abou El-Magd, N. F. Vozza, J. A. Tuszynski, D. S. Wishart. Isolation of soluble scFv antibody fragments specific for small biomarker molecule, L-Carnitine, using phage display. Journal of Immunological Methods 428 (2016), 9–19.

[28] N. Aissaoui, J. Landoulsi, L. Bergaoui, S. Boujday, J. F. Lambert. Catalytic activity and thermostability of enzymes immobilized on silanized surface: Influence of the crosslinking agent. Enzyme and Microbial Technology 52 (2013), 336–343.

[29] C. Dähnrich, L. Komorowski, C. Probst, B. Seitz-Polski, V. Esnault, J. F. Wetzels, J. M. Hofstra, E. Hoxha, R. A. Stahl, G. Lambeau, W. Stöcker, W. Schlumberger. Development of a standardized ELISA for the determination of autoantibodies against human M-type

phospholipase A2 receptor in primary membranous nephropathy. Clinica Chimica Acta 421 (2013), 213–218.

[30] K. Gabrovska, J. Ivanov, I. Vasileva, N. Dimova, T. Godjevargova. Immobilization of urease on nanostructured polymer membrane and preparation of urea amperometric biosensor. International Journal of Biological Macromolecules 48 (2011), 620–626.

[31] F. Davis, K. A. Law, N. A. Chaniotakis, D. Fournier, T. Gibson, P. Millner, J. L. Marty, M. A. Sheehan, V. I. Ogurtsov, G. Johnson, J. Griffiths, A. P. F. Turner, S. P. J. Higson. Ultra-sensitive determination of pesticides via cholinesterase-based sensors for environmental analysis. Comprehensive Analytical Chemistry 49 (2007), 311–330.

[32] M. T. Madigan, J. M. Martinko. Brock, Biology of Microorganisms, Eleventh Edition (2007).

[33] R. Häuser, S. Blasche, T. Dokland, E. Haggård-Ljungquist, A. von Brunn, M. Salas, S. Casjens, I. Molineux, P. Uetz. Bacteriophage Protein–Protein Interactions. Advances in Virus Research 83 (2012), 219–298.

[34] N. H. H. Bahara, G. J. Tye, Y. S. Choong, E. B. B. Ong, A. Ismail, T. S. Lim. Phage display antibodies for diagnostic applications. Biologicals 41 (2013), 209–216.

[35] D. J. Quinn, S. Cunningham, B. Walker, C. J. Scott. Activity-based selection of a proteolytic species using ribosome display. Biochemical and Biophysical Research Communications 370 (2008), 77–81.

[36] P. Díez, R. Jara-Acevedo, M. González-González, J. Casado-Vela, N. Dasilva, Q. Lécrevisse, R. Bartolomé, J. C. Claros, A. González, R. López, A. Orfao, M. Fuentes. High-throughgput phage-display screening in array format. Enzyme and Microbial Technology 79-80 (2015), 34–41.

[37] T. Kanamori, Y. Fujino, T. Ueda. PURE ribosome display and its application in antibody technology. Biochimica et Biophysica Acta (BBA) - Proteins and Proteomics 1844 (2014), 1925–1932.

[38] L. A. Landon, W. Harden, C. Illy, S. L. Deutscher. High-throughput fluorescence spectroscopic analysis of affinity of peptides displayed on bacteriophage. Analytical Biochemistry 331 (2004), 60–67.

[39] M. Datto, R. L. Lundblad. DNA, RNA Chemical Properties (Including Sequencing and Next-Generation Sequencing). Reference Module in Biomedical Sciences, Encyclopedia of Cell Biology (2016).

[40] H. Mollasalehi, R. Yazdanparast. Development and evaluation of a novel nucleic acid sequence-based amplification method using one specific primer and one degenerate primer for simultaneous detection of Salmonella Enteritidis and Salmonella Typhimurium. Analytica Chimica Acta 770 (2013), 169–174.

[41] Q. Xue, Y. Lv, H. Cui, X. Gu, S. Zhang, J. Liu. A DNA nanomachine based on rolling circle amplification-bridged two-stage exonuclease III-assisted recycling strategy for label-free multi-amplified biosensing of nucleic acid. Analytica Chimica Acta 856 (2015), 103–109.

[42] C. Acquah, M. K. Danquah, J. L. S. Yon, A. Sidhu, C. M. Ongkudon. A review on immobilised aptamers for high throughput biomolecular detection and screening. Analytica Chimica Acta 888 (2015), 10–18.

[43] K. Groff, J. Brown, A. J. Clippinger. Modern affinity reagents: Recombinant antibodies and aptamers. Biotechnology Advances 33 (2015), 1787–1798.

[44] R. Nezlin. Use of aptamers in immunoassays. Molecular Immunology 70 (2016), 149–154.

[45] F. Radom, P. M. Jurek, M. P. Mazurek, J. Otlewski, F. Jeleń. Aptamers: Molecules of great potential. Biotechnology Advances 31 (2013), 1260–1274.

[46] M. Wehbe, M. Labib, D. Muharemagic, A. S. Zamay, M. V. Berezovski. Switchable aptamers for biosensing and bioseparation of viruses (SwAps-V). Biosensors and Bioelectronics 67 (2015), 280–286.

[47] S. Tom, H. E. Jin, S. W. Lee. Aptamers as functional bionanomaterials for sensor applications. Engineering of Nanobiomaterials (2016), 181-226.

[48] A. M. Varizhuk, A. V. Dezhenkov, Y. G. Kirillova. Chiral Acyclic PNA Modifications: Synthesis and Properties. Studies in Natural Products Chemistry 47 (2016), 261–305.

[49] H. Shi, F. Yang, W. Li, W. Zhao, K. Nie, B. Dong, Z. Liu. A review: Fabrications, detections and applications of peptide nucleic acids (PNAs) microarray. Biosensors and Bioelectronics 66 (2015), 481–489.

[50] E. Rozners. Recent Advances in Chemical Modification of Peptide Nucleic Acids. Journal of Nucleic Acids 2012 (2012).

[51] Y. Choi, G. Metcalf, M. H. Sleiman, D. Vair-Turnbull, S. Ladame. Oligonucleotide-templated reactions based on Peptide Nucleic Acid (PNA) probes: Concept and biomedical applications. Bioorganic & Medicinal Chemistry 22 (2014), 4395–4398.

[52] J. Mertens, C. Rogero, M. Calleja, D. Ramos, J. A. Martìn-Gago, C. Briones, J. Tamayo. Label-free detection of DNA hybridization based on hydration induced tension in nucleic acid films. Nature Nanotechnology 3 (2008), 301-307.

[53] S. A. E. Marras, S. Tyagi, F. R. Kramer. Real-time assays with molecular beacons and other fluorescent nucleic acid hybridization probes. Clinica Chimica Acta 363 (2006), 48–60.

[54] W. Tan, K. Wang, T. J. Drake. Molecular beacons. Current Opinion in Chemical Biology 8 (2004), 547–553.

[55] Y. Li, X. Zhou, D. Ye. Molecular beacons: An optimal multifunctional biological probe. Biochemical and Biophysical Research Communications 373 (2008), 457–461.

[56] Y. Liang, Z. Zhang, H. Wei, Q. Hu, J. Deng, D. Guo, Z. Cui, X. E. Zhang. Aptamer beacons for visualization of endogenous protein HIV-1 reverse transcriptase in living cells. Biosensors and Bioelectronics 28 (2011), 270–276.

[57] L. Jovine. New molecular beacons for targeting double-stranded DNA under native conditions. Trends in Biotechnology 19 (2001), 487-488.

[58] D. Chappell, M. Jacob. Role of the glycocalyx in fluid management: Small things matter. Best Practice & Research Clinical Anaesthesiology 28 (2014), 227–234.

[59] F. Brettner, D. Chappell, M. Jacob. The concept of the glycocalyx – Facts that influence perioperative fluid management. Trends in Anaesthesia and Critical Care 2 (2012), 191–198.

[60] M. M. Manni, J. Sot, F. M. Goñi. Interaction of Clostridium perfringens epsilon-toxin with biological and model membranes: A putative protein receptor in cells. Biochimica et Biophysica Acta (BBA) – Biomembranes 1848 (2015), 797–804.

[61] A. Bunker, A. Magarkar, T. Viitala. Rational design of liposomal drug delivery systems, a review: Combined experimental and computational studies of lipid membranes, liposomes and their PEGylation. Biochimica et Biophysica Acta (BBA) – Biomembranes (2016).

[62] J. Li, R. Sun, C. Hao, G. He, L. Zhang, J. Wang. The behavior of the adsorption of cytochrome C on lipid monolayers: A study by the Langmuir–Blodgett technique and theoretical analysis. Biophysical Chemistry 205 (2015), 33–40.

[63] M. B. Gu, R. J. Mitchell, B. C. Kim. Whole-Cell-Based Biosensors for Environmental Biomonitoring and Application. Biomanufacturing 87 (2004), 269-305.

[64] S. Girotti, E. N. Ferri, M. G. Fumo, E. Maiolini. Monitoring of environmental pollutants by bioluminescent bacteria. Analytica Chimica Acta 608 (2008), 2–29.

[65] R. S. Burlage, G. S. Sayler, F. Larimer. Monitoring of naphthalene catabolism by bioluminescence with nah-lux transcriptional fusions. J. Bacteriol 172 (1990), 4749–4757.

[66] Z. K. Cui, M. Lafleur. Lamellar self-assemblies of single-chain amphiphiles and sterols and their derived liposomes: Distinct compositions and distinct properties. Colloids and Surfaces B: Biointerfaces 114 (2014), 177–185.

[67] F. Movahedi, R. G. Hu, D. L. Becker, C. Xu. Stimuli-responsive liposomes for the delivery of nucleic acid therapeutics. Nanomedicine: Nanotechnology, Biology and Medicine 11 (2015), 1575–1584.

[68] J. Tang, Y. Huang, H. Liu, C. Zhang, D. Tang. Novel glucometer-based immunosensing strategy suitable for complex systems with signal amplification using surfactant-responsive cargo release from glucose-encapsulated liposome nanocarriers. Biosensors and Bioelectronics 79 (2016), 508–514.

[69] H. W. Yu, Y. S. Wang, Y. li, G. L. Shen, H. l. Wu, R. Q. Yu. One Step Highly Sensitive Piezoelectric Agglutination Method for Cholera Toxin Detection Using GM1 Incorporated Liposome. Procedia Environmental Sciences 8 (2011), 248–256.

[70] T. Shahar, N. Tal, D. Mandler. Molecularly imprinted polymer particles: Formation, characterization and application. Colloids and Surfaces A: Physicochemical and Engineering Aspects 495 (2016), 11–19.

[71] P. S. Sharma, Z. Iskierko, A. Pietrzyk-Le, F. D'Souza, W. Kutner. Bioinspired intelligent molecularly imprinted polymers for chemosensing: A mini review. Electrochemistry Communications 50 (2015), 81–87.

[72] M. Peeters, K. Eersels, T. Junkers, P. Wagner. Molecularly Imprinted Polymers: Synthetic Receptors for Diagnostic Medical Devices. Molecularly Imprinted Catalysts (2016), 253–271.

[73] Z. Iskierko, P. S. Sharma, K. Bartold, A. Pietrzyk-Le, K. Noworyta, W. Kutner. Molecularly imprinted polymers for separating and sensing of macromolecular compounds and microorganisms. Biotechnology Advances 34 (2016), 30–46.

[74] C. Kokkinos, A. Economou, M. I. Prodromidis. Electrochemical immunosensors: Critical survey of different architectures and transduction strategies. TrAC Trends in Analytical Chemistry (2015).

[75] É. Lojou, P. Bianco. Application of the electrochemical concepts and techniques to amperometric biosensor devices. Journal of Electroceramics 16 (2006), 79-91.

[76] S. Liu, H. Gong, Y. Wang, L. Wang. Label-free electrochemical nucleic acid biosensing by tandem polymerization and cleavage-mediated cascade target recycling and DNAzyme amplification. Biosensors and Bioelectronics 77 (2016), 818–823.

[77] C. A. Cordeiro, M. G. de Vries, W. Ngabi, P. E. Oomen, T. I. F. H. Cremers B. H. C. Westerink. In vivo continuous and simultaneous monitoring of brain energy substrates with a multiplex amperometric enzyme-based biosensor device. Biosensors and Bioelectronics 67 (2015), 677–686.

[78] Y. Wen, W. Wen, X. Zhang, S. Wang. Highly sensitive amperometric biosensor based on electrochemically-reduced graphene oxide-chitosan/hemoglobin nanocomposite for nitromethane determination. Biosensors and Bioelectronics 79 (2016), 894–900.

[79] S. A. Tria, D. Lopez-Ferber, C. Gonzalez, I. Bazin, A. Guiseppi-Elie. Microfabricated biosensor for the simultaneous amperometric and luminescence detection and monitoring of Ochratoxin A. Biosensors and Bioelectronics 79 (2016), 835–842.

[80] G. Hughes, R. M. Pemberton, P. R. Fielden, J. P. Hart. Development of a novel reagentless, screen-printed amperometric biosensor based on glutamate dehydrogenase and NAD+,

integrated with multi-walled carbon nanotubes for the determination of glutamate in food and clinical applications. Sensors and Actuators B: Chemical 216 (2015), 614–621.

[81] A. M. Nowicka, M. Fau, T. Rapecki, M. Donten. Polypyrrole-Au Nanoparticles Composite as Suitable Platform for DNA Biosensor with Electrochemical Impedance Spectroscopy Detection. Electrochimica Acta 140 (2014), 65–71.

[82] M. García, P. Batalla, A. Escarpa. Metallic and polymeric nanowires for electrochemical sensing and biosensing. TrAC Trends in Analytical Chemistry 57 (2014), 6-22.

[83] J. M. Encarnação, L. Rosa, R. Rodrigues, L. Pedro, F. A. da Silva, J. Gonçalves, G. N. M. Ferreira. Piezoelectric biosensors for biorecognition analysis: Application to the kinetic study of HIV-1 Vif protein binding to recombinant antibodies. Journal of Biotechnology 132 (2007), 142–148.

[84] P. Skládal. Piezoelectric biosensors. TrAC Trends in Analytical Chemistry (2015).

[85] J. L. Casteleiro-Roca, J. L. Calvo-Rolle, M. C. Meizoso-Lopez , A. Piñón-Pazos , B. A. Rodríguez-Gómez. New approach for the QCM sensors characterization. Sensors and Actuators A: Physical 207 (2014), 1–9.

[86] H. J. Lee, J. G. Yook. Recent research trends of radio-frequency biosensors for biomolecular detection. Biosensors and Bioelectronics 61 (2014), 448–459.

[87] W. P. Jakubik. Surface acoustic wave-based gas sensors. Thin Solid Films 520 (2011), 986–993.

[88] I. Voiculescua, A. N. Nordin. Acoustic wave based MEMS devices for biosensing applications. Biosensors and Bioelectronics 33 (2012), 1–9.

[89] H. Y. Zhang, H. Q. Pan, B. L. Zhang, J. L. Tang. Microcantilever Sensors for Chemical and Biological Applications in Liquid. Chinese Journal of Analytical Chemistry 40 (2012), 801–808.

[90] T. P. Burg, M. Godin, S. M. Knudsen, W. Shen, G. Carlson, J. S. Foster, K. Babcock, S. R. Manalis. Weighing of biomolecules, single cells and single nanoparticles in fluid. Nature 446 (2007), 1066.

[91] Y. H. Zheng, T. C. Hua, D. W. Sun, J. J. Xiao, F. Xu, F. F. Wang. Detection of dichlorvos residue by flow injection calorimetric biosensor based on immobilized chicken liver esterase. Journal of Food Engineering 74 (2006), 24–29.

[92] B. Danielsson. Calorimetric biosensors. Journal of Biotechnology 15 (1990), 187-200.

[93] S. M. Yoo, S. Y. Lee. Optical Biosensors for the Detection of Pathogenic Microorganisms. Trends in Biotechnology 34 (2016), 7-25.

[94] L. G. Carrascosa, C. S. Huertas, L. M. Lechuga. Prospects of optical biosensors for emerging label-free RNA analysis. TrAC Trends in Analytical Chemistry (2016).

[95] D. Ghosh, N. Chattopadhyay. Gold and silver nanoparticles based superquenching of fluorescence: A review. Journal of Luminescence 160 (2015), 223–232.

[96] A. Zuber, M. Purdey, E. Schartner, C. Forbes, B. van der Hoek, D. Giles, A. Abell, T. Monro, H. Ebendorff-Heidepriem. Detection of gold nanoparticles with different sizes using absorption and fluorescence based method. Sensors and Actuators B: Chemical 227 (2016), 117–127.

[97] T. Etrych, H. Lucas, O. Janoušková, P. Chytil, T. Mueller, K. Mäder. Fluorescence optical imaging in anticancer drug delivery. Journal of Controlled Release 226 (2016), 168–181.

[98] K. Licha, U. Resch-Genger. Fluorescent Reporters and Optical Probes. Comprehensive Biomedical Physics (2014), 85-109.

[99] M. Liu, Z. Lin, J. M. Lin. A review on applications of chemiluminescence detection in food analysis. Analytica Chimica Acta 670 (2010), 1–10.

[100] Q. Xiao, J. M. Lin. Advances and Applications of Chemiluminescence Immunoassay in Clinical Diagnosis and Foods Safety. Chinese Journal of Analytical Chemistry 43 (2015), 929–938.

[101] E. Helmerhorst, D. J. Chandler, M. Nussio, C. D. Mamotte. Real-time and Label-free Bio-sensing of Molecular Interactions by Surface Plasmon Resonance: A Laboratory Medicine Perspective. Clin Biochem Rev 33 (2012), 161-173.

[102] S. Roh, T. Chung, B. Lee. Overview of the Characteristics of Micro- and Nano-Structured Surface Plasmon Resonance Sensors. Sensors 11 (2011), 1565-1588.

[103] J. Mitchell. Small Molecule Immunosensing Using Surface Plasmon Resonance. Sensors 10 (2010), 7323-7346.

[104] E. Mauriz, M. C. García-Fernández, L. M. Lechuga. Towards the design of universal immunosurfaces for SPR-based assays: A review. TrAC Trends in Analytical Chemistry (2016).

[105] C. Novara, A. Lamberti, A. Chiadò, A. Virga, P. Rivolo, F. Geobaldo. F. Giorgis. Surface-enhanced Raman spectroscopy on porous silicon membranes decorated with Ag nanoparticles integrated in elastomeric microfluidic chips. RSC Advances 6 (2016), 21865-21870.

[106] A. Lamberti, A. Virga, A. Chiadò, A. Chiodoni, K. Bejtka, P. Rivolo, F. Giorgis. Ultrasensitive Ag-coated TiO_2 nanotube arrays for flexible SERS-based optofluidic devices. Journal of Materials Chemistry C 3 (2015), 6868-6875.

[107] M. H. Shin, W. Hong, Y. Sa, L. Chen, Y. J. Jung, X. Wang, B. Zhao, Y. M. Jung. Multiple detection of proteins by SERS-based immunoassay with core shell magnetic gold nanoparticles. Vibrational Spectroscopy 72 (2014), 44–49.

[108] K. W. Kho, U. S. Dinish, M. Olivo. Biomedicine with surface enhanced Raman scattering (SERS). Biophotonics for Medical Applications (2015), 101-134.

[109] G. Binnig, C. F. Quate, Ch. Gerber. Atomic Force Microscope. Phys. Rev. Lett. 56 (1986).

[110] T. Thundat, R. J. Warmack, G. Y. Chen, D. P. Allison: Thermal, ambient-induced deflections of scanning force microscope cantilevers, Appl. Phys. Lett. 64 (1994), 2894–2896.

[111] H. J. Butt. A Sensitive Method to Measure Changes in the Surface Stress of Solids. Journal of Colloid and Interface Science 180 (1996), 251–260.

[112] R. Berger, E. Delamarche, H. P. Lang, Ch. Gerber, J. K. Gimzewski, E. Meyer, H.-J. Güntherodt: Surface stress in the self-assembly of alkanethiols on gold, Science 276 (1997), 2021–2024.

[113] H. P. Lang, R. Berger, C. Andreoli, J. Brugger, M. Despont, P. Vettiger, Ch. Gerber, J. K. Gimzewski, J.-P. Ramseyer, E. Meyer, H.-J. Güntherodt: Sequential position readout from arrays of micromechanical cantilever sensors, Appl. Phys. Lett. 72 (1998), 383–385.

[114] J. Fritz, M. K. Baller, H. P. Lang, H. Rothuizen, P. Vettiger, E. Meyer, H.-J. Güntherodt, Ch. Gerber, J. K. Gimzewski: Translating biomolecular recognition into nanomechanics, Science 288 (2000), 316–318.

[115] G. Stoney. The tension of metallic films deposited by electrolysis. Proc. Royal Soc. London, A82 (1909) 172.

[116] R. J. Jaccodine, W. A. Schlegel. Measurement of strains at Si–SiO_2 interface. J. Appl. Phys. 37 (1966), 2429.

[117] K. L. Ekinci, Y. T. Yang, M. L. Roukes. Ultimate limits to inertial mass sensing based upon nanoelectromechanical system. J Appl Phys 95 (2004), 2682–2689.

[118] Y. T. Yang, C. Callegari, X. L. Feng, K. L. Ekinci, M. L. Roukes . Zeptogram-scale nanomechanical mass sensing. Nano Lett. 6 (2006), 583.

[119] M. Rodahl, F. Höök, A. Krozer, P. Brzezinski, B. Kasemo. Quartz-crystal microbalance setup for frequency and *q*-factor measurements in gaseous and liquid environments. Rev. Sci. Instrum. 66 (1995), 3924–3930.

[120] D. A. Davis. Classical Mechanics (1986).

[121] W. C. Young, R. G. Budynas, R. J. Roark. Roark's Formulas for Stress and Strain. Boston, MA: McGraw-Hill (2002).

[122] G. T. A. Kovacs, N. I. Maluf, K. E. Petersen. Bulk micromachining of silicon. Proc. IEEE 86 (1998), 1536.

[123] G. S. May, S. M. Sze. Photolithography, Fundamentals of Semiconductor Fabrication. New York: Wiley (2004).

[124] M. A. McCord, M. J. Rooks. Electron beam lithography Handbook of Microlithography. Micromachining, and Microfabrication vol 1 (1997).

[125] G. Genolet, J. Brugger, M. Despont, U. Drechsler, P. Vettiger, N. F. de Rooij, D. Anselmetti. Soft, entirely photoplastic probes for scanning force microscopy. Rev. Sci. Instrum. 70 (1999), 2398.

[126] M. Hopcroft, T. Kramer, G. Kim, K. Takashima, Y. Higo, D. Moore, J. Brugger. Micromechanical testing of SU-8 cantilevers. Fatigue Fract. Eng. Mater. Struct. 28 (2005), 735.

[127] A. Gaitas, Y. B. Gianchandani. An experimental study of the contact mode AFM scanning capability of polyimide cantilever probes. Ultramicroscopy 106 (2006), 874.

[128] A. W. McFarland, M. A. Poggi, L. A. Bottomley, J. S. Colton. Production and characterization of polymer microcantilevers. Rev. Sci. Instrum. 75 (2004), 2756.

[129] A. W. McFarland, J. S. Colton. Chemical sensing with micromolded plastic microcantilevers. J. Microelectromech. Syst. 14 (2005), 1375.

[130] X. R. Zhang, X. Xu. Development of a biosensor based on laser-fabricated polymer microcantilevers. Appl. Phys. Lett. 85 (2004), 2423.

[131] J. Zou, X. Wang, D. Bullen, K. Ryu, C. Liu, C. A. Mirkin. A mould-and-transfer technology for fabricating scanning probe microscopy probes. J. Micromech. Microeng. 14 (2004), 204.

[132] M. Calleja, J. Tamayo, A. Johansson, P. Rasmussen, L. M. Lechuga, A. Boisen. Polymeric cantilever arrays for biosensing applications. Sensor Lett. 1 (2003), 20.

[133] J. H. T. Ransley, M. Watari, D. Sukumaran, R. A. McKendry, A. A. Seshia. SU8 bio-chemical sensor microarrays. Microelectron. Eng. 83 (2006), 1621.

[134] R. Katragadda, Z. Wang, W. Khalid, Y. Li, Y. Xu. Parylene cantilevers integrated with polycrystalline silicon piezoresistors for surface stress sensing. Appl. Phys. Lett. 91 (2007), 083505.

[135] R. H. Ibbotson, R. J. Dunn, V. Djakov, P. K. Ferrigno, S. E. Huq. Polyimide microcantilever surface stress sensor using low-cost, rapidly-interchangeable, spring-loaded microprobe connections. Microelectron. Eng. 85 (2008), 1314.

[136] A. Greve, S. Keller, A. L. Vig, A. Kristensen, D. Larsson, K. Yvind, J. M. Hvam, M. Cerruti, A. Majumdar, A. Boisen. Thermoplastic microcantilevers fabricated by nanoimprint lithography. J. Micromech. Microeng. 20 (2010), 015009.

[137] C. Martin, A. Llobera, G. Villanueva, A. Voigt, G. Gruetzner, J. Brugger, F. Perez-Murano. Stress and aging minimization in photoplastic AFM probes. Microelectron. Eng. 86 (2009), 1226.

[138] S. Mouaziz, G. Boero, R. S. Popovic, J. A. B. J. Brugger. Polymer-based cantilevers with integrated electrodes. J. microelectromech. Syst. 15 (2006), 890.

[139] R. Legtenberg, H. A. C. Tilmans, J. Elders, M. Elwenspoek. Stiction of surface micromachined structures after rinsing and drying: model and investigation of adhesion mechanisms. Sensors and Actuators A 43 (1994), 230.

[140] A. W. McFarland, M. A. Poggi, L. A. Bottomley, J. S. Colton. Injection moulding of high aspect ratio micron-scale thickness polymeric microcantilevers. Nanotechnology 15 (2004), 1628.

[141] E. Manias, J. Chen, N. Fang, X. Zhang. Polymeric micromechanical components with tunable stiffness. Appl. Phys. Lett. 79 (2001), 1700.

[142] Z. Bayindir, Y. Sun, M. J. Naughton, C. N. LaFratta, T. Baldacchini, J. T. Fourkas, J. Stewart, B. E. A. Saleh, M. C. Teich. Polymer microcantilevers fabricated via multiphoton absorption polymerization Appl. Phys. Lett. 86 (2005), 064105.

[143] E. Forsen, G. Abadal, S. Ghatnekar-Nilsson, J. Teva, J. Verd, R. Sandberg, W. Svendsen, F. Perez-Murano, J. Esteve, E. Figueras, F. Campabadal, L. Montelius, N. Barniol, A. Boisen. Ultrasensitive mass sensor fully integrated with complementarymetal-oxide-semiconductor circuitry. Applied Physics Letters 87 (2005), 043507.

[144] B. Ilic, S. Krylov, H. G. Craighead. Theoretical andexperimental investigation of optically driven nanoelectromechanical oscillators. J. Appl. Phys. 107 (2010), 13.

[145] B. Ilic, D. Czaplewski, M. Zalalutdinov, H. G. Craighead, P. Neuzil, C. Campagnolo, C. Batt. Single cell detection with micromechanical oscillators. J. Vac. Sci. Technol. B 19 (2001), 2825.

[146] K. L. Ekinci. Electromechanical Transducers at the Nanoscale: Actuation and Sensing of Motion in Nanoelectromechanical Systems (NEMS). Nanoelectromechanical systems (2005) 1, No. 8-9, 786 –797.

[147] H. P. Lang, M. K. Baller, R. Berger, C. Gerber, J. K. Gimzewski, F. M. Battiston, P. Fornaro, J. P. Ramseyer, E. Meyer, H. J. Guntherodt. An artificial nose based on a micromechanical cantilever array. Anal. Chim. Acta 393 (1999), 59.

[148] M. Yue, J. C. Stachowiak, H. Lin, R. Datar, R. Cote, A. Majumdar. Label-free protein recognition two-dimensional array using nanomechanical sensors. Nano Lett. 8 (2008), 520.

[149] F. Amiot, F. Hild, F. Kanoufi, J. P. Roger. Identification of the electroelastic coupling from full multi-physical fields measured at the micrometre scale. J. Phys. D: Appl. Phys. 40 (2007), 3314.

[150] D. Larsson, A. Greve, J. M. Hvam, A. Boisen, K. Yvind. Self-mixing interferometry in vertical-cavity surface-emitting lasers for nanomechanical cantilever sensing. Appl. Phys. Lett. 94 (2009), 091103.

[151] N. Blanc, J. Brugger, N. F. de Rooij, U. Durig. Scanning force microscopy in the dynamic mode using microfabricated capacitive sensors. J. Vac. Sci. Technol. B 14 (1996), 901.

[152] S. J. Kim, T. Ono, M. Esashi. Capacitive resonant mass sensor with frequency demodulation detection based on resonant circuit. Appl. Phys. Lett. 88 (2006), 053116.

[153] T. Itoh, T. Suga. Development of a force sensor for atomic force microscopy using piezoelectric thin films. Nanotechnology 4 (1993), 218.

[154] S. Watanabe, T. Fujii. Micro-fabricated piezoelectric cantilever for atomic force microscopy. Rev. Sci. Instrum. 67 (1996), 3898.

[155] J. H. Lee, K. S. Hwang, J. Park, K. H. Yoon, D. S. Yoon, T. S. Kim. Immunoassay of prostate-specific antigen (PSA) using resonant frequency shift of piezoelectric nanomechanical microcantilever. Biosensors Bioelectron. 20 (2005), 2157.

[156] B. H. Cha, S. M. Lee, J. C. Park, K. S. Hwang, S. K. Kim, Y. S. Lee, B. K. Ju, T. S. Kim. Detection of Hepatitis B Virus (HBV) DNA at femtomolar concentrations using a silica nanoparticle-enhanced microcantilever sensor. Biosensors Bioelectron. 25 (2009), 130.

[157] M. Tortonese, R. C. Barrett, C. F. Quate. Atomic resolution with an atomic force microscope using piezoresistive detection. Appl. Phys. Lett. 62 (1993), 834.

[158] R. Linnemann, T. Gotszalk, L. Hadjiski, I. W. Rangelow. Characterization of a cantilever with an integrated deflection sensor. Thin Solid Films 264 (1995), 159.

[159] S. Kim, T. Rahman, L. R. Senesac, B. H. Davison, T. Thundat. Piezoresistive cantilever array sensor for consolidated bioprocess monitoring. Scanning 31 (2009), 204.

[160] G. A. Baker, R. Desikan, T. Thundat. Label-free sugar detection using phenylboronic acid-functionalized piezoresistive microcantilevers. Anal. Chem. 80 (2008), 4860.

[161] J. Thaysen, A. Boisen, O. Hansen, S. Bouwstra. Atomic force microscopy probe with piezoresistive read-out and a highly symmetrical Wheatstone bridge arrangement. Sensors Actuators A 83 (2000), 47.

[162] I. Voiculescu, M. E. Zaghloul, R. A. McGill, E. J. Houser, G. K. Fedder. Electrostatically actuated resonant microcantilever beam in CMOS technology for the detection of chemical weapons. IEEE Sensors J. 5 (2005), 641.

[163] N. V. Lavrik, M. J. Sepaniak, P. G. Datskos. Cantilever transducers as a platform for chemical and biological sensors. Rev. Sci. Instrum. 75 (2004), 2229.

[164] N. L. Rosi, C. A. Mirkin. Nanostructures in biodiagnostics. Chem Rev 105 (2005), 1547–1562.

[165] C. Ziegler. Cantilever-based biosensor. Anal. Bioanal. Chem. 379 (2004), 946–959.

[166] Y. Arntz, J. D. Seelig, H. P. Lang, J. Zhang, P. Hunziker, J. P. Ramseyer, E. Meyer, M. Hegner, Ch. Gerber. Label-free protein assay based on a nanomechanical cantilever array. Nanotechnology 14 (2003).

[167] K. W. Wee, G. Y. Kang, J. Park, J. Y. Kang, D. S. Yoon, J. H. Park, T. S. Kim. Novel electrical detection of label-free disease marker proteins using piezoresistive self-sensing micro-cantilevers. Biosensors and Bioelectronics 20 (2005), 1932–1938.

[168] P. S. Waggoner, M. Varshney, H. G. Craighead. Detection of prostate specific antigen with nanomechanical resonators. Lab on a Chip 9 (2009), 3095–3099.

[169] B. Ilic, Y. Yang, H. G. Craighead. Virus detection using nanoelectromechanical devices. Appl. Phys. Lett. 85 (2004), 2604–2606.

[170] D. Maraldo, K. Rijal, G. A. Campbell, R. Mutharasan. Method for label-free detection of femtogram quantities of biologics in flowing liquid samples. Analytical Chemistry 79 (2007), 2762-2770.

[171] Q. Zhu, W. Y. Shih, W. H. Shih. In situ, in-liquid, all-electrical detection of *Salmonella typhimurium* using lead titanate zirconate/gold-coated glass cantilevers at any dipping depth. Biosens Bioelectron. 22 (2007), 3132-8.

[172] M. Su, S. Li, V. P. Dravid. Microcantilever resonance-based DNA detection with nanoparticle probes. Applied Physics Letters 82 (2003),3562–3564.

[173] A. Ymeti, J. S. Kanger, J. Greve, G. A. J. Besselink, P. V. Lambeck, R. Wijn, R. G. Heideman. Integration of microfluidics with a four-channel integrated optical Young interferometer immunosensor. Biosensors and Bioelectronics 20 (2005), 1417–1421.

[174] F. Prieto, L. M. Lechuga, A. Calle, A. Llobera, C. Domìnguez. Optimised silicon antiresonant reflecting optical waveguides for sensing applications. J. Lightwave Technol. 19 (2001), 75–83.

[175] H. Zhu, J. D. Suter, X. Fan. Optical guided-wave chemical and biosensors II, Springer Series on Chemical Sensors and Biosensors 8 (2010), Springer-Verlag, 259–279.

[176] J. A. Howarter, J. P. Youngblood. Optimization of Silica Silanization by 3-Aminopropyltriethoxysilane. Langmuir 22 (2006), 11142-11147.

[177] A. Ulman. Formation and structure of self-assembled monolayers. Chem. Rev. 96 (1996), 1533–1554.

[178] D. K. Aswal, S. Lenfant, D. Guerin, J. V. Yakhmi, D. Vuillaume. Self assembled monolayers on silicon for molecular electronics. Anal Chim Acta 24 (2006), 84-108.

[179] C. Shi, S. Mehrabani, A. M. Armani. Leveraging bimodal kinetics to improve detection specificity. Opt. Lett. 37 (2012), 1643–1645.

[180] B. W. Biggs, H. K. Hunt, and A. M. Armani. Selective patterning of Si-based biosensor surfaces using isotropic silicon etchants. J. Colloid Interface Sci. 369 (2012), 477–481.

[181] S. Pal, E. Guillermain, R. Sriram, B. L. Miller, P. M. Fauchet. Silicon photonic crystal nanocavity-coupled waveguides for error-corrected optical biosensing. Biosens. Bioelectron 26 (2011), 4024–4031.

[182] J.-Y. Byeon, F. T. Limpoco, and R. C. Bailey. Efficient Bioconjugation of Protein Capture Agents to Biosensor Surfaces Using Aniline-Catalyzed Hydrazone Ligation. Langmuir 26 (2010), 15430-15435.

[183] H. K. Hunt, C. Soteropulos, A. M. Armani. Bioconjugation Strategies for Microtoroidal Optical Resonators. Sensors 10 (2010), 9317-9336.

[184] A. L. Washburn, L. C. Gunn, R. C. Bailey. Label-Free Quantitation of a Cancer Biomarker in Complex Media Using Silicon Photonic Microring Resonators, Anal. Chem. 81 (2009), 9499-9506.

[185] C. E. Soteropoulos, H. K. Hunt, A. M. Armani. Determination of binding kinetics using whispering gallery mode microcavities. Appl. Phys. Lett. 99 (2011), 103703.

[186] J. García-Rupérez, V. Toccafondo, M.J. Banuls, J. García Castelló, A. Griol, S. Peransí-Llopis, A. Maquieira. Label-free antibody detection using band edge fringes in SOI planar photonic crystal waveguides in the slow-light regime. Opt. Express 18 (2010), 24276–24286.

[187] N. Massad-Ivanir, G. Shtenberg, A. Tzur, M. A. Krepker, E. Segal. Engineering nanostructured porous SiO(2) surfaces for bacteria detection via “Direct Cell Capture”. Anal Chem 83 (2011), 3282–3289.

[188] S. Grego, J. R. McDaniel, and B. R. Stoner. Wavelength interrogation of grating-based optical biosensors in the input coupler configuration. Sens. Actuators B 131 (2008), 347–355.

[189] K. De Vos, I. Bartolozzi, E. Schacht, P. Bienstman, R. Baets. Silicon-on-insulator microring resonator for sensitive and label-free biosensing. Opt. Express 15 (2007), 7610–7615.

[190] H. W. Choi, H. Takahashi, T. Ooya and T. Takeuchi. Label-free detection of glycoproteins using reflectometric interference spectroscopy-based sensing system with upright episcopic illumination. Anal. Methods 3 (2011), 1366.

[191] A. Ksendzov, Y. Lin. Integrated optics ring-resonator sensors for protein detection. Opt. Lett. 30 (2005), 3344–3346.

[192] H.K. Hunt, A.M. Armani. Recycling microcavity optical biosensors. Opt. Lett. 36 (2011), 1092–1094.

[193] L. M. Bonanno, L. A. DeLouise. Steric crowding effects on target detection in an affinity biosensor. Langmuir 23 (2007), 5817–5823.

[194] E. T. Vanderberg, L. Bertilsson, B. Liedberg, K. Uvdal, R. Erlandsson, H. Elwing, I. Lundstrom. Structure of 3-aminopropyltriethoxisylane on silicon oxides. J Colloid Interface Sci 147 (1991), 103–118.

[195] A. Densmore, M. Vachon, D.-X. Xu, S. Janz, R. Ma, Y.-H. Li, G. Lopinski, A. Delage, J. Lapointe, C. C. Luebert, Q. Y. Liu, P. Cheben, J. H. Schmid. Silicon photonic wire biosensor array for multiplexed real-time and label-free molecular detection. Opt. Lett. 34 (2009), 3598–3600.

[196] D. Maraldo, R. Mutharasan. Optimization of antibody immobilization for sensing using piezoelectrically excited-millimeter-sized cantilever (PEMC) sensors. Sensors and Actuators B 123 (2007), 474-479.

[197] S. Wong, D. Putnam. Overcoming limiting side reactions associated with an NHS-activated precursor of polymethacrylamide-based polymers. Bioconjug Chem 18 (2007), 970–982.

[198] Z. B. Bahşi, A. Büyükaksoy, S. M. Ölmezcan, F. Şimşek, M. H. Aslan, A. Y. Oral. A Novel Label-Free Optical Biosensor Using Synthetic Oligonucleotides from E. coli O157:H7: Elementary Sensitivity Tests. Sensors 9 (2009), 4890-4900.

[199] E. De Tommasi, L. De Stefano, I. Rea, V. Di Sarno, L. Rotiroti, P. Arcari, A. Lamberti, C. Sanges, I. Rendina. Porous Silicon Based Resonant Mirrors for Biochemical Sensing. Sensors 8 (2008), 6549-6556.

[200] S. Lee, S. C. Eom, J. S. Chang, C. Huh, G. Y. Sung, J. H. Shin. A silicon nitride microdisk resonator with a40-nm-thin horizontal air slot. Opt. Express 18 (2010), 11209–11215.

[201] G. Rong, A. Najmaie, J. E. Sipe, S. M. Weiss. Nanoscale porous silicon waveguides for label-free DNA sensing. Biosens. Bioelectron. 23 (2008), 1572-1576.

[202] S. Mandal, J. M. Goddard, D. Erickson. A multiplexed optofluidic biomolecular sensor for low mass detection. Lab on a Chip 9 (2009), 2924-2932.

[203] B. Sepúlveda, J. Sánchez del Río, M. Moreno, F. J. Blanco, K. Mayora, C. Domínguez, L. M. Lechuga. Optical biosensor micro-systems based on the integration of highly sensitive Mach-Zehnder interferometer devices. J. Opt. A, Pure Appl. Opt. 8 (2006), S561–S566.

[204] J. Xu, D. Suarez, and D. S. Gottfried. Detection of avian influenza virus using an interferometric biosensor. Anal. Bioanal. Chem. 389 (2007), 1193-1199.

[205] A. Wang, H. Tang, T. Cao, S. O. Salley, K. Y. Simon Ng. In vitro stability study of organosilane self-assemble monolayers and multilayers. Journal of Colloid and Interface Science 291 (2005), 438–447.

[206] A. Ramachandran, S. Wang, J. Clarke, S. J. Ja, D. Goad, L. Wald, E. M. Flood, E. Knobbe, J. V. Hryniewicz, S. T. Chu, D. Gill, W. Chen, O. King, B. E. Little. A universal biosensing platform based on optical micro-ring resonators. Biosensors and Bioelectronics 23 (2008), 939–944.

[207] K. De Vos, J. Girones, T. Claes, Y. De Koninck, S. Popelka, E. Schacht, R. Baets, P. Bienstman. Multiplexed Antibody Detection With an Array of Silicon-on-Insulator Microring Resonators. IEEE Photonics Journal 4 (2009), 225-235.

[208] K. De Vos, J. Gironès, S. Popelka, E. Schacht, R. Baets, P. Bienstman. SOI optical microring resonator with poly(ethylene glycol) polymer brush for label-free biosensor applications. Biosens. Bioelectron. 24 (2009), 2528-2533.

[209] D. Duval, A. B. González-Guerrero, S. Dante, J. Osmond, R. Monge, L. J. Fernández, K. E. Zinoviev, C. Domínguez, L. M. Lechuga. Nanophotonic lab-on-a-chip platforms including novel bimodal interferometers, microfluidics and grating couplers. Lab Chip 12 (2012), 1987–1994.

[210] S. Zlatanovic, L. W. Mirkarimi, M. M. Sigalas, M. A. Bynum, E. Chow, K. M. Robotti, G. W. Burr, S. Esener, A. Grot. Photonic crystal microcavity sensor for ultracompact monitoring of reaction kinetics and protein concentration. Sens. Actuators B 141 (2009), 13–19.

[211] G.T. Hermanson. Bioconjugate Techniques, 2nd Edition (2008), Academic Press, London, UK.

[212] Y. Xu, X. Wu, X. Xie, Y. Zhong, R. Guidoin, Z. Zhang, Q. Fu. Synthesis of polycarbonate urethanes with functional poly(ethylene glycol) side chains intended for bioconjugates. Polymer 54 (2013), 5363–5373.

[213] J. Escorihuela, M. J. Banuls, R. Puchades, A. Maquieira. DNA microarrays on silicon surfaces through thiol-ene chemistry. Chem Commun 48 (2012), 2116-2118.

[214] E. Hanson, J. Schwartz, B.Nickel, N. Koch, M. Danisman. Bonding Self-Assembled, Compact organo-phosphonate Monolayers to the Native Oxide Surface of Silicon. J. Am. Chem. Soc., 125 (2003), 16074-16080.

[215] A. Cattani-Scholz, D. Pedone, F. Blobner, G. Abstreiter, J. Schwartz, M. Tornow, L. Andruzzi. PNA-PEG Modified Silicon Platforms as Functional Bio-Interfaces for Applications in DNA Microarrays and Biosensors. Biomacromolecules 10 (2009), 489-496.

[216] F. Cheng, J. Shang, D. M. Ratner. A Versatile Method for Functionalizing Surfaces with Bioactive Glycans. Bioconjug Chem. 22 (2011), 50–57.

[217] T. Bocking, K. A. Kilian, K. Gaus, J. J. Gooding. Modifying Porous Silicon with Self-Assembled Monolayers for Biomedical Applications: The Influence of Surface Coverage on Stability and Biomolecule Coupling. Adv. Funct. Mater. 18 (2008), 3827–3833.

[218] H. Qiao, B. Guan J.J. Gooding, P.J Reece. Protease detection using a porous silicon based Bloch surface wave optical biosensor. Optics Express 18 (2010), 15174-15182.

[219] L. De Stefano, L. Rotiroti, I. Rea, I. Rendina, P. Arcari, A. Lamberti, C. Sanges. DNA optical detection based on porous silicon technology: from biosensors to biochips. Sensors 7 (2007), 214-221.

[220] E. Harlow, D. Lane. Antibodies: A Laboratory Manual, First Edition (1988).

[221] P. S. Waggoner, H. G. Craighead. Micro- and nanomechanical sensors for environmental, chemical, and biological detection. Lab Chip 7 (2007), 1238–1255.

[222] C. Ricciardi, S. Fiorilli, S. Bianco, G. Canavese, R. Castagna, I. Ferrante, G. Digregorio, S. L. Marasso, L. Napione, F. Bussolino. Development of microcantilever-based biosensor array to detect Angiopoietin-1, a marker of tumor angiogenesis. Biosensors and Bioelectronics 25 (2010), 1193–1198.

[223] M. Bonanno, L.A. DeLouise. Whole blood optical biosensor. Biosens. Bioelectron. 23 (2007), 444–448.

[224] Y. Guo, J. Y. Ye, C. Divin, B. Huang, T. P. Thomas, J. R. Baker, T. B. Norris. Real-time biomolecular binding detection using a sensitive photonic crystal biosensor. Anal. Chem. 82 (2010), 5211-5218.

[225] S. Sharma, R.W. Johnson, T.A. Desai. XPS and AFM analysis of antifouling PEG interfaces for microfabricated silicon biosensors. Biosens. Bioelectron. 20 (2004), 227-239.

[226] B. H. Schneider, E. L. Dickinson, M. D. Vach, J. V. Hoijer, L. V. Howard. Highly sensitive optical chip immunoassays in human serum. Biosen. and Bioelec. 15 (2000), 13–22.

[227] M. G. Guzman, S. B. Halstead, H. Artsob, P. Buchy, J. Farrar, D. J. Gubler, E. Hunsperger, A. Kroeger, H. S. Margolis, E. Martínez, M. B. Nathan, J. L. Pelegrino, C. Simmons, S. Yoksan, R. W. Peeling. Dengue: a continuing global threat. Nat Rev Microbiol 8 (2010),S7-S16.

[228] B. Zhang, G. B. Salieb-Beugelaar, M. M. Nigo, M. Weidmann, P. Hunziker. Diagnosing dengue virus infection: rapid tests and the role of micro/nanotechnologies. Nanomedicine: Nanotechnology, Biology, and Medicine 11 (2015), 1745–1761.

[229] WHO. Global strategy for dengue prevention and control, 2012-2020. [online] http://www.who.int/denguecontrol/9789241504034/en/Geneva, Switzerland: WHO; 2012.

[230] D. J. Gubler. Dengue and dengue hemorrhagic fever. Clin Microbiol Rev 11 (1998), 480-96.

[231] M. G. Guzman, G. Kouri. Dengue: an update. Lancet Infect Dis 2(2002), 33-42.

[232] S. B. Halstead. Dengue. Lancet 370 (2007), 1644-52.

[233] TDR/WHO. Dengue: guidelines for diagnosis, treatment, prevention and control. [online] http://www.who.int/denguecontrol/en/ Geneva, Switzerland: TDR/WHO; 2009.

[234] J. L. Kyle, E. Harris. Global spread and persistence of dengue. Annu Rev Microbiol 62 (2008), 71-92.

[235] P. Y. Shu, J. H. Huang. Current advances in dengue diagnosis. Clin Diagn Lab Immunol 11 (2004), 642-50.

[236] M. Bessaud, B. A. M. Pastorino, C. N. Peyrefitte, D. Rolland, M. Grandadam, H. J. Tolou. Functional characterization of the NS2B/NS3 protease complex from seven viruses belonging to different groups inside the genus Flavivirus. Virus Res. 120 (2006) 79–90.

[237] S. P. Lim, Q.-Y. Wang, C. G. Noble, Y.-L. Chen, H. Dong, B. Zou, et al. Ten years of dengue drug discovery: progress and prospects. Antiviral Res. 100 (2013) 500–519.

[238] S. Bhakat, W. Karubiu, V. Jayaprakash, M. E. S. Soliman. A perspective on targeting non-structural proteins to combat neglected tropical diseases: dengue, west nile and chikungunya viruses. Eur. J. Med. Chem. 87 (2014), 677–702.

[239] R. W. Peeling, H. Artsob, J. L. Pelegrino, P. Buchy, M. J. Cardosa, S. Devi, et al. Evaluation of diagnostic tests: dengue. Nat Rev Microbiol 8 (2010), S30-8.

[240] E. C. Holmes. The evolutionary biology of dengue virus. Novartis Found Symp 277 (2006), 177-87.

[241] A. T. Mairuhu, J. Wagenaar, D. P. Brandjes, E. C. van Gorp. Dengue: an arthropod-borne disease of global importance. Eur J Clin Microbiol Infect Dis 23 (2004), 425-33.

[242] M. Montoya, L. Gresh, J. C. Mercado, K. L. Williams, M. J. Vargas, G. Gutierrez, et al. Symptomatic versus inapparent outcome in repeat dengue virus infections is influenced by the time interval between infections and study year. PLoS Negl Trop Dis 7 (2013), e2357.

[243] S. S. Sam, S. F. Omar, B. T. Teoh, J. Abd-Jamil, S. AbuBakar. Review of dengue hemorrhagic fever fatal cases seen among adults: a retrospective study. PLoS Negl Trop Dis, 7 (2013), e2194.

[244] M. G. Guzman, M. Alvarez, S. B. Halstead. Secondary infection as a risk factor for dengue hemorrhagic fever/dengue shock syndrome: an historical perspective and role of antibody-dependent enhancement of infection. Arch Virol 158 (2013), 1445-59.

[245] S. Zompi, E. Harris. Original antigenic sin in dengue revisited. Proc Natl Acad Sci U S A 110 (2013), 8761-2.

[246] A. L. Rothman. Immunity to dengue virus: a tale of original antigenic sin and tropical cytokine storms. Nat Rev Immunol 11 (2011), 532-43.

[247] T. Pang, M. J. Cardosa, M. G. Guzman. Of cascades and perfect storms: the immunopathogenesis of dengue haemorrhagic fever-dengue shock syndrome (DHF/DSS). Immunol Cell Biol 85 (2007), 43-5.

[248] C. F. Lin, S. W. Wan, H. J. Cheng, H. Y. Lei, Y. S. Lin. Autoimmune pathogenesis in dengue virus infection. Viral Immunol 19 (2006), 127-32.

[249] S. W. Wan, C. F. Lin, T. M. Yeh, C. C. Liu, H. S. Liu, S. Wang, et al. Autoimmunity in dengue pathogenesis. J FormosMed Assoc 112 (2013), 3-11.

[250] N. T. Darwish, Y. B. Alias, S. M. Khor. An introduction to dengue-disease diagnostics. Trends in Analytical Chemistry 67 (2015), 45–55.

[251] F. S. Teles. Biosensors and rapid diagnostic tests on the frontier between analytical and clinical chemistry for biomolecular diagnosis of dengue disease: a review. Anal Chim Acta 687 (2011), 28-42.

[252] P. Patel, O. Landt, M. Kaiser, O. Faye, T. Koppe, U. Lass, et al. Development of one-step quantitative reverse transcription PCR for the rapid detection of flaviviruses. Virol J 10 (2013), 1-11.

[253] P. Y. Shu, S. F. Chang, Y. C. Kuo, Y. Y. Yueh, L. J. Chien, C. L. Sue, et al. Development of group- and serotype-specific one-step SYBR green I-based real-time reverse transcription-PCR assay for dengue virus. J Clin Microbiol 41 (2003), 2408-16.

[254] S. J. Wu, E. M. Lee, R. Putvatana, R. N. Shurtliff, K. R. Porter, W. Suharyono, et al. Detection of dengue viral RNA using a nucleic acid sequencebased amplification assay. J Clin Microbiol 39 (2001), 2794-8.

[255] E. A. Hunsperger, S. Yoksan, P. Buchy, V. C. Nguyen, S. D. Sekaran, D. A. Enria, et al. Evaluation of commercially available anti-dengue virus immunoglobulin M tests. Emerg Infect Dis 15 (2009), 436-40.

[256] M. G. Guzman, T. Jaenisch, R. Gaczkowski, V. T. Ty Hang, S. D. Sekaran, A. Kroeger, et al. Multi-country evaluation of the sensitivity and specificity of two commercially-available NS1 ELISA assays for dengue diagnosis. PLoS Negl Trop Dis 4 (2010), e811.

[257] E. M. Linaresa, L. T. Kubotab, J. Michaelisc, S. Thalhammer. Enhancement of the detection limit for lateral flow immunoassays: Evaluation and comparison of bioconjugates. Journal of Immunological Methods 375 (2012), 264–270.

[258] S. D. Blacksell, P. N. Newton, D. Bell, J. Kelley, M. P. Mammen Jr, D. W. Vaughn, et al. The comparative accuracy of 8 commercial rapid immunochromatographic assays for the diagnosis of acute dengue virus infection. Clin Infect Dis 42 (2006), 1127-34.

[259] T. Z. Wu, C. C. Su, L. K. Chen, H. H. Yang, D. F. Tai, K. C. Peng. Piezoelectric immunochip for the detection of dengue fever in viremia phase. Biosens Bioelectron 21 (2005), 689-95.

[260] D. F. Tai, C. Y. Lin, T. Z. Wu, J. H. Huang, P. Y. Shu. Artificial receptors in serologic tests for the early diagnosis of dengue virus infection. Clin Chem 52 (2006), 1486-91.

[261] S. Kumbhat, K. Sharma, R. Gehlot, A. Solanki, V. Joshi. Surface plasmon resonance based immunosensor for serological diagnosis of dengue virus infection. J Pharm Biomed Anal 52 (2010), 255-9.

[262] P. Jahanshahi, E. Zalnezhad, S. D. Sekaran, F. R. M. Adikan. Rapid immunoglobulin M-based dengue diagnostic test using surface plasmon resonance biosensor. Sci Rep 4 (2014), 1-7.

[263] B. T. Nguyen, A. E. Peh, C. Y. Chee, K. Fink, V. T. Chow, M. M. Ng, et al. Electrochemical impedance spectroscopy characterization of nanoporous alumina dengue virus biosensor. Bioelectrochemistry 88 (2012), 15-21.

[264] J. Deng, C. S. Toh. Impedimetric DNA biosensor based on a nanoporous alumina membrane for the detection of the specific oligonucleotide sequence of dengue virus. Sensors 13 (2013), 7774-85.

[264] B. N. Johnson, R. Mutharasan. Biosensing using dynamic-mode cantilever sensors: A review. Biosensors and Bioelectronics 32 (2012), 1–18.

[265] C. Ricciardi, R. Castagna, I. Ferrante, F. Frascella, S. L. Marasso, A. Ricci, G. Canavese, A. Loré, A. Prelle, M. L. Gullino, D. Spadaro. Development of a microcantilever-based immunosensing method for mycotoxin detection. Biosensors and Bioelectronics 40 (2013), 233–239.

[266] C. Ricciardi, I. Ferrante, R. Castagna, F. Frascella, S. L. Marasso, K. Santoro, M. Gili, D. Pitardi, M. Pezzolato, E. Bozzetta. Immunodetection of 17β-estradiolin serum at ppt level by microcantilever resonators. Biosensors and Bioelectronics 40 (2013), 407–411.

[267] A. Chiadò, G. Palmara, S. Ricciardi, F. Frascella, M. Castellino, M. Tortello, C. Ricciardi, P Rivolo. Optimization and characterization of a homogeneous carboxylic surface functionalization for silicon-based biosensing. Colloids and Surfaces B: Biointerfaces (2016).

[268] Y.-P. R. Lue, S.-Y. D. Yeo, L.-P. Tan, M. Uttamchandani, G. Y.-J. Chen, S. Q. Yao. Novel strategies in protein microarray generation and detection. Protein Microarrays, Jones & Bartlett Learning, (2005), 13–42.

[269] J. Kim, J. Cho, P. M. Seidler, N. E. Kurland, V. K. Yadavalli. Investigations of Chemical Modifications of Amino-Terminated Organic Films on Silicon Substrates and Controlled Protein Immobilization. Langmuir 26 (2010), 2599–2608.

[270] D. K. Owens, R. C. Wendt. Estimation of the surface free energy of polymers. J. Appl. Polym. Sci. 13 (1969), 1741–1747.

[271] D. A. Shirley. High-resolution x-ray photoemission spectrum of the valence bands of gold. Phys. Rev. B. 5 (1972) 4709–4714.

[272] V. L. Mirinov. Fundamentals of scanning probe microscopy. (2004).

[273] A. Ricci, C. Ricciardi. A new Finite Element approach for studying the effect of surface stress on microstructures. Sensors and Actuators A 159 (2010), 141–148.

[274] L. C. Martineau. Simple thermodynamic model of unassisted proton shuttle uncoupling and prediction of activity from calculated speciation, lipophilicity, and molecular geometry. J. Theor. Biol. 303 (2012), 33–61.

[275] A. Roy, A. Kucukural, Y. Zhang. I-TASSER: a unified platform for automated protein structure and function prediction. Nat. Protoc. 5 (2010) 725–738.

[276] J. Yang, R. Yan, A. Roy, D. Xu, J. Poisson, Y. Zhang. The I-TASSER Suite: protein structure and function prediction. Nat. Methods. 12 (2014), 7–8.

[277] E. F. Pettersen, T. D. Goddard, C. C. Huang, G. S. Couch, D. M. Greenblatt, E. C. Meng, et al. UCSF Chimera - A visualization system for exploratory research and analysis. J. Comput. Chem. 25 (2004), 1605–1612.

[278] C. A. Schneider, W. S. Rasband, K. W. Eliceiri. NIH Image to ImageJ: 25 years of image analysis. Nat. Methods. 9 (2012), 671–675.

[279] F. Frascella, C. Ricciardi. Functionalization Protocols of Silicon Micro/Nano-mechanical Biosensors. Nanomater. Interfaces Biol. Methods Protoc. Methods Mol. Biol. 1025 (2013).

[280] A. Munkholm and S. Brennan. Ordering in Thermally Oxidized Silicon. Phys. Rev. Lett. 93 (2004), 036106.

[281] J.M. Hill, D. G. Royce, C. S. Fadley, L. F. Wagner, F. J. Grunthaner. Properties of oxidized silicon as determined by angular-dependent X-ray photoelectron spectroscopy. Chem. Phys. Lett. Vol. 44, 1976, pp. 225.

[282] M. P. Seah, S. J. Spencer. Ultrathin SiO_2 on Si IV. Intensity measurement in XPS and deduced thickness linearity. Surf. Interface Anal. 35 (2003), 515–524.

[283] C. Cotirlan, A. Galca, C. Ciobanu, C. Logofatu. The study of the silicon oxide thickness on crystalline Si by X-ray photoelectron spectroscopy and spectroscopic ellipsometry. J. Optoelectron. Adv. Mater. 12 (2010) 1092–1097.

[284] D. Bauza, Handbook of Surfaces and Interfaces of Materials, Elsevier (2001).

[285] N. Graf, E. Yegen, T. Gross, A. Lippitz, W. Weigel, S. Krakert, et al. XPS and NEXAFS studies of aliphatic and aromatic amine species on functionalized surfaces. Surf. Sci. 603 (2009), 2849–2860.

[286] F. Truica-Marasescu, M.R. Wertheimer. Nitrogen-Rich Plasma-Polymer Films for Biomedical Applications. Plasma Process. Polym. 5 (2008), 44–57.

[287] I. Migneault, C. Dartiguenave, M. J. Bertrand, K. C. Waldron. Glutaraldehyde: Behavior in aqueous solution, reaction with proteins, and application to enzyme crosslinking. Biotechniques. 37 (2004), 790–802.

[288] M. Rabe, D. Verdes, S. Seeger. Understanding protein adsorption phenomena at solid surfaces. Adv. Colloid Interface Sci. 162 (2011), 87–106.

[289] V. Hlady, J. Buijs. Protein adsorption on solid surfaces. Curr. Opin. Biotechnol. 7 (1996), 72–77.

[290] J. J. Gray. The interaction of proteins with solid surfaces. Curr. Opin. Struct. Biol. 14 (2004), 110–115.

[291] T. J. Su, J. R. Lu, R. K. Thomas, Z. F. Cui. J. Penfold, The Effect of Solution pH on the Structure of Lysozyme Layers Adsorbed at the Silica - Water Interface Studied by Neutron Reflection. 7463 (1998), 438–445.

[292] Y. Xiaoa, S. N. Isaacs. Enzyme-linked immunosorbent assay (ELISA) and blocking with bovine serum albumin (BSA)—not all BSAs are alike. Journal of Immunological Methods 384 (2012), 148–151.

Vorrei ringraziare il Prof. Carlo Ricciardi ed il Prof. Fabrizio Pirri per avermi dato la possibilità di realizzare questo lavoro che fa dell'interdisciplinarietà il suo punto di forza. Inoltre, desidero ringraziare tutte le persone con cui ho lavorato in questi tre anni, con cui ho condiviso e apprezzato quell'alternanza di soddisfazioni e interminabili difficoltà tipica del lavoro di ricerca. In particolare, vorrei ringraziare Alessandro per essere stato una persona disponibile e presente nei momenti di necessità, in grado di spronarti a dare il massimo soprattutto quando gli ostacoli che incontri sembrano non avere mai fine. Infine, desidero ringraziare la mia famiglia per l'incondizionato sostegno e per l'inesauribile pazienza nel sopportare i miei momenti di difficoltà.